The Pennsylvania State University

The Graduate School

Department of Chemical Engineering

SEGMENTAL DYNAMICS IN POLY(ETHYLENE OXIDE)/ POLY(METHYL METHACRYLATE) BLENDS

A Thesis in

Chemical Engineering

by

Chunxia Chen

Submitted in Partial Fulfillment
of the Requirements
for the Degree of

Doctor of Philosophy

December 2006

The thesis of Chunxia Chen was received and approved* by the following:

Janna K. Maranas
Associate Professor of Chemical Engineering and
Material Science and Engineering
Thesis Advisor
Chair of Committee

Kristen Fichthorn
Merrell R. Fenske Chair Professor of Chemical Engineering

Seong H. Kim
Assistant Professor of Chemical Engineering

Patrick Cirino
Assistant Professor of Chemical Engineering

Ralph H. Colby
Professor of Material Science and Engineering
Courtesy Appointment Professor of Chemical Engineering

Andrew L. Zydney
Walter L. Robb Chair and Professor of Chemical Engineering
Head of Department of Chemical Engineering

*Signatures are on file in the Graduate School.

Abstract

Blending has been recognized as a potential tool to tune polymers with designed properties. The present work studies the molecular packing and segmental dynamics in poly(ethylene oxide)/syndiotactic poly(methyl methacrylate) (PEO/PMMA) blends using molecular dynamics simulations with neutron scattering experiments as a test of the accuracy of simulation models.

The static and dynamic properties of poly(ethylene oxide) (PEO) obtained from two levels of modeling, i.e., an explicit atom model and a united atom model, are compared. Both models accurately describe the PEO static structure factor as measured by neutron diffraction. Hydrogen atom motion from the explicit atom model and carbon/oxygen atom motion from the united atom model closely follow the experimental hydrogen motion. Both models also provide a good description of the orientation properties of C-H vectors measured by nuclear magnetic resonance (NMR) experiments.

Local relaxations present in poly(methyl methacrylate) (PMMA) including α-methyl rotation, ester methyl rotation, β-relaxation, and α-relaxation are successfully isolated at temperatures above the glass transition temperature using molecular dynamics simulations. Both activation energies and relaxation times of α-methyl and ester methyl rotations are a continuous extension of those at low temperatures. The β-relaxation is confirmed to originate from the rotation of the entire ester side group, while the α-relaxation is found to be associated with the motion of the main chain.

Distinct dynamics are observed in PEO/PMMA blends with PEO slowed and PMMA speeded, which is consistent with those normally found in polymer blends. The effect of blending on the dynamics of the α-methyl rotation, the ester methyl rotation, and the ester side group rotation in PMMA are also explored. The relaxation times and activation energies of all the three rotations in the blend are smaller than those in pure PMMA, indicating that PEO accelerates these rotations. This phenomenon may be attributed to the faster conformation changes in the blend at high temperatures.

Table of Contents

List of Figures

List of Tables

Acknowledgements

With a deep sense of gratitude, first I wish to express my sincere thanks to my advisor, Dr. Janna K. Maranas, for kindly providing guidance throughout the development of this study. Her support, encouragement, and comments have been of greatest help at all times.

Sincere thanks also go to Dr. Ralph H. Colby, Dr. Kristen Fichthorn, Dr. Seong H. Kim, and Dr. Patrick Cirino for serving as my committee members. Their guidance and critical comments are invaluable to my research. Especial thanks to Dr. Ralph H. Colby for providing the neutron spin echo data.

This work was supported by Polymers Program of the National Science Foundation (DMR-0134910) and Department of Energy Early Career Principal Investigator Program (DE-FG02-02ER25535). This work utilized facilities supported in part by the National Science Foundation (DMR-0454672).

My research group was also a great help to my work, and I am especially grateful to Victoria García Sakai for her help on the experimental part.

I take this opportunity to express my love and sincere thanks to my parents for their endless love and support. My appreciation and love also go to my brother.

I wish to give a very special thank to my husband, Fuhua, who is always there to support me with encouraging words and affection, as well as his experience in programming and numerical simulation. And to my son, Yidong, whose smile has always been an encouragement to me.

Chapter 1
Introduction

1.1 Relaxation processes in glass forming polymers

The relaxation processes of glass forming polymers are characterized by a very broad distribution of temporal and spatial scales. These processes have been widely investigated using a variety of techniques on a number of systems (Kulik et al., 1994; Schmidt-Rohr et al., 1994; Zetsche and Fischer, 1994; Zorn et al., 2002). These processes include the primary (α-) relaxation and secondary processes.

The primary or α-relaxation is believed to be associated with motion of segments of the polymer chain backbones. It is active above the glass transition temperature *Tg*, below which the relaxation times become exceedingly long. Secondary relaxations are related to the local arrangements of the backbone or motions of side groups. These relaxation processes, which include β-relaxation and some fast side group relaxations (for example, methyl group rotations), are active both above and below *Tg*. The relaxation times normally follow an Arrhenius temperature dependence at temperatures below *Tg*. Their high-temperature behaviors are not widely investigated because these processes will group together with α-relaxation to form a single, merged relaxation at high temperatures (Gómez et al., 2001; Arbe et al., 1996). Figure 1.1 gives an example of the typical relaxation processes occurring in glass forming polymers by showing the "relaxation map" of polyisoprene (Arbe et al., 2003).

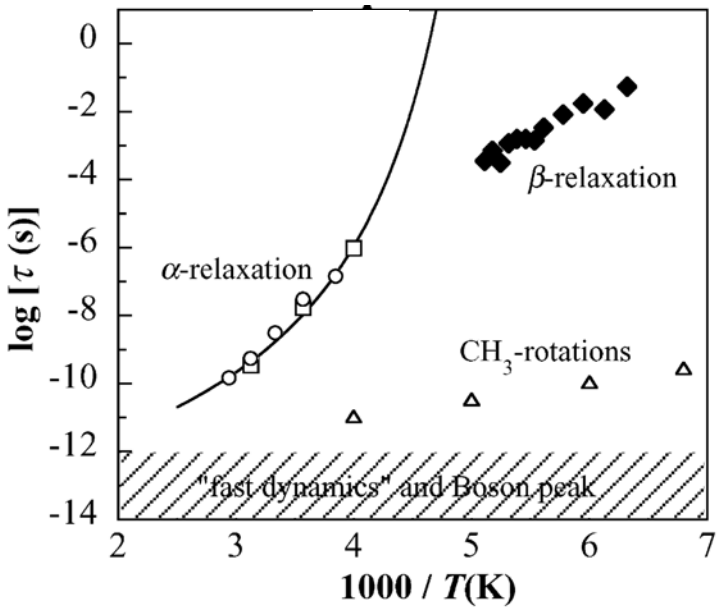

Fig. 1.1 Schematic illustrating the relationship between the relaxation times for primary relaxation (α-relaxation) and the secondary processes.

1.2 Dynamics in miscible polymer blends

The importance of polymer blends has been recognized for a lot of years. Blending two polymers is a cheaper way to achieve new materials with certain physical property requirements than synthesizing new homopolymers. The properties of polymer blends are tunable by appropriate selection of component compositions. An understanding of polymer blend miscibility is crucial to understanding polymer processing and the manipulation of the final product properties.

Polymer miscibility is governed by the Gibbs free energy of mixing (ΔG_m), which is defined as

$$\Delta G_m = \Delta H_m - T\Delta S_m \tag{1.1}$$

where ΔH_m and ΔS_m are the enthalpy and the entropy of mixing, respectively. Two components in the polymer blends (or mixtures) will mix if the Gibbs free energy of mixing is negative,

$$\Delta G_m < 0 \tag{1.2}$$

Furthermore, a single phase binary mixture with component composition ϕ_A and ϕ_B at fixed temperature T and pressure P satisfies the following

$$\left(\frac{\partial^2 \Delta G_m}{\partial \phi_A^2}\right)_{T,P,\phi_B} > 0 \tag{1.3}$$

Flory-Huggins theory, originally derived for small molecular systems, was expanded to model polymer systems by assuming that the polymer consists of a series of connected segments and that each of these segments occupy one lattice site. In this model the expression for the Gibbs free energy of mixing is proposed as (Flory, 1953),

$$\frac{\Delta G_m}{RT} = \frac{\phi_A}{M_A}\ln\phi_A + \frac{\phi_B}{M_B}\ln\phi_B + \chi\phi_A\phi_B \tag{1.4}$$

where M_A and M_B are the molecular weights of component A and B, respectively; ϕ_A and ϕ_B are the volume fractions of component A and B, respectively; χ is the Flory interaction parameter between component A and B. A positive value of this term suggests unfavorable mixing, while a negative one suggests the opposite.

In recent years the dynamics in miscible polymer blends has been the focus of considerable investigations using different techniques. Oscillatory shear (Colby, 1989; Pathak et al., 1999; Roovers and Toporowski, 1992) and dielectric spectroscopy (Roland

and Ngai, 1991; Alegría et al. 1994; Arbe et al., 1999) have been used to investigate dynamics processes on the order of microseconds and longer, while quasielastic neutron scattering (QENS) (Doxastakis et al., 2000; Hoffmann et al., 2000) and nuclear magnetic resonance (NMR) (Chung et al., 1994a; Cendoya et al., 1999) have been applied to probe dynamics on the order of nanosecond to picosecond scale.

It is previously believed that one single glass transition temperature, which is intermediate between the glass transition temperatures of the pure components in miscible polymer blends, is expected. Thus a single α-process should be observed because the α-process is correlated with glass transition as discussed in Section 1.1. However, this is not always the case. Studies show that two distinct α-relaxations can be observed in miscible blends, usually when the *Tg*s of the pure components are well separated (Cendoya et al., 1999; Doxastakis et al., 2000; Hoffmann et al., 2000). At a fixed temperature, the usual observation is that the relaxation times will move closer to each other, i.e. the fast component is slowed and the slow component is accelerated. Polyisoprene/Poly(vinylethylene) (PI/PVE) ($\Delta Tg \cong 60$ K) is a typical polymer blend which has received much attention (Chung et al., 1994a and 1994b; Arbe et al., 1999; Roovers and Toporowski, 1992; Roland and Ngai, 1991; Alegría et al., 1994). The dynamics of the lower *Tg* component, PI, is slowed by adding PVE and the opposite is true for the higher *Tg* component, PVE. Similar observation is observed for poly(ethylene oxide)/poly(methyl methacrylate) (PEO/PMMA) ($\Delta Tg \cong 180$ K), poly(styrene)/ poly(vinyl methyl ether) (PS/PVME) ($\Delta Tg \cong 110$ K) blends (Colby, 1989; Zawada et al., 1994; Dionisio et al., 2000; Lutz et al., 2003; Cendoya et al., 1999). α-

relaxations in miscible blends are typically broadened compared to the pure component response, which indicates that the range of dynamic time scales broadens on blending. One result of this is that time-temperature superposition (tTS) often fails in blends because the broadening increases as temperature is lowered.

As for secondary processes including the β-relaxation and side group rotations, they have not received as much attention as the α-process. Arbe et al. (1999) presented a quasielastic neutron scattering study on PI/PVME blends. They showed that for the blend component displaying the high *Tg*, i.e. PVE, the secondary β-like processes is not modified by blending. With the same technique, Arrighi et al. (1995) studied the methyl group rotation dynamics on two partially miscible blends: a blend of solution chlorinated polyethylene and poly(methyl methacrylate) (SCPE/PMMA) and a blend of polystyrene and poly(vinyl methyl ether) (PS/PVME). The rotational dynamics of the ether methyl group in PVME in blends with PS is very similar to that of the pure polymer, whereas a strong effect of blending on the ester methyl group in PMMA is observed in the SCPE/PMMA blend. It is pointed out that the weaker interaction between PS and PVME might be responsible for this difference. The effect of blending on local secondary processes is also investigated in head-to-head poly(propylene)/poly(ethylene-propylene) (hhPP/PEP) and PI/PVE systems (Pérez Aparicio et al., 2006; Mukhopadhyay et al., 1998). These data suggest that these localized processes are less affected by blending.

1.3 Theories of segmental dynamics in miscible polymer blends

The microscopic origins of the unusual observations in miscible polymer blends have been the subject of considerable debate in recent years. Concentration fluctuation and chain connectivity (the self-concentration effect) are two potential explanations. Both explanations state that the local environment is heterogeneous in the blend and a concentration, which differs from the bulk, is defined on a local length scale. The details of these two models are described below.

1.3.1 Concentration fluctuations

According to Zetsche and Fischer (1994), concentration fluctuations are driven purely by the statistical mechanics of the system and the distribution of concentration fluctuations in an incompressible polymer blend is given as

$$P(\phi) \propto \exp\left[-\frac{\left(\phi - \tilde{\phi}\right)^2}{2\left\langle (\Delta\phi)^2 \right\rangle} \right] \tag{1.5}$$

where $\tilde{\phi}$ is the mean blend composition, *P(ϕ)* the probability of finding a concentration fluctuation with composition ϕ, $\Delta\phi$ the concentration fluctuation, and $\left\langle (\Delta\phi)^2 \right\rangle$ the mean-squared value of the concentration fluctuation, which is defined by

$$\left\langle (\Delta\phi)^2 \right\rangle = \frac{S(0)}{V} \tag{1.6}$$

S(0) is the static structure factor at q (wave vector) = 0 and V is an appropriate control volume (Kumar et al., 1996; Kamath et al., 1999; Zetsche and Fischer, 1994).

It was postulated that the experimentally probed dynamics is related to relaxation processes occurring over a "cooperative" volume *V*, and its length scale is of key importance. Zetsche and Fischer (1994) assert the "cooperative" volume *V* is connected to a length scale ξ that governs the glass transition in the Donth model (Donth, 1982) and it is represented by the following equation,

$$V(\tilde{\phi}) \equiv \xi^3 = d_a^3 \left[\frac{T_\infty(\tilde{\phi})}{T - T_\infty(\tilde{\phi})} \right]^2 \tag{1.7}$$

where $T_\infty(\tilde{\phi})$ is the Vogel temperature of the blend and it is related to the glass transition temperature *Tg* of the bulk system by

$$T_\infty(\tilde{\phi}) = T_g(\tilde{\phi}) - c_2 \tag{1.8}$$

where c_2 is the WLF coefficient and d_a is a material-related constant.

Kumar et al. (1996) state that the distance from the local Vogel temperature, T-T_∞, which corresponds to a local composition, determines the cooperative volume. It means that the size of the cooperative volume increases with decreasing temperature and that the regions that are rich in the lower *Tg* component are associated with a smaller control volume. This model has successfully captured the broadening of relaxation times, but it fails to explain the distinct different component *Tg* in miscible polymer blends.

1.3.2 Chain connectivity

This model has been highlighted by Lodge and McLeish (2000). They state that each component's environment is rich in itself because it is connected to the segments of its own type and propose the Kuhn length as the relevant temperature and composition

independent length scale. They also introduced an effective local concentration which is given by

$$\phi_{eff} = \phi_s + (1 - \phi_s)\phi \tag{1.9}$$

where ϕ is the bulk concentration, ϕ_s is the self-concentration of the same component and is estimated by

$$\phi_s = \frac{C_\infty M_0}{k\rho N_A V} \tag{1.10}$$

where C_∞ is the characteristic ratio, M_0 is the repeat unit molar mass, k is the number of backbone bonds per repeat unit, ρ is the density, N_A is Avogadro's constant, and

$$V = l_k^3 \tag{1.11}$$

Here l_k is the Kuhn length.

This model has been tested on a large number of miscible polymer blends. It successfully explains some experimental observations in polymer blends, such as the broadening of glass transition temperature and the failure of time-temperature superposition.

The relative importance of concentration fluctuations and chain connectivity effects has been the subject of considerable debate in recent years. Kant et al. (2003) estimated this effect on several miscible polymer blends and a tetrablock copolymer. They found that chain connectivity provides a good description of the mean segmental dynamics at temperatures above the *Tg* of both pure components, while at lower temperatures, especially below the *Tg* of the pure high *Tg* component and above the blend *Tg*, the self concentration of the high *Tg* component is observed to decrease

monotonically and concentration fluctuations play an important role in this temperature range.

1.4 Literature on the dynamics of PEO/PMMA blends

The mixture of PEO and PMMA is characterized by large *Tg* contrast [$\Delta Tg \approx 185$ K] and minimal interactions (the Flory χ parameter is nearly zero) (Ito et al., 1987; Russell et al., 1988). This blend exhibits an amorphous phase for concentration of PEO less than 30 by weight. Common PEO is a linear molecule without side chains. Two side groups are present in PMMA: one is the α-methyl group; the other one is a large ester side group. Their structures are illustrated in Fig. 1.2, respectively. The side group associated motions make the relaxations in PMMA more complicated. Relaxation processes in PMMA include rotations of the ester and α-methyl groups, main chain motion, and the rotation of the entire ester side group. All these facts make this blend an excellent candidate in the study of miscible polymer blend dynamics.

Using oscillatory shear rheometry, Colby (1989) studied the temperature dependence of the terminal relaxation times for both components in blends with 20 and 30 wt% PEO. At any given temperature, the two relaxation times are shifted towards each other in the blend, but if considered at constant *T*-*Tg*, PMMA [the slow component] is less mobile in the blend. The PEO relaxes slightly faster, although the difference is small and could be interpreted as no change in mobility when blended. These results were obtained in the range *Tg* + 40 to *Tg* + 100 K. The data cannot be superposed and this is attributed to the separate friction factors for each component. Zawada et al. (1992)

used simultaneous measurements of infrared dichroism and birefringence to monitor the dynamic response of this blend with PEO contents ranging from 40 to 80%. In this composition range, PEO dynamics are slowed considerably at constant *T-Tg*, while the

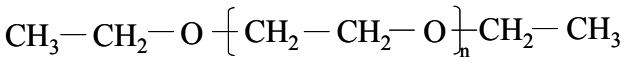

(a)

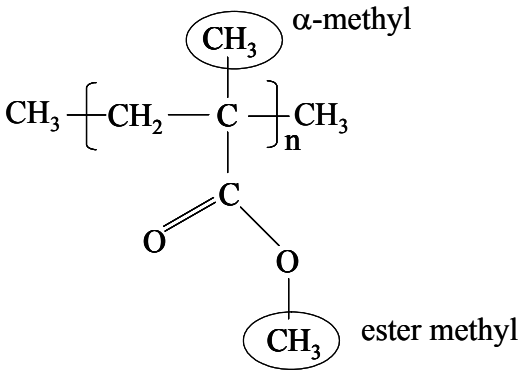

(b)

Fig. 1.2 Chemical structures of PEO (a) and PMMA (b).

change in PMMA dynamics is smaller and non-monotonic in composition. Dielectric spectroscopy (Dionísio et al., 2000) on blends with PEO contents up to 25 wt% shows that the merged $\alpha\beta$-relaxation process of PMMA becomes faster with addition of PEO, the low *Tg* component. This study also suggests that PEO motion is cooperative with the main chain of PMMA. In contrast, NMR on d_4PEO/PMMA blends with PEO contents of 3–30% has observed PEO motion that is up to 12 orders of magnitude faster than PMMA

motion at the blend *Tg*, and depends only weakly on composition, suggesting the motion of PEO measured by NMR is not coupled to that of PMMA (Lutz et al., 2003). These authors ascribe their observations to the lack of side groups in PEO allowing it to move freely on the segmental level, despite being surrounded by nearly immobile PMMA chains. Another explanation is provided by Kumar et al. (1996). Concentration fluctuations [which should be high in this blend due to its small χ parameter] temporarily create regions rich in PEO, which allow a large fraction of the PEO to relax unhindered by PMMA. Another fraction of the PEO would be expected to relax more slowly, consistent with the mean blend composition, leading to a bimodal distribution of relaxation times, as is sometimes observed for the low *Tg* component in miscible blends. All these results present a complicated composition dependence of component dynamics in this blend.

1.5 Motivation of this work

The dynamics of miscible polymer blends are of fundamental and practical relevance. To resolve the molecular origins of these effects, first problem to face is to isolate the dynamic response of different relaxation processes. It is difficult to retrieve specific local motions using commonly used experimental techniques, especially at high temperatures, because the response in a particular experiment includes all types of motion grouped together. For example, quasielastic neutron scattering can only detect the methyl group rotation at temperatures below 200 K (Arrighi et al., 1995a; 1995b). Dielectric spectrometer also needs to be operated below glass transition temperature *Tg* to capture

the β-relaxation (Bergman et al., 1998). Furthermore, we did some neutron spin echo measurements on PEO/PMMA blends as discussed in Chapter 4 (Farago et al., 2005). However, the collective motions occurring in polymers are far more beyond understanding. In addition, the fast time dynamics are missing in neutron spin echo measurements. To solve these problems, an investigation of PEO/PMMA system using molecular dynamics (MD) simulation is initiated in the work. Neutron scattering techniques, which cover the same time range as molecular dynamics simulations, are used to test the accuracy of simulation models.

In this thesis work, local motions in PMMA, which group together at temperatures above *Tg*, will be isolated using molecular dynamics simulations. In addition, the effect of blending on each specific motion in PMMA is investigated. As far as we know, only one paper so far presents some simulation work on the local dynamics of PEO/PMMA blend (Genix et al., 2005). In their work, they combine the quasielastic neutron scattering and atomistic molecular dynamics simulations to mainly focus on the investigation of PEO dynamics in the blend at temperatures close and above the blend *Tg*. They observe a significant slowing down of the PEO dynamics in the blend and that the fast PEO dynamics is confined in space to a volume of about 1 nm. In our work, in addition to the studies of the main chain dynamics of PEO and PMMA in the blend, we mainly focus on the effect of blending on the methyl group rotation and the β-relaxation of PMMA at temperatures above blend *Tg*.

1.6 Summary of other chapters

In Chapter 2 and 3, the molecular dynamics and neutron scattering techniques are introduced, respectively. The results from neutron spin echo measurements are summarized in Chapter 4. The validation of the PEO simulation model is given in Chapter 5, which also includes a detailed comparison of PEO structure and dynamics between united and explicit atom PEO simulation models, while in Chapter 6 the structure and dynamics of PMMA melts are discussed, as well as the method to isolate side group rotations and main chain motion. In Chapter 7, the effects of blending on methyl group rotations, the entire ester side group rotation, and the main chain motion are discussed. Finally in Chapter 8, a summary and future works are given.

Chapters 5 and 6 are adapted from manuscripts in print or accepted for publication at the time of writing. The findings in Chapter 5 are published in *Journal of Chemical Physics* 124: 234901/1-234901/11 (2006). Paper related to Chapter 6 has been accepted in *Macromolecules* for publication. Chapter 4 is partly adapted from the paper published in *Physical Review E* (Farago et al., 2005).

Chapter 2
Molecular Dynamics Technique

2.1 Introduction

Computer simulations have been recognized as a useful tool to explore the structure and dynamics of polymer systems. They provide detailed molecular information on a microscopic scale. This information (molecular geometry and microscopic interaction) is crucial in understanding the properties of polymer molecules of experimental interest. The connection between the microscopic simulation and macroscopic properties is made via statistical mechanics by relating the macroscopic properties with molecular structure and atom motions in the simulation system. In addition, computer simulation serves as a complement to experiments. Experiments are limited and expensive, while simulations are easy to perform and can be carried out under extreme temperatures and pressures that for experiments are impossible. One of the most important simulation techniques is molecular dynamics (MD). In the following sections, the main theory and algorithms involved in the molecular dynamics simulations as well as some simulation details are introduced.

2.2 Molecular dynamics theory

MD simulations are numerical solutions of classical Newton's equation of motion for the particles within the investigated system,

$$m_i \frac{d^2 \mathrm{r}_i}{dt^2} = \mathrm{F}_i(\mathrm{r}_1, \mathrm{r}_2, \cdots, \mathrm{r}_N), \quad i = 1, 2, \cdots, N. \tag{2.1}$$

Here F_i denotes the force acting on particle i under consideration, m_i its mass and r_i its position vector.

The forces F_i are derived from the potential energy function $U(\mathrm{r}_1, \mathrm{r}_2, \cdots, \mathrm{r}_N)$, which depends on the specific geometric arrangement of the particles,

$$\mathrm{F}_i(\mathrm{r}_1, \mathrm{r}_2, \cdots, \mathrm{r}_N) = -\nabla_{\mathrm{r}_i} U(\mathrm{r}_1, \mathrm{r}_2, \cdots, \mathrm{r}_N) \tag{2.2}$$

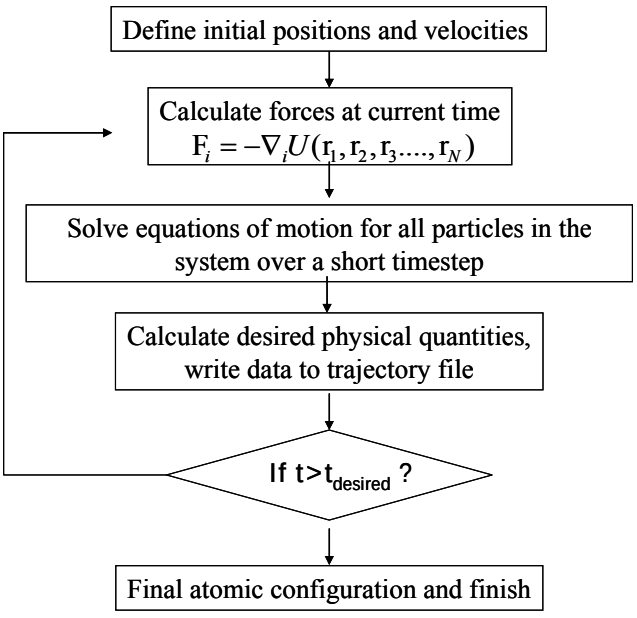

Fig. 2.1 A schematic of MD program.

The main principle of a Molecular Dynamics program is illustrated in Fig. 2.1. First the investigated system is initialized. The forces acting on every particle are computed based on the positions of all the particles in the system. Then after integrating Newton's equations of motion, the positions and velocities for the particles at time $t_0+\Delta t$

(Δt is the time step) are updated. The above procedure is repeated until the desired length of time is reached. After the loops finish, the trajectory of the particles in the system can be used to calculate some physical quantities and to determine the properties of the system. The force calculation and the integration of equations make up the core of the simulation work. Usually in MD, the force calculation is crucially important because given the force everything related to the properties of the investigated system can be calculated.

2.3 Interaction potential functions

Interactions present in polymer chains include bonded interactions, which are related to covalent bonds, and nonbonded interactions. Bonded interactions include bond stretching, bond angle bending and bond torsion. Nonbonded interactions consist of van der Waals and electrostatic. van der Waals force is commonly used to refer to forces that arise from the polarization of molecules into dipoles. The van der Waals particle itself is a temporary dipole with a slight negative charge on one side and a slight positive charge on the other. The electrostatic force appears between two or more charged particles. If both the particles are positively or negatively charged, the force is repulsive; if they are of opposite charge, it is attractive. These interactions can be expressed by the potential energy functions, which depend only on molecular positions of the investigated system. A typical example of the function is given as follows,

$$
\begin{aligned}
U(\mathrm{r}_1, \mathrm{r}_2, \cdots, \mathrm{r}_N) = & \sum_j \frac{k_j^{\,l}}{2}(l_j - l_j^{\,0})^2 && \text{(bond)} \\
& + \sum_j \frac{k_j^{\,\theta}}{2}(\theta_j - \theta_j^{\,0})^2 && \text{(angle)} \\
& + \sum_j \sum_0^k c_{kj} \cos^k \phi_j && \text{(torsion)} \\
& + \sum_{i,j=1}^N \varepsilon_{ij} \left[\left(\frac{\sigma_{ij}}{r_{ij}} \right)^{12} - 2 \left(\frac{\sigma_{ij}}{r_{ij}} \right)^6 \right] && \text{(van der Waals)} \\
& + \sum_{i,j=1}^N \frac{q_i q_j}{r_{ij}} && \text{(electrostatic)}
\end{aligned}
\tag{2.3}
$$

In the above equation, $k_j^{\,l}$ and $k_j^{\,\theta}$ are the constants related to bond stretching and bond angles. They are used to define the rigidness of the bond or angle. The higher the constant, the more difficult the bond or angle is to deform. l and θ are the bond length and bond angle, respectively. l^o and θ^0 represent the equilibrium bond length and bond angle. c_{kj} is the constant related to the deformation of torsions, ϕ the dihedral angle and k the number of energy minima present in the torsion structure. ε is the well depth, which governs the strength of van der Waals interaction and σ is a length scale at which the interaction energy is zero. q is the charge on the atom and r_{ij} is the distance between the non-bonded atom pair of i and j.

2.4 Integration of equation of motion

There are a few algorithms for propagating the motion of the particles in a simulation. Here we only look over the velocity VERLET algorithm, since it is used in

the current study. This algorithm is one of the modifications to the basic VERLET algorithm. The velocity VERLET algorithm stores positions, velocities and accelerations. The main advantages of this method are numerical stability, time-reversibility and simplicity. It is one of the most attractive methods so far.

$$\mathbf{r}(t+\Delta t) = \mathbf{r}(t) + \Delta t \cdot \mathbf{v}(t) + \frac{1}{2}\Delta t^2 \mathbf{a}(t) \tag{2.4}$$

$$\mathbf{v}(t+\Delta t) = \mathbf{v}(t) + \frac{1}{2}\Delta t \cdot [\mathbf{a}(t) + \mathbf{a}(t+\Delta t)] \tag{2.5}$$

In the molecular dynamics simulation, we should be careful in choosing the desired time step. Using a large time step can save computer run time for a specific problem. However, the computational error is also increased. Furthermore, for too large of time step, some atoms may move into regions where the potential energy is prohibitively high, and the simulation becomes unstable. The rule of thumb is to choose the time step to be an order of magnitude less than the smallest time scale of the system, i.e., the period of the fastest motion.

2.5 Techniques used in the current simulation programs

The techniques used in the current molecular dynamics simulations are described below.

2.5.1 Periodic boundary conditions

When we run simulation programs to study the properties of a system in bulk, there are a lot of particles that are near the surface of the investigated system which we

are not interested in. To avoid the surface effects, the system size needs to be large enough to ensure that the surface effects on the bulk properties can be neglected which, is extremely computationally expensive.

To solve this problem, periodic boundary conditions, which are shown schematically in Fig. 2.2, are used. The periodic boundary makes a simulation that consists of only a few hundred atoms behave as if it is infinite in size, thus, the surface effect is removed. In periodic boundary conditions, the simulation box is replicated throughout space. Each particle has an image in each replicated box. The particle in the central box moves with exactly the same orientation and velocity with all its periodic images in other boxes. Therefore, when a particle leaves the central box, one of its images will enter through the opposite face, otherwise when one of the images moves into the central box, the corresponding particle will leave the box instantaneously. This technique enables us just store the positions of all the particles in the central box and there is no need to consider the infinite number of images in a simulation, which greatly saves computation time.

In the simulation program, the periodic boundary condition is considered in both the integration of equations of motion and the force calculations. The particle coordinates are examined at every time step. If one particle moves out of the simulation box, the particle has to be taken inside to keep it in the box. When we calculate the force interaction, we have to include all the interactions of one particle with all the other particles in the central box and all the images in the surrounding boxes. It is impossible to accomplish since it include an infinite number of images. For the short-ranged

interactions, the force calculation can be restricted to a small range, for example, within a circle of radius of r_c as shown in Fig. 2.2.

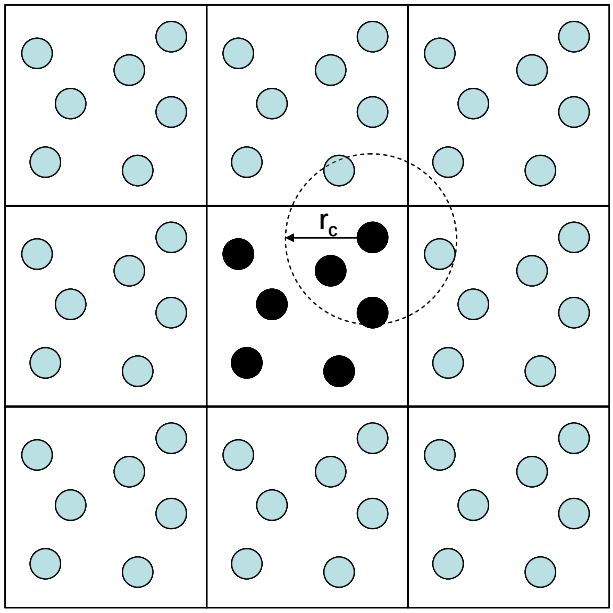

Fig. 2.2 Periodical boundary conditions. The central box is represented by 7 gray particles.

2.5.2 Berendsen thermostat

In this work, the molecular dynamics simulations are implemented in the canonical (NVT) ensemble, which is characterized by a fixed number of atoms, *N*, a fixed volume, *V*, and a fixed temperature, *T*. This ensemble corresponds to the common experimental conditions. At the same time it prevents the long-time temperature drift problem which often happens in the microcanonical (NVE) ensemble when the long run time is required, where the total energy is conserved (Mudi and Chakravarty, 2004).

Constant temperature in this work is ensured by Berendsen's method. The basic idea is to rescale velocities to achieve a mean kinetic energy consistent with the desired temperature by weakly coupling the system to an external bath. It works as follows: the velocities of the particles are adjusted at each time step by a factor that depends on the instantaneous temperature (T), the desired target temperature (T_d) and an adjustable time scale factor τ which indicates how fast the temperature is corrected (Berendsen et al., 1984),

$$\lambda = \left[1 + \frac{\Delta t}{\tau} \left(\frac{T_d}{T} - 1 \right) \right]^{1/2} \tag{2.6}$$

This method can be easily incorporated in the Verlet algorithm. By varying the time constant τ, we can decrease or increase the degree of coupling to an external bath. When $\tau \to \infty$, λ is 1, which represents the microcanonical ensemble (Mudi and Chakravarty, 2004).

2.5.3 Truncated and shifted van der Waals potential

The Lennard-Jones (LJ) potential, an example of which is plotted in Fig. 2.3, is often used as an approximate model for the van der Waals interactions between two neutral particles in molecules,

$$u(r_{ij}) = \varepsilon \left[\left(\frac{\sigma}{r_{ij}} \right)^{12} - 2 \left(\frac{\sigma}{r_{ij}} \right)^{6} \right] \tag{2.7}$$

When two particles are put far apart, they are weakly polarized and the attraction is generated between each other. When they get too close, there is a significant overlap in

the electron clouds, which results in a repulsive potential. The attractive and repulsive parts of the Lennard-Jones particle, also indicated in Fig. 2.3, are represented by,

$$u^a(r_{ij}) = -2\varepsilon\left(\frac{\sigma}{r_{ij}}\right)^6 \tag{2.8}$$

and

$$u^r(r_{ij}) = \varepsilon\left(\frac{\sigma}{r_{ij}}\right)^{12} \tag{2.9}$$

respectively.

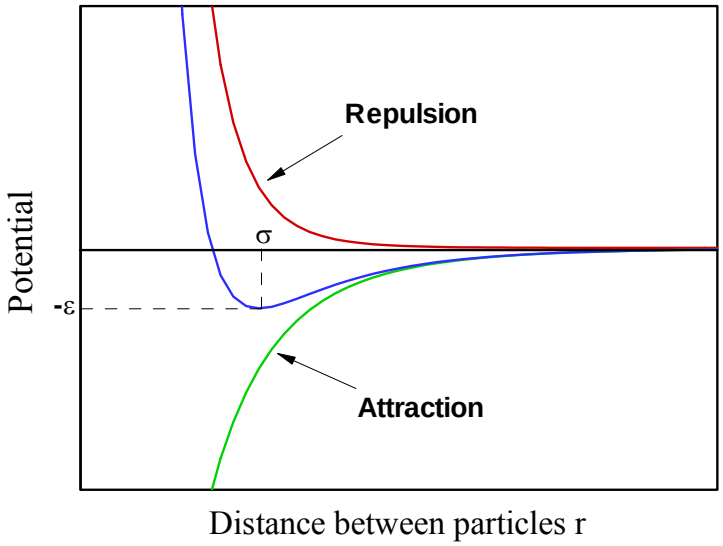

Fig. 2.3 Illustration of a Lennard-Jones potential.

As shown in Fig. 2.3, a long tail is observed in Lennard-Jones potentials. To save computational time, potential truncations are often applied in a simulation. The simplest method is to ignore the interactions beyond cut-off distance r_c, which means that we can

only calculate the total potential energy of a given particle with its neighboring particles that are closer than the cut-off distance. Then the potential is simulated as below,

$$u^{trunc}(r_{ij}) = \begin{cases} u(r_{ij}) & r \le r_c \\ 0 & r > r_c \end{cases} \tag{2.10}$$

The larger the r_c, the smaller the cut-off potential, while at the same time r_c should be chosen to be less than half the diameter of the simulation box in periodic boundary conditions because a given particle can only interact with the nearest periodical images of all the other particles. This method may result in a systematic error in estimating the potential energy of the true Lennard-Jones potential. Moreover, a discontinuity of potential is introduced at $r = r_c$. When a pair of particles crosses this boundary, the total energy is not conserved. To avoid this problem, in this work the potential is shifted so that the potential is zero at $r = r_c$ as follows,

$$u^{trunc}(r_{ij}) = \begin{cases} u(r_{ij}) - u(r_c) & r \le r_c \\ 0 & r > r_c \end{cases} \tag{2.11}$$

The introduced term $u(r_c)$ is constant for any pair interaction, and it does not affect the forces.

2.5.4 Ewald summation

As discussed in Section 2.3, the electrostatic force is normally expressed in Coulomb's law,

$$U(\mathrm{r}_1, \mathrm{r}_2, \cdots, \mathrm{r}_N) = \sum_{i<j}^{N} \frac{q_i q_j}{r_{ij}} \tag{2.12}$$

This equation shows that Coulomb force is proportional to r^{-2}. As discussed in Section 2.5.3, the long-range Lennard-Jones interactions can be truncated at $r = r_c$ to reduce the computer effort. But we cannot do the same trick to the Coulomb force since it decays much slower than Lennard-Jones potential and the interaction range becomes so larger that the long-range Coulomb force cannot be neglected. Therefore, the total energy of a system of N particles in a cubic simulation box of size L and their infinite replicas in periodic boundary conditions is represented by

$$U = \frac{1}{2} \sum_{\mathbf{n}}{}' \sum_{i,j=1}^{N} \frac{q_i q_j}{\left|\mathbf{r}_{ij} + L\mathbf{n}\right|} \tag{2.13}$$

The sum is over all integer vectors **n** and the primer indicates that terms with $i = j$ are omitted when $\mathbf{n} = 0$. The above summation is conditionally convergent, which means that the result depends on the order of summation. Furthermore, since this calculation is over a large range of image boxes, the solution is extremely computationally expensive and even insolvable.

To handle the above long-range problems, in this simulation work the Ewald summation technique is employed. Ewald summation was originally developed by Ewald [Ewald, 1921] as a technique to efficiently sum the interaction between an ion and all its periodical images. It reorganizes Eq. (2.13) into two rapidly converging series plus a constant term. The total Coulomb potential is written as the sum of the real space part (U^r), the imaginary part (U^k) and the constant part (U^s),

$$U^r = \frac{1}{4\pi\varepsilon_0} \sum_{\mathbf{n}}{}' \sum_{1 \le i \le j \le N} q_i q_j \frac{erfc\left(\alpha\left|\mathbf{r}_{ij} + L\mathbf{n}\right|\right)}{\left|\mathbf{r}_{ij} + L\mathbf{n}\right|} \tag{2.14}$$

$$U^k = \frac{1}{2\varepsilon_0 V}\sum_{\mathrm{k}\neq 0}\frac{1}{\mathrm{k}^2}e^{-\frac{k^2}{4\alpha^2}}\left\{\left|\sum_{i=1}^{N} q_i \cos(\mathrm{k}\cdot\mathrm{r}_i)\right|^2 + \left|\sum_{i=1}^{N} q_i \sin(\mathrm{k}\cdot\mathrm{r}_i)\right|^2\right\} \tag{2.15}$$

$$U^c = -\frac{1}{8\varepsilon_0 V\alpha^2}\left|\sum_{i=1}^{N} q_i\right|^2 \tag{2.16}$$

V is the volume of the simulation box, **k** the reciprocal-space vector, and erfc() the complimentary error function which decrease monotonically with x and is defined as

$$\begin{aligned} erfc(x) &= 1 - erf(x) \\ &= 1 - \frac{2}{\sqrt{\pi}}\int_0^x e^{-u^2} du \end{aligned} \tag{2.17}$$

The physical explanation of the decomposition is as follows. In the Ewald method, each point charge is surrounded by a charge distribution of equal magnitude and opposite sign which is assumed to be Gaussian,

$$\rho_i(r) = q_i\alpha^3 \exp(-\alpha^2 r^2)/\sqrt{\pi^3} \tag{2.18}$$

where α determines the width of the distribution, and r is the position relative to the center of distribution. This introduced Gaussian distribution screens the interactions between neighboring charges. The total screened potential becomes the real space part of the Ewald sum (U^r), which is now short-ranged. To cancel out the induced Gaussian distribution, a charge distribution of the same sign and magnitude as the original charge is added. This canceling distribution is summed in reciprocal space and makes up the reciprocal space part of the Ewald sum (U^k). U^c is the self energy term that corrects the overcounting in the reciprocal space.

This method is more expensive than the truncation method used in Lennard-Jones potential, but it preserves the long-range character of Coulomb force. It should be careful

to choose the parameters used in both real and reciprocal series. The parameter α determines how fast the real part decreases. A large value of α corresponds to a sharp distribution of charge, but more terms need to be included in *k*-space. A typical value of α is $5/L$ and a spherical cutoff of 5 is imposed on the *k*-space.

2.5.5 Techniques that tackle time scale problems

In simulations of molecular systems, the various time scales are present. There will be a fast time scale arising from the local motions within the molecule which are related to bond and bend vibrations and dihedral angle motions, an intermediate time scale arising from the short-ranged nonbonded intermolecular interactions, and a slow time scale arising from the long-range interactions. The differences between the time scales are usually several orders. Thus to set the time step based on the fastest motion may be a waste of time for other motions. Therefore, techniques are developed to solve this time-scale problem (Frenkel and Smit, 2002). In this work, two techniques have been used: constraints and multiple time steps.

2.5.5.1 Constraints

The basic idea of constraint dynamics is to freeze the bonds (sometimes, the angles) in molecules with smaller time scales by setting geometrical constraints so that a much larger time step can be chosen.

Consider a molecule whose structure is subject to one or more bond length constraints. Assuming there are a total of n_c distance constraints imposed on the

molecule, and if the *k*th constraint acts between atoms *i*(*k*) and *j*(*k*), these constraints can then be summarized by the following set of equations,

$$\sigma_k = r_{ij}^2 - d_{ij}^2 \tag{2.19}$$

Here r_{ij} represents the actual *k*th bond length and d_{ij} the desired *k*th bond length.

The equations of motion can be written as,

$$m_i \ddot{\mathrm{r}}_i = \mathrm{F}_i + \mathrm{G}_i \tag{2.20}$$

where $\mathbf{F}_i$ is the usual force term which accounts for all the non-constraint interactions, and $\mathbf{G}_\mathrm{i}$, usually called as constraint force, is an additional force-like term that accounts for the effect of the constraints. It can be expressed as below by introducing Lagrange multipliers λ_k :

$$\mathbf{G}_i = -\sum_{k \in C(i)} \lambda_k \nabla_{\mathrm{r}_i} \sigma_k = -\sum_{k \in C(i)} 2\lambda_k \mathbf{r}_{ij} \tag{2.21}$$

where *C(i)* denotes the set of constrains that involve atom *i*, and $\mathbf{r}_{ij} = \mathbf{r}_i - \mathbf{r}_j$.

Particle positions and the multipliers can be calculated from the above equations together with the constraint equations.

These equations can be solved either by the direct matrix method or by the relaxation method. In the direct matrix method, the equations of motion are solved together with the constraints. This entails expressing the constraint equations in matrix form and then solving the resulting linear algebra problem using standard numerical techniques. The satisfaction of the constraints is thus subject to numerical error. The relaxation method, which is a particularly simple one, is to advance the system over a single time step by integrating the unconstrained equations of motion and then adjusting the coordinates and/or velocities until the constraints are satisfied to a pre-specified

accuracy. In this way, the constraints can be satisfied even better than that in the direct matrix method. The most widely used relaxation methods are the SHAKE algorithm and its variant the RATTLE algorithm**.** In this work, we used the RATTLE algorithm, in which the velocities are corrected as well as the coordinates, thereby ensuring that the atoms have zero relative velocity along the direction of their mutual constraint. In addition, this method is proposed based on the velocity VERLET integration algorithm. It is a two-stage process and there are two kinds of constraints. One is distance constraint as described previously.

$$\sigma_k = 0 \tag{2.22}$$

The other is a velocity constraint,

$$\dot{\sigma}_k = 2\dot{\mathbf{r}}_{ij} \cdot \mathbf{r}_{ij} = 2(\mathbf{v}_i - \mathbf{v}_j) \cdot (\mathbf{r}_i - \mathbf{r}_j) = 0 \tag{2.23}$$

The artificial position and velocity are obtained first in the absence of constraint and are then corrected accordingly.

$$\dot{\sigma}_k = 2\dot{\mathbf{r}}_{ij} \cdot \mathbf{r}_{ij} = 2(\mathbf{v}_i - \mathbf{v}_j) \cdot (\mathbf{r}_i - \mathbf{r}_j) = 0 \tag{2.24}$$

The position correction parameter is calculated as,

$$\lambda = \frac{r_{ij}^{\ 2} - d_{ij}^{\ 2}}{4\Delta t^2 (1/m_i + 1/m_j) \cdot (\mathbf{r}_{ij} \cdot \tilde{\mathbf{r}}_{ij})} \tag{2.25}$$

And the velocity correction parameter is calculated as,

$$\beta = \frac{\mathbf{v}_{ij} \cdot \mathbf{r}_{ij}}{2d_{ij}^{\ 2}(1/m_i + 1/m_j)} \tag{2.26}$$

Here $\mathbf{r}_{ij}$ and $\mathbf{v}_{ij}$ are the intermediate or artificial position and velocity which could be reached in the absence of any constraint. $\tilde{\mathbf{r}}_{ij}$ is the position which could be reached with constraint.

2.5.5.2 Multiple time steps

The multiple time step technique is an alternate method to deal with those high frequency vibrations in polymer systems. The physics under multiple time step algorithms is that different forces can be integrated with different time steps. Normally the fast forces are simple and fast to compute, while the slow forces are computationally expensive. With multiple time steps, a short time step can be given to the fast forces and a large one to the slow forces.

Multiple time steps are based on the Liouville formulation of the equations of motion. The derivation of this algorithm has been described in many papers (Tuckerman and Berne, 1992; Komeiji and Uebayasi, 1997). Here, we explain how to implement it in the simulation work. The forces are divided into fast processes (f_f) which include the bond stretching, angle vibration, and dihedral angle motion, medium processes (f_m) which are associated with the short-ranged non-bonded interaction and slow ones (f_s) which arise from the long range non-bonded interactions. Their corresponding time steps are Δt_f, Δt_m and Δt_s, respectively. In the following a piece of code is provided to illuminate the basic idea of the multiple time step method.

```
DO i = 1, n1
  v = v + fs/m*Δts/2          ! long range non-bonded
  Do j = 1, n2
    v = v + fm/m*Δtm/2        ! short range non-bonded
```

```
    do k = 1, n3
      v = v + ff/m*Δtf/2      ! short range non-bonded
      x = x + Δtf * v
      call force(ff)          ! fast-process force
      v = v + ff/m*Δtf/2
    enddo
    call force(fm)            ! medium-process force
    v = v + fm/m*Δtm/2
  Enddo
  call force(fs)              ! slow-process force
    v = v + fs/m*Δts/2
ENDDO
```

In the above program, the slow-process force (f_s) is evaluated n_1 times, while the medium-process force (f_m) is evaluated n_1*n_2 times and the fast-process force (f_f) $n_1*n_2*n_3$ times. Therefore, the computation time is significantly saved by computing fewer times of time-consuming slow processes.

2.6 Code validation

The MD main programs, as well as the programs used for the post data analysis, are all self-written. The main program developed through a few versions. The following lists the validation of some important versions.

2.6.1 Lennard-Jones fluid model

The main program is first tested on a very simple molecule, i.e. Argon molecule. This molecule is assumed as the Lennard-Jones fluid and only the van der Waals interaction is considered. The radial distribution function, which will be explained in

Section 2.8.2.3, is calculated and illustrated in Fig. 2.4. It is in good agreement with that reported in literature (Frenkel and Smit, 2002).

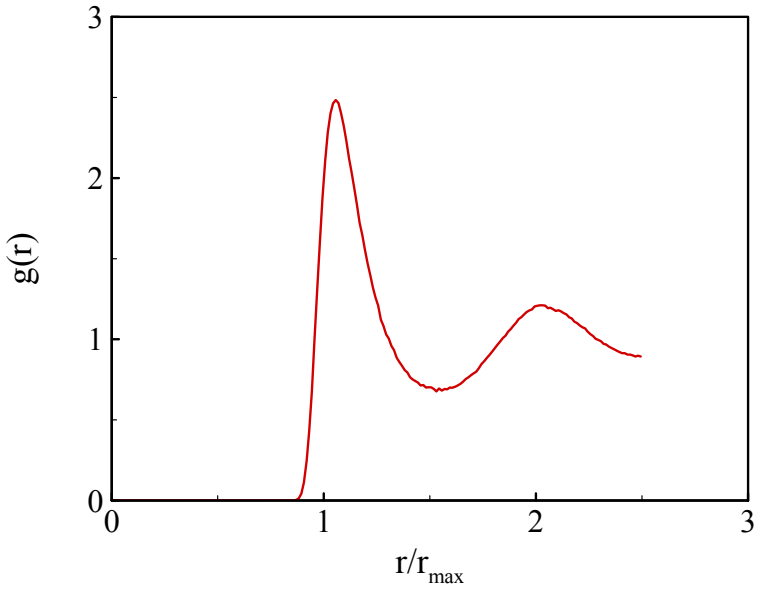

Fig. 2.4 Radial distribution function of Argon at $T = 87$ K ($r_{max} = 3.405$ Å).

2.6.2 Constraints dynamics simulation model

A case has been studied by considering a system of diatomic Lennard-Jones molecules to evaluate the efficiency of the RATTLE constraints by comparing two models. The first model uses a fixed bond length while the second one uses the direct bond stretching potential. In this study, the average deviation of the initial energy, which measures the accuracy of the integrator, is calculated,

$$\beta_E = \frac{1}{N}\sum_{i=1}^{N}\left|\frac{E(i\Delta t) - E(0)}{E(0)}\right| \tag{2.27}$$

where $E(0)$ is the initial energy, $E(i\Delta t)$ is the total energy at time $i\Delta t$, and N is the run steps.

Figure 2.5 gives the energy fluctuations β_E as a function of time step. From this figure, we can see that at the same time step constraint model always gives a lower β_E, which means that constraint model gives higher energy accuracy than the non-constraint model. For the similar energy noise level, for example 10^{-4}, it corresponds to the time step of 0.5 fs for non-constraint model and for constraint model, it can be obtained with a time step of 1 fs, which is a factor of 2 larger.

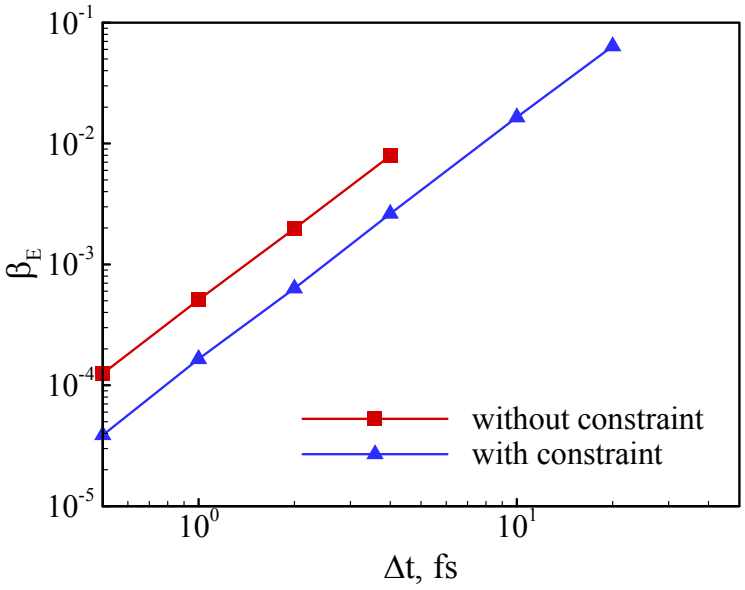

Fig. 2.5 Comparison of the energy fluctuations as a function of the time step for a normal MD simulation with a harmonic bond potential and a constrained one with RATTLE algorithm.

2.6.3 Polyethylene simulation model

Polyethylene is a very simple chain molecule, in which the electrostatic interaction between atoms can be neglected. In addition, a lot of simulation work has been done on this polymer. It is easier to find some results to compare with. Figure 2.6

presents the intermediate scattering functions of polyethylene with and without constraints using the current simulation program, and their comparison to the results from a validated model (Maranas et al., 1998) at two q values of 2.1 $Å^{-1}$ and 1.0 $Å^{-1}$. These comparisons indicate that constraint dynamics doesn't affect polymer dynamics. At the same time, the consistency of my results with previous ones validates our simulation program.

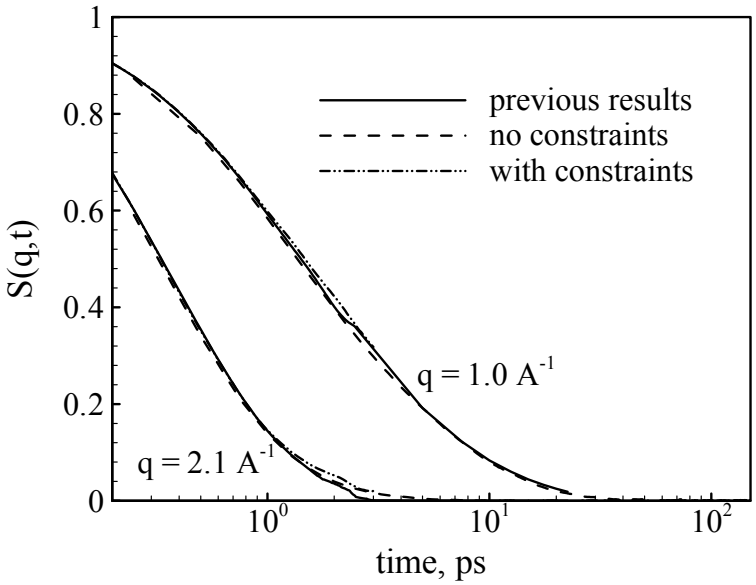

Fig. 2.6 The intermediate scattering functions of PE w/o constraints and their comparison to the results from a validated model.

2.6.4 Poly(ethylene oxide) simulation model

The accuracy of the "constraints" and "multiple time step" algorithm was evaluated on PEO simulations. Figure 2.7 gives the intermediate scattering functions of PEO with constraints and multiple time steps, where the bond lengths are not constrained.

No significant difference is observed, which validates the multiple time step algorithm and our simulation program. At the same efficiency, the program with multiple time step algorithm is about 3 times faster than that with constraints dynamics in PEO case.

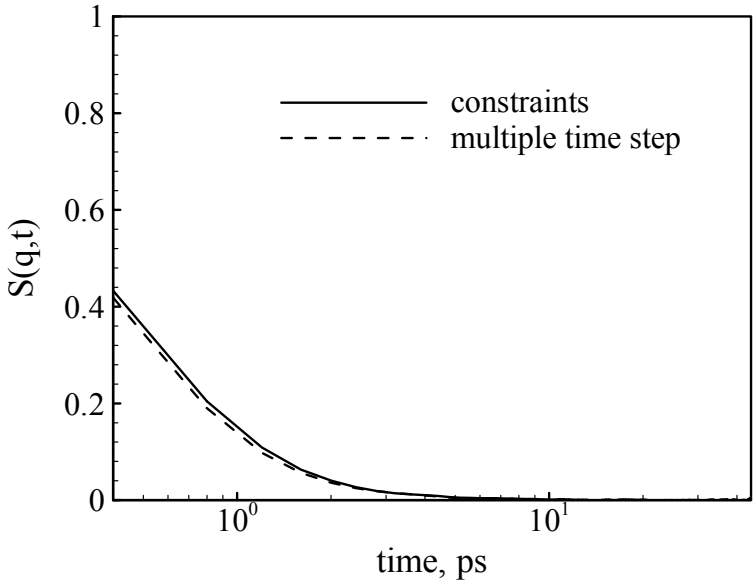

Fig. 2.7 The intermediate scattering functions of PEO calculated from programs with constraints or multiple time steps.

2.7 Simulation model setup

In the course of thesis work, two levels of simulation models are considered. They are united atom (UA) and explicit model (EA). A united atom model treats C, CH, CH_2, CH_3, and O in the molecules as one single unit, while in an explicit model all atoms including hydrogen atoms are considered as individual interaction sites. Simulation setup starts from the united atom model of pure components. The initial configurations for united atom model are generated as follows.

One single chain is first generated in an all-trans configuration. (For syndiotactic PMMA, the sequence also needs to be considered. In the current work, PMMA structure with a sequence of 100% syndiotactic is constructed, which means that the ester side groups are on the opposite side of the stretched PMMA chain.) This chain is copied and then rotated to produce different conformations. The generated multiple chains are placed in a large cubic box to ensure that the chains are not overlapping. Then the MD program starts to run with the box size reducing to its desired value, which is determined by the desired density of the system,

$$L = \left(\frac{m}{\rho} \right)^{\frac{1}{3}} \tag{2.28}$$

This relaxation process normally takes 1 ns. After the box reaches its desired size, a few more nanosecond simulation run is allowed. The structure and dynamics of the investigated system are checked over 2 or 3 ns simulation blocks to ensure the system approaches equilibrium. Once equilibrium is reached, data collection begins. These data can be used not only for the property calculation, but also for the starting configuration for the UA model of the blend and the EA model for pure components. Two sets of data are recorded at every time step: one stores the real atom coordinates, which is for the calculation of dynamical properties; the other one stores the periodical coordinates, which is for the calculation of structural properties.

The initial configuration of UA model for the PEO/PMMA blends starts with the equilibrated pure PEO and PMMA chains. The desired number of PEO and PMMA chains, which make up the desired concentration of the blend, are chosen and randomly

placed into the individual cells of a large cubic box. Then the box is shrunk as described above. The simulation is run for enough time to equilibrate.

The initial configuration of the EA simulation for pure components is obtained from the carbon and oxygen atom positions from the equilibrated UA simulation with hydrogen atoms inserted afterwards. The insertion method is illustrated in Fig. 2.8 with PEO as an example. For CH_2 group, we first find the bonds [in PEO case, they are C-C and C-O bonds; in PMMA case, they are C-C and C-C bonds] that connect the central C in united atom model. Second, the hydrogen atoms are placed symmetrically about the plane C-C-O by fixing the angle φ between the C-H bonds and C-C or C-O bonds at 110° and C-H the bond length l at 1.09 $Å^{-1}$. For CH_3 group, we first find the bond linking the CH_3 group [in PEO case, it's C-C bond; in PMMA case, it's C-C (α-methyl) or C-O bond (ester methyl)], then place one hydrogen atom randomly around the central C by just constraining the angle φ between C-H and C-C bonds at 110° and the C-H bond length l at 1.09 $Å^{-1}$; the other two hydrogen atom positions are obtained by fixing the angle φ between C-H bonds and the existing C-C or C-H bonds at 110° and the C-H bond length l at 1.09 $Å^{-1}$.

(a) (b)

Fig. 2.8 Determination of hydrogen atom positions: (a) for CH_2 group; (b) for CH_3 group.

Similarly, to start an EA model for the blend, hydrogen atoms are inserted to the equilibrated carbon and oxygen atom positions from UA model as described above. Then the simulation is allowed to run for a few nanoseconds to relax the bonds and angles, even some large backbone readjustments.

2.8 Calculation of equilibrium properties

2.8.1 Thermodynamic properties

2.8.1.1 Temperature

Temperature is calculated from the total kinetic energy of the system,

$$T(t) = \sum_{i=1}^{N} \frac{m_i v_i^2(t)}{k_B N_f} \tag{2.29}$$

where k_B is the Boltzmann constant, N the total number of atoms in the system and N_f the number of degree of freedom.

Note that there is a difference when calculating N_f for polymer chains with and without constraints. Assuming there are N_c number of chains with N_a atoms per chain, the total number of atoms N is equal to $N_c \cdot N_a$.

Without constraints,

$$N_f = 3 \cdot N - 3 \tag{2.30}$$

With constraints (i.e. the bond lengths are constrained to fixed values),

$$\begin{aligned} N_f &= \left[3 + (N_a - 1) \cdot (3 - 1)\right] \cdot N_c - 3 \\ &= 2 \cdot N + N_c - 3 \end{aligned} \tag{2.31}$$

2.8.1.2 Pressure

Pressure is defined as,

$$P = \frac{N}{V} k_B T - \frac{1}{3V} \left\langle \sum_i \sum_{j>i} \frac{\partial U}{\partial \mathrm{r_{ij}}} \cdot \mathrm{r_{ij}} \right\rangle \tag{2.32}$$

where T is the instantaneous temperature, and V the volume of the system.

2.8.1.3 Total energy

The total energy is the sum of kinetic and potential energy in the system,

$$E = E_k + U_p = \frac{3}{2} N k_B T + \left\langle \sum_i \sum_{j>i} U(\mathrm{r_{ij}}) \right\rangle \tag{2.33}$$

where E_k is the kinetic energy, U_p the total potential of the system, and $U(r_{ij})$ the potential between atom i and atom j.

2.8.2 Chain dimensions and packing

2.8.2.1 Radius of gyration (Rg)

The radius of gyration is determined using

$$Rg = \left\langle \sqrt{\frac{\sum_i m_i (r_i - r_{CM})^2}{M}} \right\rangle \tag{2.34}$$

The summation is taken over all the units in a chain [total chain mass M, atom mass m_i], and the average is taken over many coordinate snapshots. The position of unit i is indicated by r_i and the center of mass r_{CM} of each chain is

$$r_{CM} = \frac{\sum_i m_i r_i}{M} \tag{2.35}$$

2.8.2.2 End-to-end distance (Re)

The end-to-end distance is calculated from

$$\mathrm{R}e = < |r_1 - r_n| > \tag{2.36}$$

where r_1 and r_n are the positions of the first and last carbon atoms on a chain. This calculation is also averaged over many coordinate snapshots.

2.8.2.3 Radial distribution function g(r)

The radial distribution function (RDF or *g(r)*) provides structural information about the system. It is defined as the probability of finding a pair of molecules at a distance *r* apart, relative to the probability expected for an ideal gas of the same density.

$$g(r) = \frac{\langle N(r, \Delta r) \rangle}{\frac{1}{2} N \rho V(r, \Delta r)} \tag{2.37}$$

where ρ is macroscopic density, *N* is the total number of atoms in the system, $V(r,\Delta r)$ is the volume of a shell with width Δr at distance *r*, and $N(r,\Delta r)$ is the number of atoms in the shell. The average is taken over all the atoms in the system. For the intermolecular *g(r)*, only the pairs on different molecules are counted and pairs on the same molecule are counted for the intramolecular *g(r)*.

Within a computer simulation, the calculation of *g(r)* is implemented as described below. The volume around each particle is divided into concentric spherical shells. The number of atoms found in each shell is counted and stored. At the end of the simulation,

the average number of atoms in each shell is calculated. Then it is divided by the shell volume and the overall density to obtain *g(r)*. This results in *g(r)* approach unity at large distance *r*. For polymer molecules, at distances shorter than the bond length the radial distribution function approaches zero, since two particles cannot come closer than the bond length.

2.8.2.4 Static structure factor

An atomistic static structure factor *S(q)* of an isotropic sample is calculated by (Borodin et al., 2003)

$$S(q)=\frac{n}{\left\langle |b|^2 \right\rangle}\sum_i\sum_j c_i c_j b_i b_j \int_0^\infty [g_{ij}(r)-1]\frac{\sin qr}{qr}4\pi r^2 dr \tag{2.38}$$

where

$$\left\langle |b|^2 \right\rangle = \sum_i c_i |b_i|^2 \tag{2.39}$$

In the above, *i* and *j* represent different atomic species, the coherent scattering length *b* describes the interaction between neutron and nucleus, *c* is the atomic species concentration, and the radial distribution function $g_{ij}(r)$ reflects the local packing between atoms of types *i* and *j*. *q* is the momentum transfer, which is related to the spatial scale by

$$q=\frac{2\pi}{r} \tag{2.40}$$

2.8.3 Dynamics

2.8.3.1 Mean square displacement (MSD)

The mean squared displacement of individual atoms is evaluated by

$$MSD = \left\langle \left| r_i(t + t_0) - r_i(t_0) \right|^2 \right\rangle \tag{2.41}$$

where $r_i(t)$ is the position of atom i at time t and the average is taken over all atoms and multiple time origins t_0.

2.8.3.2 Self-intermediate scattering function

The definition of self-intermediate scattering function $S(q,t)$ is

$$\begin{aligned} S(q,t) &= \frac{1}{N}\left\langle \sum_{i=1}^{N} \exp(-i\mathrm{q}\cdot(\mathrm{r}_i(t+t_0) - \mathrm{r}_i(t_0))) \right\rangle \\ &= \frac{1}{N}\left\langle \sum_{i=1}^{N} \exp(-i\mathrm{q}\cdot\mathrm{r}) \right\rangle \end{aligned} \tag{2.42}$$

where $\mathrm{r}_i(t+t_0)$ is the position vector of atom i at time $t+t_0$, and r the vector between times $t+t_0$ and t. This function represents the self-correlation between the positions of atoms at times $t+t_0$ with respect to their positions at time t.

Assuming that the system is isotropic, there are two ways to calculate the self-intermediate scattering function. One is

$$\begin{aligned} S(q,t) &= \frac{1}{N}\left\langle \sum_{i=1}^{N} \exp(-i\mathrm{q}\cdot\mathrm{r}) \right\rangle \\ &= \frac{1}{N}\left\langle \sum_{i=1}^{N} \exp(-iqr\cos\theta) \right\rangle \\ &= \frac{1}{N}\left\langle \sum_{i=1}^{N} \exp(-iqx) \right\rangle \end{aligned} \tag{2.43}$$

where *S(q,t)* is the real part of the above equation and *x* is the *x* coordinate of r.

The other is

$$S(q,t) = \frac{1}{N}\left\langle \sum_{i=1}^{N} \frac{\sin(qr)}{qr} \right\rangle \tag{2.44}$$

Figure 2.9 demonstrates that the two methods are equivalent by giving exactly the same results.

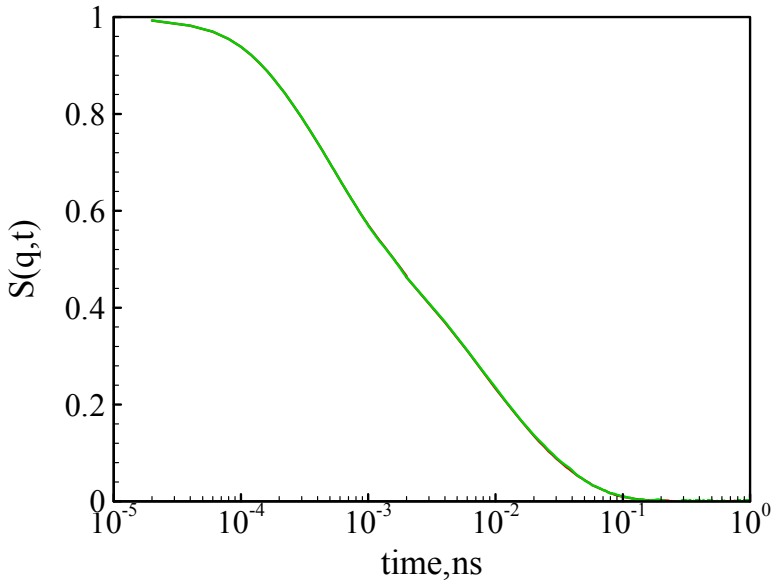

Fig. 2.9 Comparison of self-motion intermediate function *S(q,t)* calculated from the above two methods for PEO at $T = 343$ K and $q = 1.5$ Å^{-1}.

2.8.3.3 Collective intermediate scattering function

The definition of collective intermediate scattering function $S_c(q,t)$ is

$$S_c(q,t) = \frac{1}{N}\left\langle \sum_{j=1}^{N}\sum_{i=1}^{N} \exp(-i\mathrm{q}(\mathrm{r}_i(t+t_0) - \mathrm{r}_j(t_0))) \right\rangle \tag{2.45}$$

The average is taken over all atom pairs. It describes the relative correlation of particle *i* at time $t + t_0$ with respect to all the other particles at time t_0.

2.8.3.4 Orientation autocorrelation function (OACF)

The orientation autocorrelation function is the frequency Fourier transform of a spectral density function $J(\omega)$ which is measurable in NMR experiments (Lutz et al., 2003). It describes the decorrelation of the orientation of the C-H bond vector:

$$G(t) = \frac{3}{2}\left\langle \cos^2 \theta(t) \right\rangle - \frac{1}{2} \tag{2.46}$$

where $\theta(t)$ is the angle of the C-H bond at time t relative to its orientation at $t = 0$.

2.9 Data interpretation

To characterize motions in polymers, it is necessary to employ a fitting procedure that gives the average relaxation times and the width of a distribution of relaxation times on the time decay functions. In the course of thesis work, an empirical Kolrausch-Williams-Watts (KWW) equation is used (Phillips, 1996),

$$S(q,t) = A(q,T)\exp\left[-\left(\frac{t}{\tau_{KWW}(q,T)} \right)^{\beta(q,T)} \right] \tag{2.47}$$

where A is a prefactor, τ_{KWW} is the characteristic relaxation time, and β is the stretching exponent. All of them are momentum transfer and temperature dependent. This function has been successfully applied to pure polymers and blends (Cendoya et al., 1999; Doxastakis et al., 2000; Hoffmann et al., 2000; Arbe et al., 1999).

Each of these parameters has some physical significance. If the prefactor α is unity, it suggests that there are no dynamic processes occurring before the experimental window which are not represented by the same mathematical form as Eq. (2.47), or that

any such processes represent a small part of the overall decay. The characteristic relaxation time τ gives an average relaxation time which indicates how fast the motion is. The stretching exponent β describes the width of distribution of relaxations. Larger β suggests a narrower distribution. The deviation of β from unity represents the extent of dynamic heterogeneity in the system.

The characteristics of a relaxation process is manifested by the relaxation time τ as a function of temperature. For Arrhenius processes, the activation energy *Ea* can be obtained from,

$$\ln \tau = \ln \tau_0 + \frac{Ea}{RT} \tag{2.48}$$

where τ_0 is a constant. This equation has been widely used to describe the secondary processes at low temperatures (Arbe et al., 1996; Arrighi et al., 1995a; Bergman et al., 1998).

Chapter 3
Neutron Scattering Technique

3.1 Introduction

Neutron scattering has become a key technique for investigating the structure and dynamics of materials down to an atomic scale (Roe, 2000). The uniqueness of this method is based on the fact that the wavelengths and energies of thermal neutrons are of the same order of magnitude as interatomic distances and excitation energies, respectively, in condensed matter, and thus it plays an important role in probing the static and dynamic properties of materials.

3.2 Principles of neutron scattering technique

The scattering of a neutron is characterized by the transfer of momentum,

$$\hbar \mathrm{q} = \hbar(\mathrm{k}_f - \mathrm{k}_i) \tag{3.1}$$

and energy,

$$\begin{aligned} \Delta E = \hbar\omega &= E_f - E_i \\ &= \frac{\hbar}{2m}(k_f^2 - k_i^2) \end{aligned} \tag{3.2}$$

where $\hbar$ is Planck constant,

$$\hbar = \frac{h}{2\pi} \tag{3.3}$$

k_f and k_i are the scattered and incident wave vectors of the neutron, and E_f and E_i the energies of scattered and incident neutrons. Figure 3.1 illustrates an incident neutron with wave vector k_i and energy E_i, which is scattered by a scattering angle 2θ.

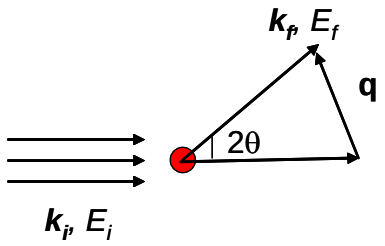

Fig. 3.1 A schematic of neutron scattering process.

For an inelastic scattering process, $\left|\mathrm{k}_f\right| \neq \left|\mathrm{k}_i\right|$. For a quasielastic scattering process,

$$\left|\mathrm{k}_f\right| \cong \left|\mathrm{k}_i\right| = \frac{2\pi}{\lambda_0} \tag{3.4}$$

where λ_0 is the wavelength of the incoming neutrons. The magnitude of the scattering vector q is

$$q \cong \left|\mathrm{q}\right| = \frac{4\pi}{\lambda_0}\sin\theta \tag{3.5}$$

Thus, q is resolved in neutron instruments as it is related to the scattering angle 2θ.

As discussed above, neutron scattering occurs at the nuclei. The interaction between them is characterized by the scattering length, which depends on both the particular isotope and the relative spin orientations of neutron and nuclei (Ewen and Richter, 1997; Bée, 1988; Trouw and Price, 1999). If all nuclei in the sample have the

same spin and isotope, the scattering is said to be coherent. A random distribution of scattering lengths or a random combination of spins, gives rise to incoherent scattering. Different isotopes of the same nucleus could give different scattering lengths. The incoherent and coherent scattering cross sections are given by

$$\sigma_{inc} = 4\pi(\langle b^2 \rangle - \langle b \rangle^2) \tag{3.6}$$

and

$$\sigma_{coh} = 4\pi \langle b \rangle^2 \tag{3.7}$$

where $\langle b^2 \rangle$ and $\langle b \rangle^2$ are the mean square length and the square of mean scattering length, respectively.

Table 3.1 lists the scattering lengths and cross sections for some common elements existing in polymer systems. As shown in this table, hydrogen and deuterium have a large difference in scattering cross sections. This allows selective labeling of hydrogen-containing organic material and thus plays a crucial role for studying polymer blend dynamics since one component can be hydrogenated and the scattering signal is dominated by incoherent scattering, while deuterium is suitable for structural studies.

The intensity of the scattered neutrons observed in experiments is represented by the double-differential cross section, which is defined as the probability that neutrons are scattered into a solid angle $d\Omega$ with an energy change $\Delta E = \hbar\omega$, (Lovesey, 1984; Bée, 1988)

$$\frac{\partial^2 \sigma}{\partial \Omega \partial \omega} = \frac{k_f}{4\pi k_i} \left[\sigma_{inc} S_{inc}(\mathrm{q}, \omega) + \sigma_{coh} S_{coh}(\mathrm{q}, \omega) \right] \tag{3.8}$$

where $S_{inc}(\mathrm{q},\omega)$ and $S_{coh}(\mathrm{q},\omega)$ are incoherent and coherent scattering laws, σ_{inc} and σ_{coh} are incoherent and coherent atomic cross sections.

Table 3.1 Scattering lengths (b) and cross sections (σ) for some common elements and isotopes

Elements	b_{coh} (10^{-15} m)	b_{inc} (10^{-15} m)	σ_{coh} (10^{-24} m^2)	σ_{inc} (10^{-24} m^2)
^{1}H	−3.7423	25.217	1.7599	79.91
^{2}H	6.674	4.033	5.597	2.04
C	6.6535	0	5.563	0
O	5.805	0	4.235	0

The incoherent and coherent dynamic scattering laws, which are measurable in neutron scattering experiments, are related to the simulation observables through the Fourier transform,

$$S_{inc}(\mathrm{q},\omega)=\frac{1}{2\pi}\int_{-\infty}^{+\infty}I_s(\mathrm{q},t)\exp(-i\omega t)dt \tag{3.9}$$

$$S_{coh}(\mathrm{q},\omega)=\frac{1}{2\pi}\int_{-\infty}^{+\infty}I_c(\mathrm{q},t)\exp(-i\omega t)dt \tag{3.10}$$

where $I_s(\mathrm{q},t)$ and $I_c(\mathrm{q},t)$ are the self and collective intermediate scattering functions defined in Section 2.8.3, which are related to the self-correlation and collective correlation, respectively.

3.3 Neutron techniques used in current work

As discussed above, neutron scattering has two components. The incoherent scattering is associated with self-correlation of individual atoms at time different times; while the coherent scattering arises from correlation between different atoms at the same or different times. They are measured by different techniques and different kinds of sample information are provided. The techniques used in this work are discussed below.

3.3.1 Diffraction

Diffraction spectrometer measures the single differential cross-section, which is the summation of the scattering intensity over all energy transfers (Trouw and Price, 1999),

$$\frac{\partial \sigma}{\partial \Omega} = \int_{-\infty}^{\infty} \frac{\partial^2 \sigma}{\partial \Omega \partial \omega} d\omega \tag{3.11}$$

Combining (3.8) and (3.11),

$$\frac{\partial \sigma}{\partial \Omega} = \sigma_{coh} S(q) + \sigma_{inc} \tag{3.12}$$

where $S(q)$ is the static structure factor, which as explained in Section 2.8.2.4, provides the structural information of investigated samples.

For the diffraction measurement performed in this work, we used the BT-7 triple-axis spectrometer at the NIST Center for Neutron Research in Gaithersburg, MD. The detailed configuration is discussed in Chapter 5.

3.3.2 Quasielastic neutron scattering (QENS)

Quasielastic neutron scattering is a special low-energy inelastic scattering technique. These techniques are suitable for the measurements of very small energy changes (such as the low energy window for polymer backbone motion) on time scales from 10^{-1} to 10^{4} ps. Backscattering and time-of-flight Spectrometry are the two commonly used quasielastic neutron techniques. The backscattering instrument sacrifices the wide energy window and focuses the neutron flux in a very narrow band of energies to achieve better resolution. This makes use of the fact that Bragg reflection at 180° from a single crystal yields an extremely sharp energy spectrum, around 1 μeV. Time-of-flight spectroscopy employs multiple choppers to produce a pulsed monochromatic beam at the sample position, and time-of-flight analysis of events in a large array of detectors to determine energy transfer and wave vector transfers q for neutrons scattered by the sample (Copley and Cook, 2003).

The QENS measurements in this work are performed on the high-flux backscattering (HFBS) and the disk chopper time-of-flight spectrometer (DCS) at the NIST Center for Neutron Research in Gaithersburg, MD. For detailed information refer to Chapter 6.

3.3.3 Neutron spin echo (NSE)

NSE is a useful technique to access relaxation processes on a molecular level (Bée, 1988; Higgins and Benoît, 1996). It is distinguished from all other dynamic neutron scattering techniques in that it measures the velocity change of incident and

scattered neutrons using the Larmor precession of the neutron spin in an external magnetic field. The incoming and outcoming velocity difference of every neutron can be measured directly because the neutron spin vector acts like the hand of an internal clock attached to each neutron that stores the velocity on the neutron itself. Thus, NSE spectroscopy decouples energy resolution from beam characteristics that it can achieve the highest energy resolution from all inelastic neutron scattering techniques with only 10-20% monochromatic beam. The NSE technique is a Fourier method and directly measures the normalized dynamic structure factor in the time domain:

$$\widetilde{S}(q,t) = \frac{S(q,t)}{S(q,0)} = \frac{\sum_{ij} b_i b_j \exp[i\mathrm{q}\cdot \mathrm{r}_{ij}(t)]}{\sum_{ij} b_i b_j \exp[i\mathrm{q}\cdot \mathrm{r}_{ij}(0)]} \tag{3.13}$$

where $\mathrm{r}_{ij} = \mathrm{r}_i - \mathrm{r}_j$, r_i and r_j indicate the position vectors of different scattering centers.

The NSE experiments were performed at the NSE spectrometer IN11C at the Institute Laue-Langevin (ILL) in Grenoble. Detailed information is shown in Chapter 4.

3.4 Data analysis

Neutron scattering experiments measure the scattering law *S(q,ΔE)* as a function of ΔE. In order to compare with simulation results, the frequency domain function *S(q,ΔE)* is transformed to the intermediate scattering function *S(q,t)*, which is in the time domain. This transform is achieved by applying the discrete complex Fourier integral to each set of data measured at a constant temperature and momentum transfer (Carlsson et al., 2001):

$$\widetilde{S}(q,t) = \sum_{k=1}^{N} \widetilde{S}(q,\omega_k)\exp(-i\omega_k t)\Delta\omega_k \tag{3.14}$$

where k represent a data point, N is the total number of data points, and ω_k is the angular frequency defined by

$$\omega_k = \frac{\Delta E}{\hbar} \tag{3.15}$$

$\Delta\omega_k$ is the frequency interval.

Since neutron scattering spectrometers offer a limited energy resolution, the measured $S(q,\omega)$ is affected by the instrumental resolution function $R(q,\omega)$. $R(q,\omega)$ is obtained when purely elastic ($\Delta E = 0$) scattering takes place in the sample. Normally it is determined from the scattering of a sample at a very low temperature, where all the dynamical processes are frozen. Thus, the experimentally accessed quantity has to be compared with the convolution of the resolution and then Fourier transformed to the time domain as indicated as following,

$$\widetilde{S}(q,\omega) = S(q,\omega) \otimes R(q,\omega) \tag{3.16}$$

$$\Downarrow$$

$$\widetilde{S}(q,t) = S(q,t) \otimes R(q,t) \tag{3.17}$$

In some cases, the normalized intermediate scattering function *S(q,t)* is fit with the KWW equation (Eq. (2.47)) to get the values of fitting parameters A, β and τ. The fitting is conducted using a self-written global optimization program, which is based on the simulated annealing technique. In the fitting, the deviation of the predicted fit from the measured values is calculated as a function of KWW parameters (A, β and τ). These parameters are accepted when the deviation reaches a very small number (say 10^{-7}). In

the fitting program the prefactor A and stretching exponent β are set to be in a range of 0 to 1, and no constraints are set on τ.

Error bars for the Fourier transformed data and KWW parameters are also calculated. This calculation is based on a sampling technique, which involves randomly generating a large number of data sets with each data point randomly placed within its error bars. In the calculation, the sample quantity was chosen to be 500, since as discussed by García Sakai et al. (2004), the size of the error bars did not change for 500 generations. The error bars presented in the figures of this thesis correspond to the minimum and maximum values of each parameter obtained in the 500 generations. Note that for the current study, the error bars for the Fourier transformed decay data are so small that they are approximately the size of the symbols and thus they are not indicated on the graphs.

Chapter 4
Collective Motion in Poly(ethylene oxide)/Poly(methyl methacrylate) Blends

This chapter presents neutron spin echo and structural measurements on a perdeuterated miscible polymer blend: poly(ethylene oxide) [PEO]/poly(methyl methacrylate)[PMMA], characterized by a large difference in component glass transition temperatures and minimal interactions. The measurements cover the spatial range 3.7 to 8 Å and the temperature range *Tg* - 75 to *Tg* + 89, where *Tg* is the blend glass transition. The spectra, obtained directly in the time domain, are very broad with stretching parameters $\beta < 0.20$. The relaxation times vary considerably over the spatial range considered. At small spatial scales, consistent with intramolecular correlations, relaxations are detectable by our measurements with relaxation times smaller than 1 μs even at temperatures far below *Tg*. The temperature dependence of these relaxation times strongly resembles the β-relaxation process observed in pure PMMA. At the largest spatial scales, consistent with the first structure factor peak in pure PMMA, the spectra may be consistent with the α-relaxation in PMMA, but have a weaker temperature dependence as a result of blending.

4.1 Introduction

As discussed in Chapter 1, motions in polymeric materials are typically associated with segmental α-relaxation or localized β-relaxation processes. Whole chain motions,

such as Rouse motion or reptation, also contribute to polymer dynamics, making the spectrum of dynamic processes in polymers very broad. Time-temperature superposition [tTs] is often used to extend the time scale of a polymer dynamics experiment by taking measurements at a series of temperatures. The premise of this principle is that lowering temperature has the same effect as extending to longer measurement times. tTs is often used with rheological data (Colby, 1989) but has also been applied to quasielastic neutron scattering data (Richter et al., 1998) using the shift factors obtained from rheology. The physical implication of shifting neutron data successfully with mechanical shift factors is that the processes probed by the two methods have the same temperature dependence, despite the fact that they probe very different time scales.

We investigate mixtures of poly(ethylene oxide) [PEO, *Tg* ~ 220 K] and poly(methyl methacrylate) [PMMA, *Tg* ~ 405 K]. A variety of techniques have been employed to study the dynamics of this blend. The two components retain their individual characters in the blend, as suggested by ^{2}H-NMR measurements (Lutz et al., 2003) and the failure of tTS in oscillatory shear measurements (Colby, 1989). Dielectric spectroscopy on blends with PEO contents up to 25 wt% shows that the merged $\alpha\beta$-relaxation process of PMMA becomes faster with addition of PEO, the low *Tg* component (Dionísio et al., 2000). This study also suggests that PEO motion is cooperative with the main chain of PMMA. In contrast, NMR on d_4PEO/PMMA blends with PEO contents of 3 – 30% has observed PEO motion that is up to 12 orders of magnitude faster than PMMA motion at the blend *Tg*, and depends only weakly on composition (Lutz et al., 2003), suggesting the motion of PEO is not coupled to that of PMMA. These authors ascribe their observations to the lack of side groups in PEO

allowing it to move freely on the segmental level, despite being surrounded by nearly immobile PMMA chains. Another explanation is provided by Kumar et al. (1996). Concentration fluctuations [which should be high in this blend due to its small χ parameter] temporarily create regions rich in PEO, which allow a large fraction of the PEO to relax unhindered by PMMA. Another fraction of the PEO would be expected to relax more slowly, consistent with the mean blend composition, leading to a bimodal distribution of relaxation times, as is sometimes observed for the low *Tg* component in miscible blends.

The dynamic behavior of both pure components has also been investigated. Results from broad-band dielectric spectroscopy are able to discern both the α- and β-relaxations of pure PMMA around *Tg* (Gómez et al., 2001; Bergman et al., 1998). Near *Tg* the α-relaxation time changes very rapidly with temperature and the β-relaxation time follows an Arrhenius temperature dependence with an activation energy of *Ea* = 79.4 kJ/mol. The β-relaxation of pure PMMA has been attributed to hindered rotation of the carboxyl side group around the bond that links it to the main chain (Bergman et al., 1998). Pure PEO has been investigated using quasi-elastic neutron scattering. However, because mobility quickly increases above the melting temperature of PEO, which occurs near *Tg* + 120 K (Mos et al., 2000; Mao et al., 2000), there are only a narrow range of temperatures with motion which falls within the time [energy transfer] range of the spectrometers.

As mentioned above, NMR has shown that PEO in the PEO/PMMA blend relaxes essentially as though it were in an environment of nearly pure PEO (Lutz et al., 2003).

Two characteristics of this blend are that it has very large *Tg* contrast, and that the Flory interaction parameter is very small. In light of this, the expectation of the Kumar theory (Kumar et al., 1996) is quite similar to the observations, although there are other possible interpretations (Lutz et al., 2003). A connection between the observed dynamics and molecular level processes would help to clarify the situation. In order to provide this interpretation, we have initiated an investigation of this system using quasi-elastic neutron scattering. Quasi-elastic neutron scattering provides temporal and spatial information by following both the energy [time] and momentum [spatial] changes in neutrons interacting with the sample. Two types of experiments are possible: incoherent, which measures self-motion, and coherent, which measures the decay of correlations between two different scattering groups [relative motion]. The current work presents results of the latter type obtained from neutron spin-echo (NSE) measurements.

The NSE technique has been applied to several single component polymers: polybutadiene (PB) (Arbe et al., 1996; Richter et al., 1998b), polyisobutylene (PI) (Arbe et al, 1997; Richter et al., 1998a and 1998b) and polypropylene (PP) (Arrighi et al., 2001). One study (Hoffmann et al., 2000) has investigated polymer blend dynamics in the PI/poly(vinyl ethylene) (PVE) system well above *Tg*. Both single component and blend studies show significant spatial effects. Relaxation times for polybutadiene at the first (interchain) and second (intrachain) peaks in the static structure factor show temperature dependences that can be associated with the α- and β-processes, respectively. This is further evidenced by the success of tTS (using shift factors from mechanical data) at the interchain peak, and failure at the intramolecular peak. These results support the idea that at the interchain peak, NSE probes the high frequency tail of the α-process, while some

other process is observed at the intrachain peak. In the PI/PVE blend, it is shown that at temperatures far above the blend *Tg*, the component relaxation times coincide at length scales greater than 31 Å, and differ at length scales of 14 Å and less (Hoffmann et al., 2000).

The PEO/PMMA blends in the current study have 20 and 30 wt% PEO and are investigated from 273 – 414 K [below and above the blend *Tg*] and in the spatial range 3.7 – 8 Å. The spatial range covers the structure factor peaks of both PEO and PMMA, and is in the region where distinct component mobilities are observed (Hoffmann et al., 2000). Our results depend strongly on the spatial range of the measurement. At separations small enough that intermolecular contacts are not possible, relaxation times exhibit an Arrhenius temperature dependence with activation energies consistent with the β mode of PMMA. The NSE spectra in this intramolecular region also scale with PMMA composition. Although the fraction of motion that decays on timescales faster than the instrument increases for higher PEO content, the decay within the time window of NSE is insensitive to composition.

4.2 Experimental section

4.2.1 Materials and sample preparation

Perdeuterated PEO/PMMA blends and perdeuterated pure PMMA were used for the experiments. Both components were prepared by anionic polymerization and thus have narrow molecular weight distributions. The dPEO was obtained from Polymer Laboratories. dPMMA was prepared as follows. The deuterated MMA (Aldrich) was

distilled under reduced pressure from both calcium hydride and triethylaluminum to ensure complete removal of protic impurities. The purified monomer was added to a reactor containing THF at –78 ºC and diphenylhexyllithium as an initiator. The monomer was added drop-wise to minimize exotherms which would lead to premature termination. The polymerization was allowed to proceed for 20 minutes at –78 ºC after complete addition of the MMA monomer. The polymerization was terminated with the addition of acidic methanol. The THF solution (approximately 10% polymer by weight) was precipitated in excess petroleum ether and upon filtration, the sample was dried for 18 hours at 60 ºC under reduced pressure. The white fibrous product was obtained in greater than 95% isolated yield.

The molecular weights, deuterium level, polydispersity indices, and glass transition temperatures for both components are given in Table 4.1. Deuterium levels were assessed with proton NMR, and differential scanning calorimetry with heating and cooling rates of 10 K/min was used to measure the glass transition temperatures. The *Tg* for the 20 wt% blend is 348 K, and for the 30 wt% blend, the *Tg* is 326 K. Polydispersity was assessed using size exclusion chromatography. The blend samples were prepared using the following procedure. The required amounts of PEO and PMMA were calculated and each component was dissolved separately in acetone at 313 K with constant stirring using a magnetic stirrer for 8 hours. Once both polymers had dissolved completely in the solvent, the solutions were mixed and the mixture was stirred for an hour. This solution was then transferred to a round-bottomed flask and dried in a rotary evaporator at 313 K. The resulting mixture was further dried in a vacuum oven at 423 K for 3 days to remove any residual solvent. The sample was rapidly transferred to a hot

press maintained at 410 K and hot pressed for 4 hours. Once the sample had been pressed, the entire hot press assembly was quenched in liquid nitrogen to prevent crystallization. The resulting samples were transparent, indicating miscibility.

Table 4.1 Properties of samples.

Polymers	Mw	Deuterium level	*Tg* (K)	polydispersity
dPEO	550 000	99.89%	221	< 1.1
dPMMA	375 000	99.54%	402	< 1.2

4.2.2 Methods

NSE measures the velocity change of incident and scattered neutrons using the Larmor precession of the neutron spin in an external magnetic field. After aligning the spins, neutrons are passed through a magnetic field where each spin processes by a given amount. The neutrons interact with the sample, and the spins are then flipped by 180º. The neutrons then pass through another magnetic field identical to the first. If there are only elastic collisions that do not involve any exchange of energy with the sample [i.e. no motion] then the second field "undoes" the action of the first so that the spins are once again aligned. Any deviation from this can thus be attributed to motion in the sample. The observable in the NSE technique is the normalized dynamic structure factor in the time domain [Eq. (3.13)].

The NSE experiments were performed at the NSE spectrometer IN11C (Farago, 1997) at the Institute Laue-Langevin (ILL) in Grenoble. The wavelength of the incoming neutrons was λ = 5.76 Å with $\Delta\lambda/\lambda$ = 15% full width half maximum (FWHM). The instrumental resolution was measured on amorphous quartz with a similar shape and size as the sample as well as on the samples themselves by cooling them down to 10 K where all relaxations can be safely supposed to frozen out. Data was taken with the double echo configuration between Fourier times of 0.008 and 1.48 ns with roughly equidistant steps on a logarithmic scale. The 30% PEO/PMMA blend was studied at six temperatures: T = 273, 313, 362, 382, 393 and 413 K. The IN11 is equipped with a multidetector bank covering a 30º scattering angle in one position. Combining three detector positions allowed gathering of data over a q range of 0.35 to 1.66 $Å^{-1}$. At each position the 40 detectors were binned into seven groups each covering about a 4.3 degree scattering angle. The 20% PEO/PMMA blend was studied at six temperatures T = 273, 313, 353, 373, 393 and 412 K, but only one configuration resulting in a q range from 1.35 to 1.70 $Å^{-1}$. These were also binned into the five upper wavevectors described above. Pure PMMA was measured at T = 393 and 413 K again at one spectrometer configuration for a wavevector range of $1.35 \leq q \leq 1.70$ $Å^{-1}$.

The static structure factor *S(q)* for both blends and pure PMMA were measured on the D20 diffractometer at the ILL at room temperature. Since there are few protons present in the samples, the scattering intensity from both structural and dynamic experiments is dominated by coherent scattering. In the static structure factor, this reveals preferred packing distances, and in NSE spectra collective motion between different scattering centers is observed. The weighting factors in Eq. (3.13) are thus the

coherent scattering cross sections of oxygen, deuterium and carbon atoms. Because the coherent cross sections for deuterium (6.671 fm) and carbon (6.646 fm) are nearly identical, there are effectively two scatterers in the system: deuterium/carbon and oxygen (5.803 fm). As an approximate tool to interpret our results, we have grouped these atoms together in three units: the PMMA backbone [a], the PMMA side chain [b] and the PEO repeat unit [c], as illustrated in Fig. 4.1. At wavevectors corresponding to spatial scales larger than the average size of these units [~2.5 Å], the scattering may be regarded as arising from sums of atoms comprising each unit. Differences in unit size are taken into account by summing the scattering lengths of the individual atoms and normalizing for the volume occupied by each center. Values for these scattering length densities, $\langle \underline{b}_i \rangle$ are given in Table 4.2 for each scattering center in our system. The neutron weighting for each pair, $\langle \underline{b}_i \rangle \langle \underline{b}_j \rangle$ is presented in Table 4.3.

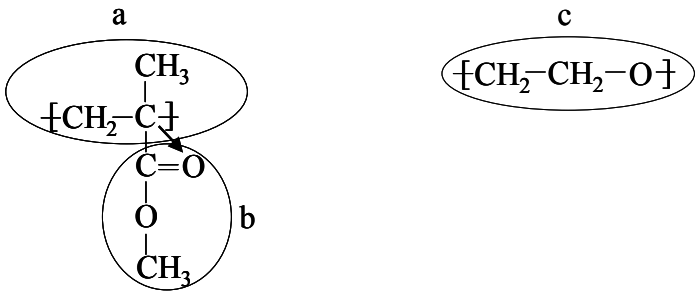

Fig. 4.1 Structures of PMMA and PEO.

Table 4.2 Coherent scattering length densities for scattering centers of PEO and PMMA.

Scattering center	a	b	c
Coherent Scattering Length Density (10^{-6} Å^{-2})	8.007	5.013	6.481

Table 4.3 Neutron weights for scattering centers of PMMA and PEO.

pair	Weight (10^{-12} Å^{-4})
a/a	64.11
a/c	51.89
c/c	42.00
a/b	40.13
b/c	32.49
b/b	25.11

4.3 Results

4.3.1 Structure

Shown in Fig. 4.2 is the coherent static structure factor *S(q)* for perdeuterated pure PMMA and perdeuterated 10%, 20% and 30% dPEO/dPMMA blends. Although the intensity varies with sample due to differences in thickness, atom counts and neutron flux in each experiment, we have aligned the data such that the intramolecular peaks at 3.0 Å^{-1} overlap. These length scales [r < 2.5 Å] correspond to bond length and angle distances, both of which are not expected to vary significantly due to differences in composition. Three spatial regimes are indicated in the Figure. The upper and lower limits refer to the wavevector extremes of our NSE data. The significance of these regions will become apparent when the dynamic data are discussed. Pure dPMMA is characterized by a first peak at q = 0.9 Å^{-1}, a second broad peak at q = 2.0 Å^{-1}, and 3.0 Å^{-1} mentioned above.

The locations of these peaks are consistent with the coherent static structure factor of partially deuterated PMMA observed by Moreno et al. (2001a) using neutron scattering. Three pairs are present in pure PMMA: a/a, a/b and b/b. The most likely origin of the first peak [q = 0.9 Å^{-1}] is intermolecular a/a pairs. Supporting this hypothesis is the data of Moreno et al. (2001a) taken for PMMA with all hydrogens except those of the -$COOCH_3$ group substituted with deuterium. In this case, the intensity of the 0.9 Å^{-1} peak is approximately four times greater than the q = 2.0 Å^{-1} peak, while for the present data the ratio is ~ 1.2. Substituting the b unit with hydrogen rather than deuterium, as in the present case, would decrease the scattering length density of unit b substantially, because the coherent scattering length for hydrogen is negative. This would result in a decrease in intensity for a/b and b/b contributions. The lower intensity of the area between 1.1 and the 2.0 Å^{-1} peak, should be interpreted as the location of a/b and b/b correlations. It is certainly reasonable that side group/backbone [a/b] and side group/side group [b/b] correlations would appear at length scales smaller than the backbone/backbone [a/a] correlations. The size of the side group in PMMA results in intermolecular backbone/backbone packing on a length scale of about $2\pi/q$ = 7 Å, considerably larger than the intermolecular chain packing peak in pure PEO, which occurs at ~ 4.2 Å [q = 1.4 Å^{-1}], as assessed by neutron diffraction (Johnson et al., 1998), and molecular dynamics simulation (de Leeuw et al., 2001). The second broad peak at q = 2.0 Å^{-1} is consistent with intramolecular packing of a and b units, i.e. a PMMA backbone segment and the side group with which it is bonded. The fact that it is broader than the first peak indicates a distribution of atomic pair distances within the two groups, and also that the side group samples a number of different configurations with respect to the chain backbone.

Rotation of the -$COOCH_3$ side group around the C-C bond linking the side group to the main chain has been identified as the origin of the β-relaxation in pure PMMA (Schmidt-Rohr et al, 1994), and thus such a sampling is expected even below *Tg*. The final peak at 3.0 $Å^{-1}$ occurs at spatial scales too small [~2.1 Å] to interpret in terms of a and b units.

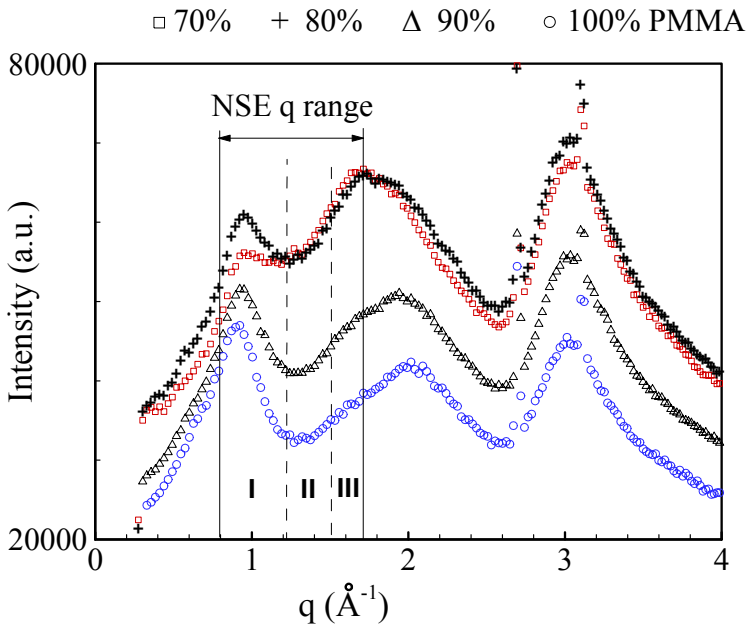

Fig. 4.2 Static structure factor of perdeuterated pure PMMA and 10%, 20% and 30% dPEO/ dPMMA blends.

We now consider the effect on packing when PEO is added to pure PMMA. The peak at 3.0 $Å^{-1}$ does not change its shape or location with PEO content, as is consistent with a specific intramolecular atom pair separated by at most two bonds. The high wavevector side of the peak at 0.9 $Å^{-1}$ builds slowly as PEO is added, indicating an additional packing process at smaller length scales than PMMA chain packing. This is consistent with packing of a and c units, as PEO chains should be able to pack better with the PMMA chain backbone than other PMMA chains. There is likely some contribution

from PEO self-packing [c/c] here as well, as the peak in the structure factor of pure PEO is centered at 1.4 $Å^{-1}$. The peak at q = 2.0 $Å^{-1}$ narrows and shifts to smaller wavevectors with PEO addition. This indicates that the PMMA side group samples fewer conformations as PEO is added, and that the conformations sampled tend to keep the oxygen atoms in the side group further from the PMMA backbone than when PEO is not present. This behavior seems to saturate when the PEO content is between 20 and 30%. It is unlikely that these features arise from PEO self-packing, because the length scales are smaller than the peak in the pure PEO structure factor, and because the intensity does not build with PEO content between 20 and 30%.

4.3.2 Dynamics

Examples of NSE spectra at different wavevectors for 20% and 30% blends are presented in Fig. 4.3. Representative wavevectors from each region are shown for both blends, with the exception of region I for the 20% blend, where no data were taken. The curves in the figure are Kohlrausch-Williams-Watts (KWW) or stretched exponential fits [Eq. (2.47)]. The relaxation processes we observe are very stretched at all momentum transfers, with $\beta \sim 0.15$.

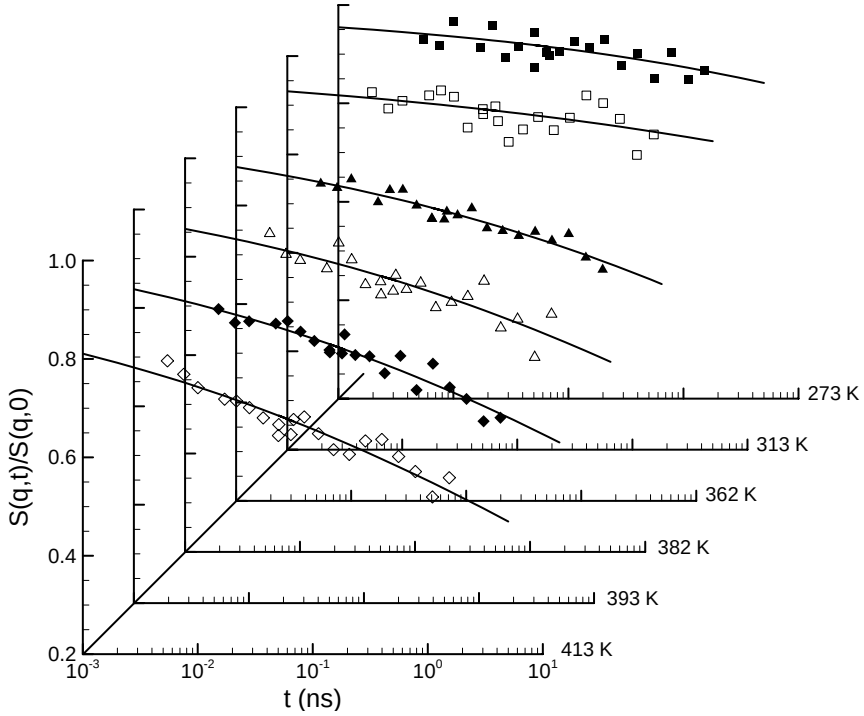
S(q,t)/S(q,0)
1.0
0.8
0.6
0.4
0.2
10^{-3}
10^{-2}
10^{-1}
10^{0}
10^{1}
t (ns)
273 K
313 K
362 K
382 K
393 K
413 K

(a)

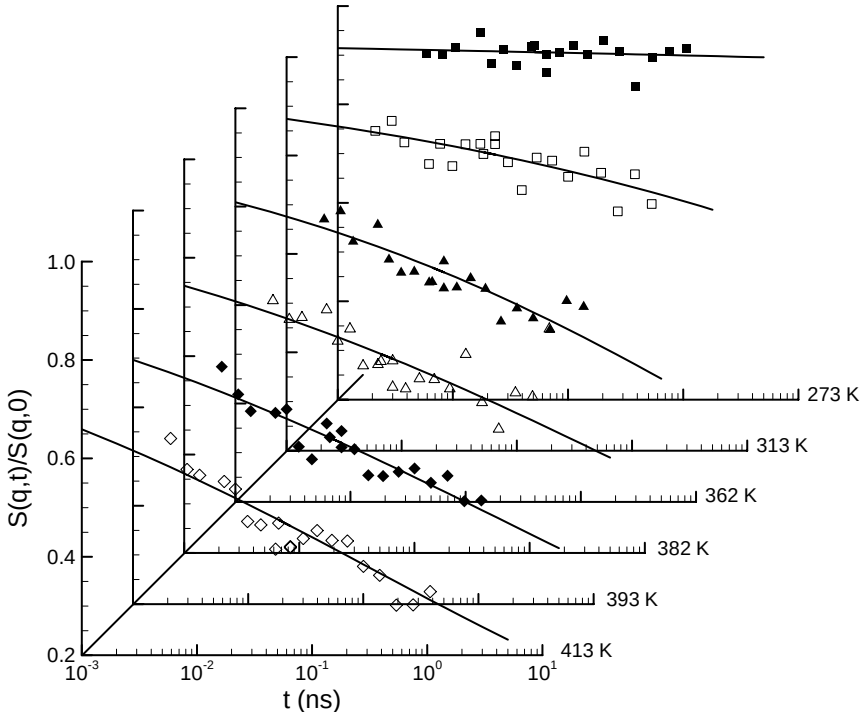
S(q,t)/S(q,0)
1.0
0.8
0.6
0.4
0.2
10^{-3}
10^{-2}
10^{-1}
10^{0}
10^{1}
t (ns)
273 K
313 K
362 K
382 K
393 K
413 K

(b)

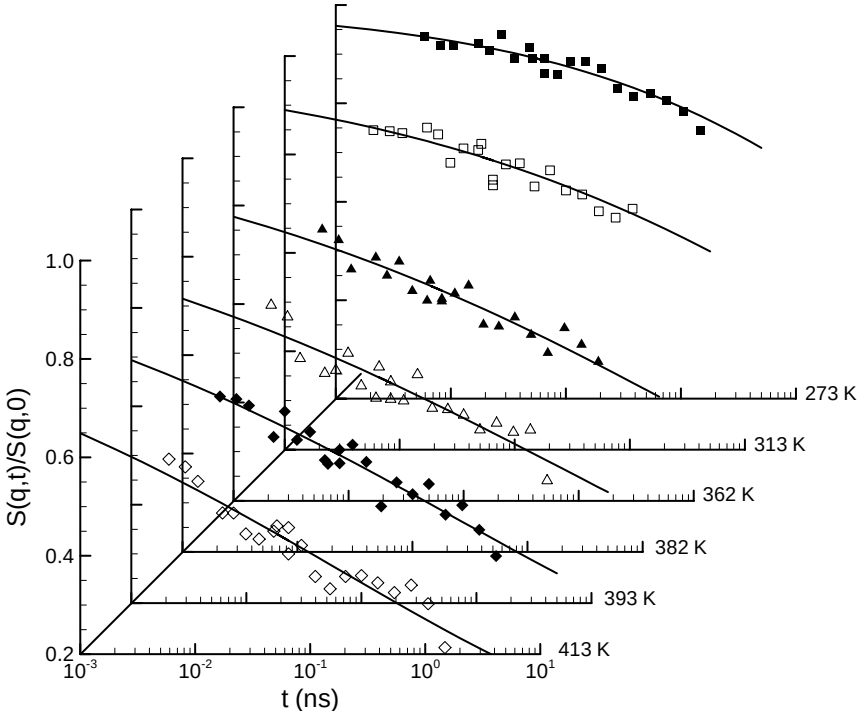
S(q,t)/S(q,0)
1.0
0.8
0.6
0.4
0.2
273 K
313 K
362 K
382 K
393 K
413 K
10-3
10-2
10-1
100
101
t (ns)

(c)

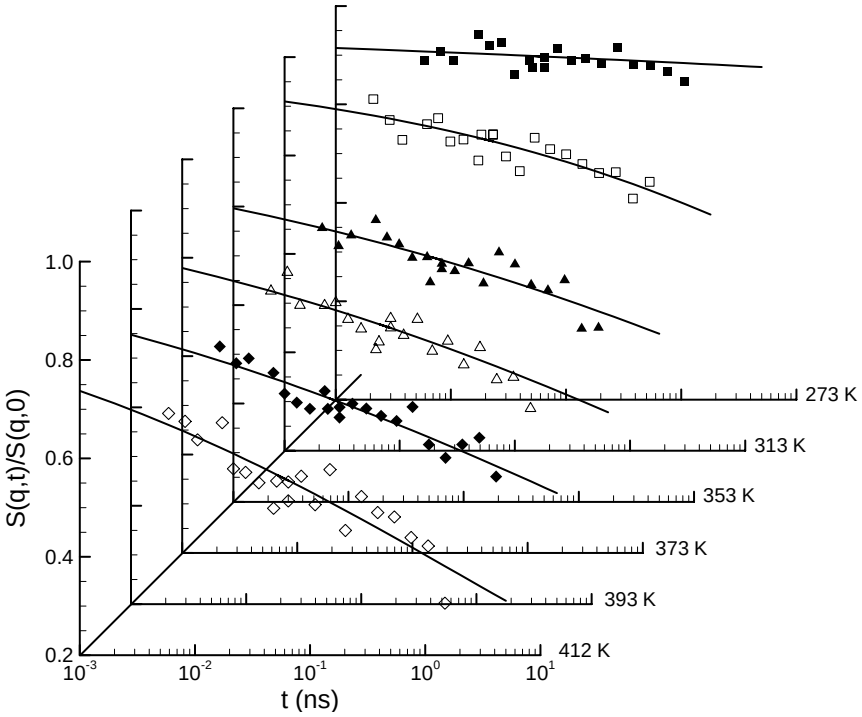
S(q,t)/S(q,0)
1.0
0.8
0.6
0.4
0.2
273 K
313 K
353 K
373 K
393 K
412 K
10-3
10-2
10-1
100
101
t (ns)

(d)

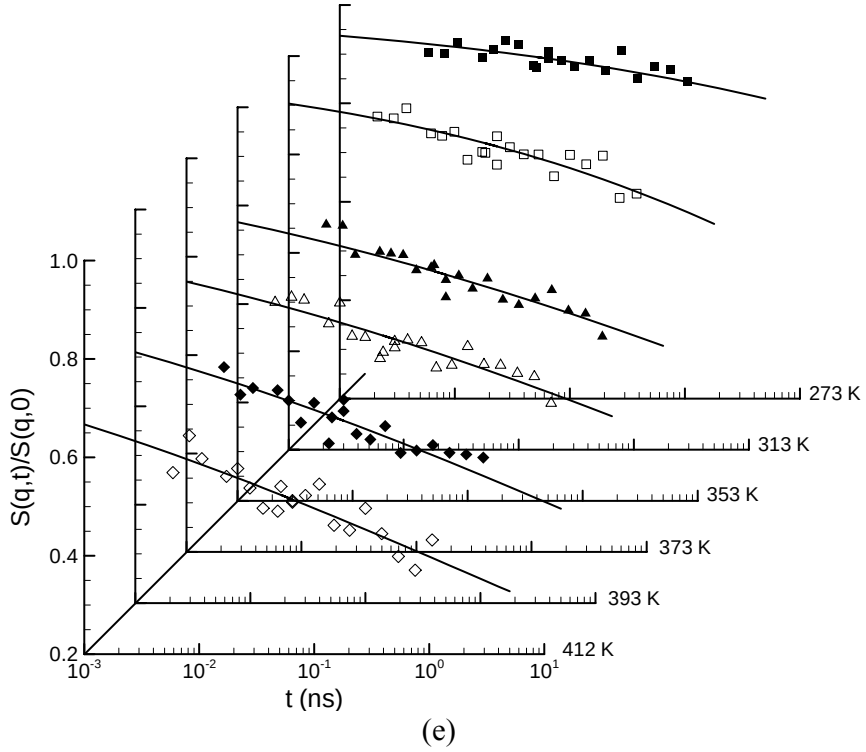

(e)

Fig. 4.3 NSE spectra for the temperatures indicated at (a) q = 1.05 Å^{-1} for 30% blend, (b) q = 1.41 Å^{-1} for 30% blend, (c) q = 1.66 Å^{-1} for 30% blend, (d) q = 1.41 Å^{-1} for 20% blend, (e) q = 1.66 Å^{-1} for 20% blend.

Our methodology in fitting the data to Eq. (2.47) is to first superpose the spectra, obtaining a more complete decay curve from which to determine the stretching parameter, as the assignment of β from a small decay is uncertain. Often this might be avoided by using stretching parameters obtained from dielectric or other data with larger time windows. Such data are not currently available for this system. The superposition is performed by defining a shift factor:

$$a_T = \frac{\tau(T)}{\tau(T_0)} \tag{4.1}$$

that empirically connects the data sets in a smooth curve, if possible. Here $\tau(T)$ and $\tau(T_0)$ are the relaxation times at temperature T and a reference temperature T_0. In contrast to the treatment of pure polymers (Ritchter et al., 1998), we are not able to use shift factors from mechanical measurements because mechanical data do not superpose for this blend. Terminal relaxation times are available for each of the blend components, however because of the nature of the NSE experiment we are not yet sure which component is being observed. The temperature dependence of terminal relaxation times of each component will be compared to the temperature dependence of NSE relaxation times below. In the fits performed to assign relaxation times used to define the shift factors, we take the prefactor as unity, and obtain β and τ as fit parameters. Using 273 K as the reference temperature, we determine shift factors for each momentum transfer, q, requiring that the same shift factor be used for all momentum transfers.

To assign relaxation times at individual temperatures, we fix β at the value obtained from the superposed spectra, and α and τ are obtained as parameters. In this case, the prefactor obtained is 0.95 or greater. The characteristic relaxation time τ_{KWW}, sets the timescale of the observed relaxations, and is the main parameter of interest. All relaxation times we report at individual temperatures are the result of this fitting procedure. At momentum transfers where the low temperature data show no decay, making time-temperature superposition difficult, we use representative values of the stretching parameters found from the superposed spectra at other momentum transfers: β = 0.15 for the 30% blend and β = 0.12 for the 20% blend. As can be seen from Table 4.4, the stretching parameters are relatively insensitive to spatial scale. It is important to note

Table 4.4 Relaxation times and stretching parameters obtained from tTS fitting. The reference temperature is *To* = 273 K.

		30% PEO / 70% PMMA		20% PEO / 80% PMMA	
	q (Å)	τ (ns)	β	τ (ns)	β
Region I	0.86	8.0×10^4	0.15		
	0.92	1.2×10^6	0.14		
	0.99	4.0×10^8	0.17		
	1.05	6.6×10^4	0.15		
	1.11	2.0×10^7	0.15		
	1.18	3.4×10^8	0.14		
Region II	1.24	7.8×10^9	0.16		
	1.29	2.2×10^{10}	0.13		
	1.35	7.8×10^{12}	0.15	---	---
	1.41	1.2×10^{14}	0.14	---	---
	1.46	7.8×10^{11}	0.14	---	---
Region III	1.51	2.1×10^5	0.16	4.65×10^7	0.11
	1.56	3430	0.15	7.07×10^5	0.12
	1.61	3250	0.15	2.58×10^7	0.12
	1.66	7943	0.15	2.64×10^6	0.11
	1.70	407	0.14	3.6×10^5	0.11

that in both fitting procedures for individual temperatures [α fixed at unity or β fixed at the superposed value], there is a range of stretching parameters from $\beta \sim 0.10$ to 0.30 that can successfully describe the data. This is a difficulty associated with the small time window and the very broad nature of the relaxations, which makes it impossible to get a

large decay in the spectra for this system using neutron spin echo. We report those values of β that result in the smallest error, and note that fits with other values of β are also possible.

Many of our relaxation times at low temperatures are too large [relative to the time window of the experiment] to be relevant, and are not reported. To place an upper limit on the relaxation times that can be extracted without significant error from the data, we require that the spectra have decayed at least 20% from its initial value. Because the spectra in this system are very broad [see below], this sets an upper limit of $\tau_{KWW} \sim 10^4$ ns on the range of relaxation times that we can report as numerical values. Spectra that have not decayed by at least 20% may be interpreted as having relaxation times larger than this limit, but the relaxation time cannot be estimated.

Time-temperature-shifted NSE spectra, calculated using the shift factors a_T are shown in Fig. 4.4 for selected momentum transfers, q. The figure shows representative time-temperature-shifted spectra at q = 1.41 Å^{-1} and 1.66 Å^{-1} for the 20% blend and q = 1.05 Å^{-1}, 1.41 Å^{-1} and 1.66 Å^{-1} for the 30% blend. Time-temperature superposition is reasonable at all momentum transfers, although the quality declines when q is less than 1.24 Å^{-1} or greater than 1.46 Å^{-1}. As illustrated in Fig. 4.4 (a), (c) and (e), the data are scattered around a single master curve close to the first (q = 1.05 Å^{-1}) and second (q = 1.66 Å^{-1}) peaks in the static structure factor of pure PMMA at both blend compositions. This corresponds to regions I and III described earlier [see Fig. 4.2]. In the intermediate q range [region II], the spectra for temperatures below the blend *Tg* decay very little. When the data are shifted with the same shift factor used in regions I and III, as is

illustrated for q = 1.41 Å^{-1} in Fig. 4.4 (b) and (d), this results in a larger scatter of the data around the superposed fit line below *Tg*. Oscillatory shear measurements (Colby, 1989) on this blend find a failure of time-temperature superposition, and thus it might appear the present results are inconsistent with those results. It is important to keep in mind that the current experiments probe two decades in time, whereas oscillatory shear measurements probe five decades in time, and thus is a far more stringent test of time-temperature superposition. The two time windows are also separated by seven decades.

The relaxation times and stretching parameters obtained from the superposed fits are shown in Table 4.4. The stretching parameters obtained from this procedure range from $\beta = 0.11$ to $\beta = 0.17$. Similar values are found in fits to assign the shift factors where the prefactor is fixed and β is a free parameter. These parameters correspond to spectra at a temperature T_o = 273 K taken out to 10,000 ns. All the superposed spectra have decayed to 0.5 or less, and thus if we accept the validity of time-temperature superposition, we can take with reasonable confidence these relaxation times that far exceed the timescale of the NSE technique. At the same time, caution should be used in interpreting the superposed spectra in this way, because in so doing we assume that the temperature dependence is unaltered as *Tg* is crossed. From the Table, some trends are evident. The relaxation time distribution in the 20% blend is broader than in the 30% blend, as expected based on the model reported by Kumar et al. (1996). Relaxations at wavevectors in regions I and II become very large. Although this trend is intriguing, the superposed relaxation times depend on the validity of tTs. The stretching parameters given in Table 4.4 were used in fitting the spectra at each temperature as described above.

Relaxation times reported in the remainder of the manuscript are the result of this fitting procedure.

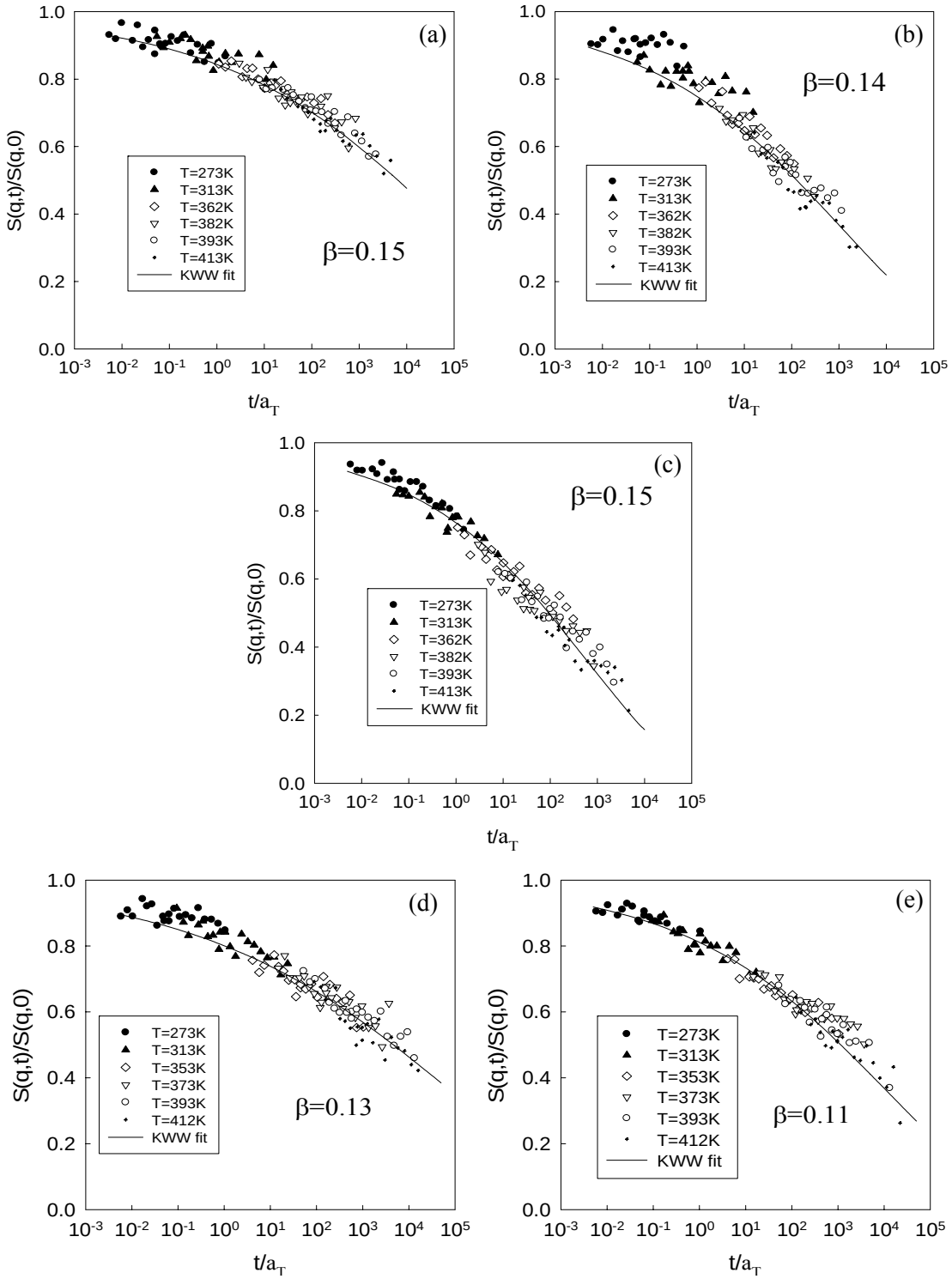

Fig. 4.4 Rescaled data with the calculated shift factor α_T at (a) q = 1.05 Å^{-1} for 30% blend, (b) q = 1.41 Å^{-1} for 30% blend, (c) q = 1.66 Å^{-1} for 30% blend, (d) q = 1.41 Å^{-1} for 20% blend, (e) q = 1.66 Å^{-1} for 20% blend.

4.3.3 Comparison of results with pure component data

Of interest when considering miscible blend dynamics is the difference of each component from its pure state. As explained above, this difference is particularly relevant when considered at constant T - Tg. Although incoherent neutron scattering techniques can reveal the motion of each component by selective deuterium labeling, in the present system, coherent scattering is measured on perdeuterated polymers. Thus it is not clear which blend component's motion is followed. An additional complicating factor is the measurement of scattering center motion relative to the position of other scattering centers, rather than itself. To orient ourselves, we compare relaxation times obtained from our NSE measurements to those obtained from each pure component. By considering the spatial scale at which the current results follow available measurements, we may be able to suggest which motion is dominant as spatial scale is varied. The best scenario is a comparison with incoherent neutron scattering techniques, for example from backscattering or time-of-flight spectrometers. Such data are not yet available for the blend or for PMMA. For PEO, some data are available, only above the melting temperature for PEO, which unfortunately is far above its Tg. In place of these measurements, we compare to dielectric measurements, which are available for both components. Shown in Fig. 4.5 are the relaxation times obtained from fits to individual spectra using the stretching parameters from the superposed data. Selected momentum

transfers from each region are shown as a function of distance above *Tg* for the 30% blend. Also shown are PMMA and PEO relaxation times from dielectric spectroscopy and neutron scattering data for PEO, which as explained above is only available at *Tg* + 127. The dielectric results are for the merged α/β- and β- relaxations for PMMA (Bergman et al., 1998), and are on semicrystalline PEO (Jin et al., 2002).

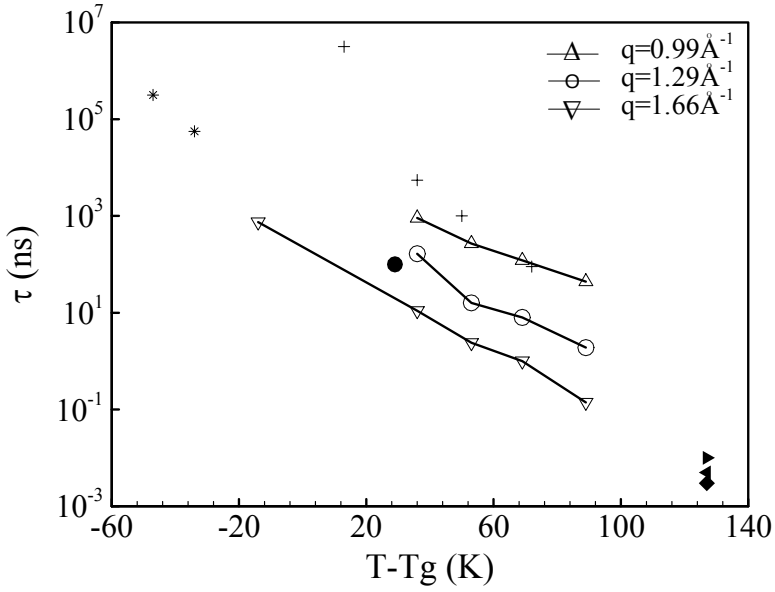

Fig. 4.5 Comparison of relaxation times [ns] of 30% blend from NSE with pure PEO and PMMA. QENS data for PEO at q = 0.99 Å^{-1} (►), 1.29 Å^{-1} (◄) and 1.66 Å^{-1} (♦) are from Mao et al. (2000); dielectric data for PEO are from Jin et al. (2002) and dielectric data for PMMA α- (+) and β- (∗) relaxtions are from Bergman et al. (1998)

The relaxation time of pure PEO appears to fit with the current measurements in region II, where the pure PEO structure factor peak is located. However, caution must be used when comparing the current measurements where PEO is fully amorphous, to semi-crystalline PEO. The neutron data (Mao et al., 2000) for PEO appear to fall along the

region III curve, although it is difficult to draw any conclusions because the higher temperature of these measurements requires sizeable temperature extrapolation of our results. In addition, the possibility of bimodal relaxation of PEO and the NSE timescale would suggest we observe the slow portion of the relaxation, not that of a region rich in PEO. The merged α/β data from pure PMMA are consistent with our NSE data at q = 0.99 $Å^{-1}$ [region I], the momentum transfer where the interchain peak in PMMA appears. In contrast, the β data from pure PMMA are consistent with region III. This rough overview suggests that the PMMA structural relaxation is observed in region I, the PMMA beta relaxation is observed in region III and that region II may highlight the PEO structural relaxation.

Pure PMMA stretching parameters for both the α- and β-relaxations have been reported from dielectric spectroscopy (Bergman et al., 1998). Values range from 0.2 at *Tg* to a high temperature limit of 0.55 for the α-relaxation, and from a low temperature plateau of 0.2 to 0.36 near the merging with the α-process for the β-relaxation. Our β values [0.11 – 0.17] are smaller than these results, and indicate that the addition of PEO broadens the distribution of relaxation times in the blend. This type of broadening often occurs in miscible blends (Zetsche and Fischer, 1994; Katana et al., 1995), and is expected by theory (Kumar et al., 1996). It is also possible that these measurements probe the combined motion of both blend components, which would also broaden the observed relaxations. The high temperature limit of the stretching parameter for pure PEO is 0.58 (Mos et al., 2000), and again our results are far broader than those of pure PEO.

4.3.4 Interpretation of Results

We divide the dynamic behavior of PEO/PMMA blends into the same three regions as the structural data: region I: q = 0.86 Å^{-1} to 1.23 Å^{-1}, region II: 1.23 Å^{-1} to 1.46 Å^{-1} and region III: 1.46 Å^{-1} to 1.70 Å^{-1}. There exist three relaxations previously identified in the pure components: the α- and β-relaxations of PMMA, and the α-relaxation of PEO. For each region, we seek to identify which, if any of these relaxations are observed. Differences between regions are evident in Fig. 4.6, where the relaxation times are plotted as a function of momentum transfer, q, for each temperature. The q dependence is relatively flat in region III. Region II and part of region I are characterized by a strong q dependence, which appears to flatten at the highest momentum transfers measured, just beyond the first peak in *S(q)* for pure PMMA. The largest relaxation time that we feel it is possible to assign based on sufficient decay [> 0.2] of the spectra is of the order 10^4. Most of the data points at the two lowest temperatures do not meet this criterion. The exception is data in Region III, which have measurable relaxation times below *Tg*. The data in region III must thus have a temperature dependence different than that in regions I and II, otherwise those regions would also have relaxation times detectable by NSE below *Tg*.

In region II and most of region I, the relaxation time is a power law in q at high temperatures, as shown in Fig. 4.7. The slope is consistent with $-2/\beta$, which is the stretched exponential form of the Gaussian approximation (Richter et al., 1998). The exceptions occur at the low end of the momentum transfer range. At the lowest momentum transfer measured, the relaxation times are well below the $-2/\beta$ scaling line

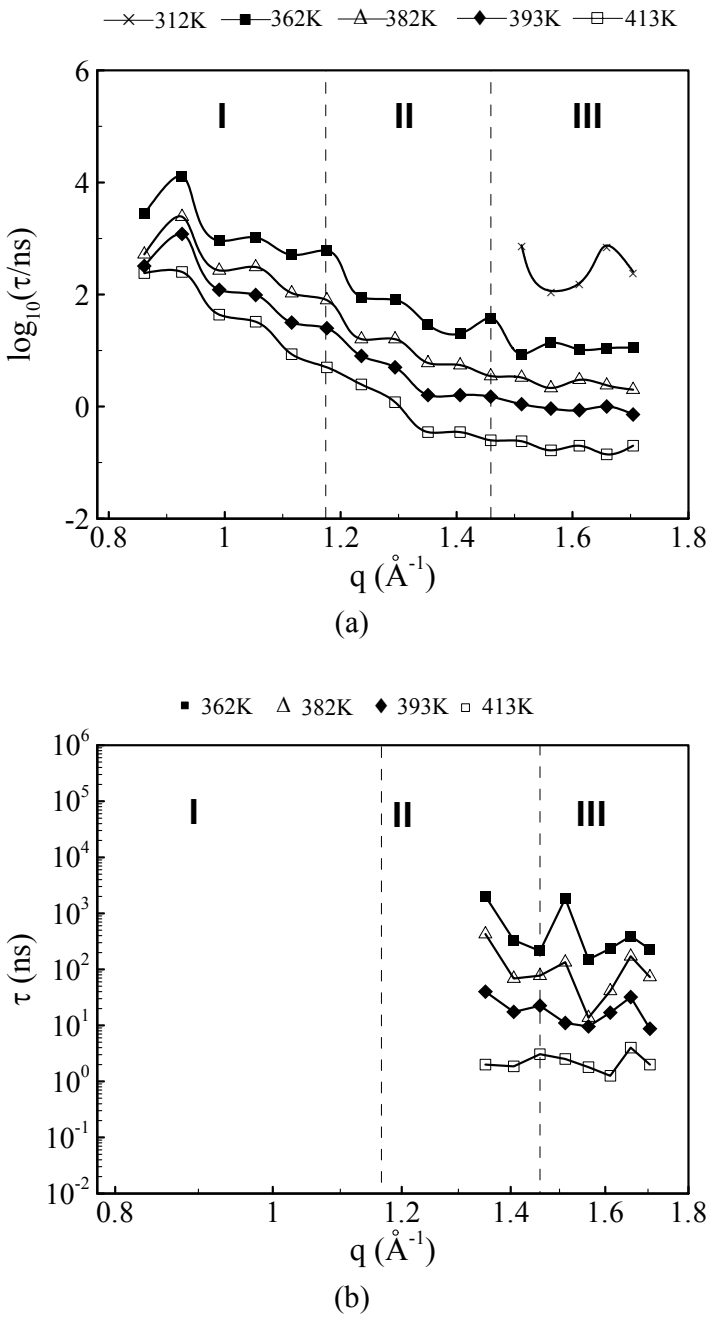

Fig. 4.6 Relaxation times as a function of wavevector at all the temperatures for: (a) 30% blend, (b) 20% blend.

for all temperatures. It is possible that a cross over in scaling occurs here, although this possibility cannot be tested without further data at lower momentum transfers. Near first peak in *S(q)*, [q = 0.9 Å^{-1}], all relaxation times fall above the scaling line. The deGennes narrowing (de Gennes, 1979) predicts such a slow down of relative motion in phase with *S(q)*. For some pure polymers, it can be quite pronounced (Richter et al., 1998). A different scaling law is clearly evident in region III, where the dependence of relaxation times on momentum transfer is far less pronounced. Accordingly, region III, in addition to having a temperature dependence different than the other two regions, also is characterized by a different momentum transfer dependence. We now consider the possible origins for motion in each region.

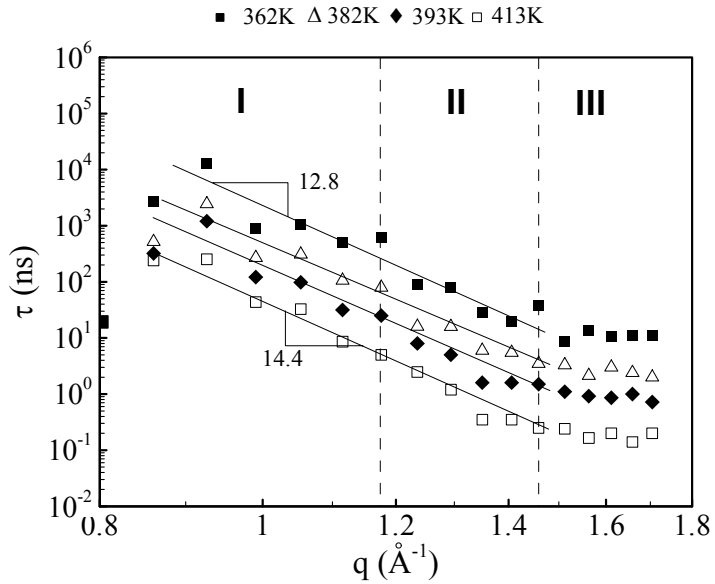

Fig. 4.7 Wavevector dependence of the characteristic times τ_{KWW} at 413 K for 30% blend.

Region I: In the superposed fits, the momentum transfer with the largest relaxation time, $q = 0.99$ Å^{-1}, corresponds to the intermolecular peak in the pure PMMA structure factor. This is evidenced by the entries in Table 4.4, as well as the data above the $-2/\beta$ scaling line in Fig. 4.7. Neutron scattering data on pure polymers have shown that in the vicinity of the intermolecular peak in *S(q)* the α-process is observed (Richter et al., 1998). It thus appears plausible to associate the region I relaxation with the PMMA α-relaxation. One way to test this is to examine the temperature dependence of the characteristic relaxation times. Figure 4.8 shows KWW relaxation times as a function of temperature for momentum transfers in regions I, II and III. The temperature dependence for the three regions at temperatures between *Tg* + 27 and *Tg* + 86 [the four highest temperatures] is not distinctly different. Although the Arrhenius form continues below *Tg* in region III, in regions I and II there is such a small decay in the NSE spectra that relaxation times cannot be assigned with NSE, implying they are larger than 10^4 ns. This rules out a continuing Arrhenius temperature dependence, and suggests a dependence following the Vogel form, although this cannot be confirmed without further data.

Also shown in Fig. 4.8 is the temperature dependence of terminal relaxation times obtained from oscillatory shear measurements (Colby, 1989). If region I observes the α-relaxation of PMMA, one would expect to see the same temperature dependence as in the mechanical data. The situation is complicated by the fact that the NSE data may actually observe a combination of PEO and PMMA motion, as well as the fact that relative, rather than self motion, is observed in our experiment, and the differences in temperature

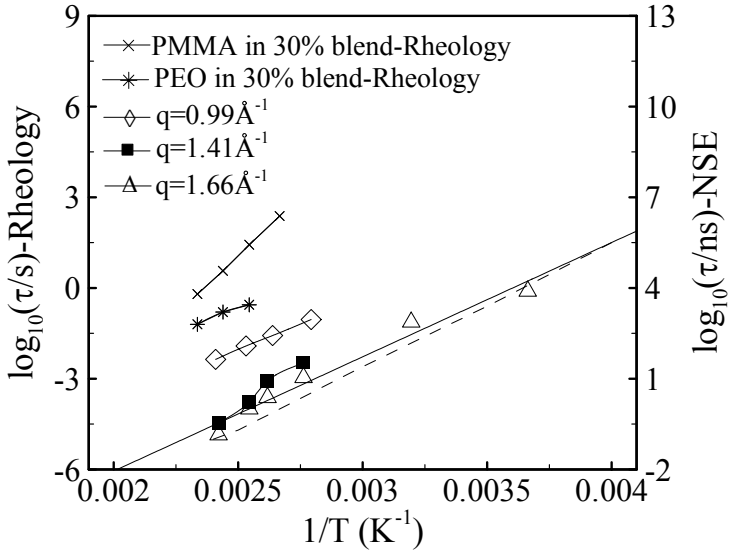

(a)

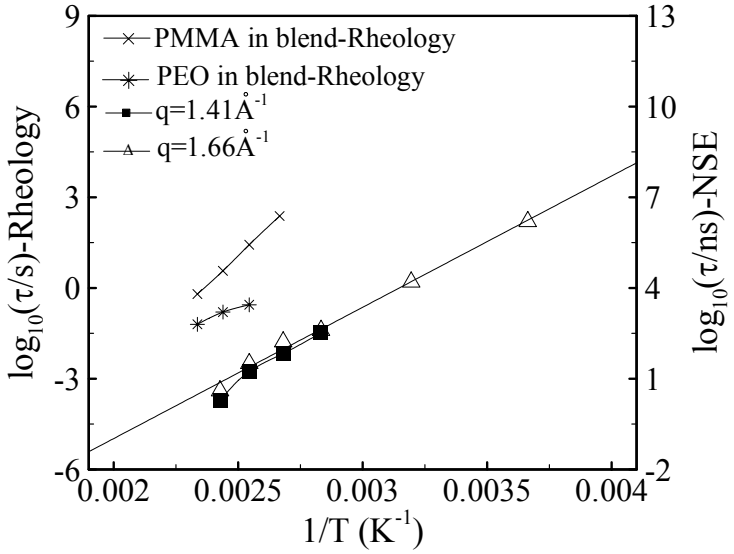

(b)

Fig. 4.8 Temperature dependence of the characteristic times τ_{KWW} from NSE and Rheology: (a) 30% blend, (b) 20% blend. The dashed line represents the temperature dependence of dielectric relaxation times from Bergman et al. (1998).

dependence between the two for miscible blends are unknown. Unfortunately, the comparison is not conclusive. The temperature dependence for all regions in the 30% blend [Fig. 4.8 (a)] looks more like PEO, while that in the 20% blend [Fig. 4.8 (b)] more closely resembles PMMA. It is likely that a combination of both components motion is observed.

As suggested in Fig. 4.4, the data in region I are consistent with the merged α/β-process in pure PMMA. This consistency breaks down at lower temperatures, where the pure PMMA dielectric relaxation times become larger than the NSE relaxation times. If the spectra in region I are tied to the α-relaxation of pure PMMA, it appears they are accelerated at low temperatures by the presence of PEO. This is consistent with current views of blend dynamics, which hold that the slow component will have a shift of its α-relaxation to shorter time scales.

Region II: Region II is located at momentum transfers where correlations between PEO and PMMA backbones are likely to occur. It also encompasses the first peak in the static structure factor of pure PEO (de Leeuw et al., 2001). This is the region where the quality of tTS declines, and where superposed relaxation times become quite large. The individual spectra have reasonable decays at high temperature, but are essentially flat [less decay than in regions I or III] at low temperatures. This strong temperature dependence suggests an α-relaxation. It is unclear whether PMMA motion, PEO motion, or a combination of the two is observed in this region. Complicating matters, the motion

of the low *Tg* component, PEO, is expected to be bimodal, and thus a fast or slow fraction of PEO may be probed by the experiment.

To test the possibility of PEO motion in region II, we consider a recent report of PEO motion in this blend using deuterium NMR (Lutz et al., 2003). The dNMR relaxation times of PEO over the temperature and composition range we study here are all less than ten ns, even below the blend *Tg,* and approach 1 ps at the high end of our temperature range. In contrast, our relaxation times are only less than ten ns at the highest temperature. From this we conclude that if the motion in region II corresponds to PEO dynamics, it would have to be the slow fraction of PEO that is observed – i.e. PEO segments surrounded by PMMA chains. At the same time, the NMR results would have to observe the fast fraction of PEO segments – those in a PEO dominated local environment. However, we cannot confirm this possibility, nor can we rule out the observation of PMMA motion in region II.

Region III: The surprising feature of the data in Fig. 4.6 is that there are relaxation times measurable on the timescale of NSE at temperatures well below *Tg* in region III. This is suggestive of a β-process, which does not change character at the glass transition. Relaxation times for the PMMA β-relaxation below *Tg* have been reported by Bergman, et al. from dielectric measurements (Bergman et al., 1998). At 75 and 53 degrees below *Tg*, relaxation times in pure PMMA are reported as $7.9*10^6$ and $6.3*10^5$ ns respectively. These may be compared to our superposed data at $T = 273$ [Table 5.4], which is 75 degrees below the 20% blend *Tg* and 53 degrees below the 30% blend *Tg*. Relaxation times for the 20% blend are of the order 10^6 ns, which is consistent with the dielectric

data, whereas relaxation times for the 30% blend are of order 10^4 ns. In both cases, motion continues well below *Tg*. The motion underlying the β-process is thought to be relatively insensitive to composition. Shown in Fig. 4.9 are relaxation times in region III as a function of distance above *Tg* for several momentum transfers in region III in both the 20% and 30% blends. It is evident from the Fig. 4.9 that the temperature dependence of characteristic times in region III follows an Arrhenius-like behavior, which again is suggestive of a β-process (Tetsutani et al., 1982a and 1982b). The activation energy for the β-process may be calculated as follows:

$$\tau = \tau_0 \exp\left(\frac{E_A}{kT}\right) \tag{4.2}$$

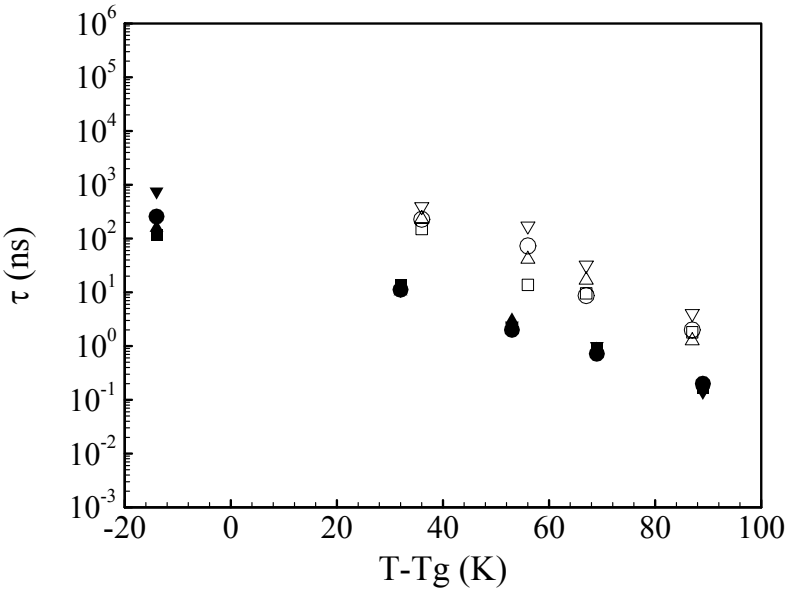

Fig. 4.9 Region III relaxation times for 20% and 30% PEO/PMMA blends. Filled symbols are for 30% blend: (■) q = 1.56 Å^{-1}, (▲) q = 1.61 Å^{-1}, (▼) q = 1.66 Å^{-1} and (●) q = 1.70 Å^{-1}; open symbols are for 20% blend: (□) q = 1.56 Å^{-1}, (Δ) q = 1.61 Å^{-1}, (∇) q = 1.66 Å^{-1} and (○) q = 1.70 Å^{-1}.

The activation energy we obtain at q = 1.70 Å^{-1} for 30% blend is 75 kJ/mol, which is in agreement with the activation energy of the local β-process for pure PMMA from dielectric results (Bergman et al., 1998; Garwe et al., 1996). A line with the dielectric PMMA activation energy is shown on the Figure. Using the same approach we obtain the activation energy (E_A = 81 kJ/mol) for the 20% blend at q = 1.70 Å^{-1} [shown in Fig. 4.8 (b)], which is close to that for the 30% blend, as shown in Table 4.5. This adds to our conjecture that the β-relaxation of PMMA dominates in this region.

Table 4.5 Comparison of activation energies for 20% and 30% blends at high q with that of the β-relaxation of pure PMMA.

Measurements	Activation energy *Ea* (kJ/mol)
20% PEO NSE	81
30% PEO NSE	75
dielectric β-relaxation*	79

* from Bergman et al. (1998)

As a final test of the correlation of dynamics in region III with the β-relaxation of pure PMMA, we refit the data for pure PMMA and both blends 1.70 Å^{-1} using

$$\frac{S(q,t)}{S(q,0)} = A * x_{PMMA} * \exp[-(\frac{t}{\tau_{KWW}})^{\beta}] \qquad (4.3)$$

where the prefactor A is obtained from fitting pure PMMA NSE data at T = 413 K, and x_{PMMA} is the weight fraction of PMMA in the blends. We have only taken data for pure PMMA at the highest temperature in our measurement range, as it decays very little

[413 K is 10 degrees above *Tg*] and only in region III. We use an average [over all momentum transfers in the region] of the stretching exponents obtained from the superposed fits of the 20 and 30% blends, $\beta = 0.125$. Figures 4.10 (a) and (b) show the results of this fitting procedure. We have included data on a 10% blend – for this blend reasonable decays are obtained only at the highest temperatures and momentum transfers, such as those represented in the Figure. At momentum transfers in region III, we can get good fits for pure PMMA and both blends using this scaling procedure, indicating that the observed relaxation process scales with PMMA composition. In contrast, this fitting procedure does not work in region II, as evidenced by the fits in Fig. 4.10 (b).

As evidenced by many factors, the relaxation process observed in region III, which corresponds to intramolecular correlations between the PMMA side group and main chain, is the β-relaxation in PMMA. The process has an Arrhenius temperature dependence continuing below *Tg*, with an activation energy consistent with that of the β-process in pure PMMA as determined by dielectric spectroscopy. The relaxation times do not change with composition if considered at constant $T + Tg$, and the observed spectra resemble that of pure PMMA and scale with PMMA composition.

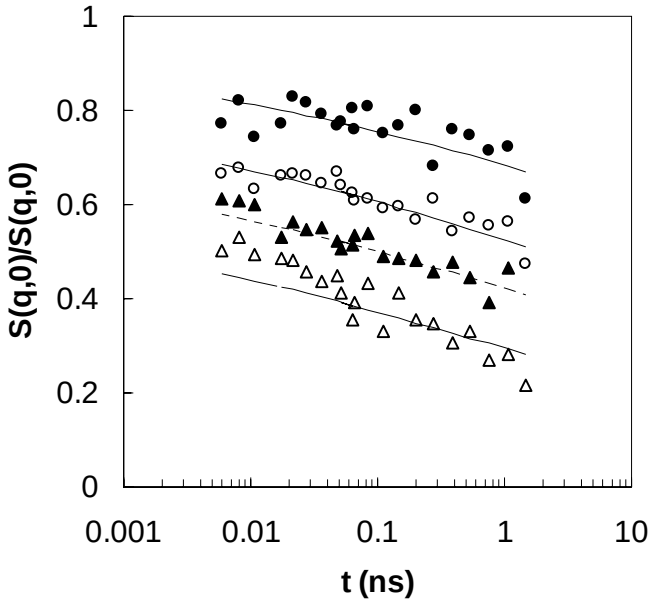

(a)

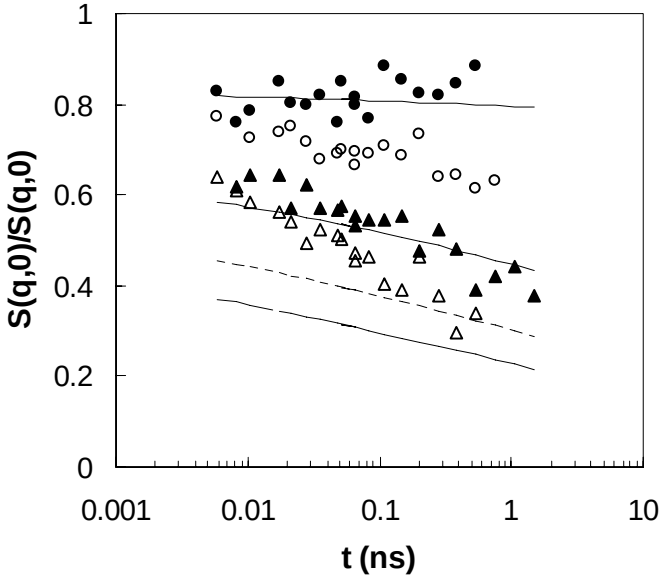

(b)

Fig. 4.10 NSE spectra for pure PMMA(•), 10% PEO blend(o), 20% PEO blend(▲) and 30% PEO blend(Δ) at $T = 413$ K, $q = 1.70$ Å^{-1}(a) and $q = 1.35$ Å^{-1}(b). Lines are fits to the KWW equation $S(q,t)=A*\chi_{PMMA}*exp(-(t/\tau_{KWW})^{0.125})$.

4.4 Conclusions

We have investigated the dynamics of 20% and 30% dPEO/dPMMA blends at six temperatures below and above the blend *Tg* and at wavevectors ranging from 0.86 $Å^{-1}$ to 1.70 $Å^{-1}$ using the NSE technique, which provides both time and spatial resolution. Our observations vary with spatial scale, and can be roughly divided into three regions. The first region, q = 0.86 to 1.23 $Å^{-1}$, contains the inter-chain structure factor peak of pure PMMA. Above the blend *Tg*, the data have an Arrhenius temperature dependence, and relaxation times are consistent with those of the α-relaxation of pure PMMA, when considered at the same $T + Tg$. Below the blend *Tg*, the spectra do not decay enough to assign relaxation times, suggesting that the Arrhenius dependence does not extend to lower temperatures. Since the closest temperature measured above *Tg* is *Tg* + 32, further measurements closer to *Tg*, but still far enough above it to obtain measurable relaxation times, are required to clarify the picture. In region II, where the peak in the static structure factor of pure PEO is located, the situation is very unclear. Similar to region I, the data show an Arrhenius temperature dependence above *Tg*, which must not continue at lower temperatures because the relaxation times quickly exceed the timescale of the experiment. The relaxation times above *Tg* far exceed those reported from NMR measurements, and thus if PEO motion is probed here, it is the slow portion of a bimodal distribution of relaxation times. In region III, NSE observes the β-process of PMMA, as evidenced by the following. Motion on this spatial scale is apparent far below the blend *Tg*. The temperature dependence of KWW relaxation times is Arrhenius throughout the temperature range of our measurements [*Tg* - 53 to *Tg* + 88 for the 30% blend] and has an

activation energy consistent with that obtained for the β-process in pure PMMA. Although a picture of the spatial dependence of motion in this system is emerging, additional measurements are required. In particular, incoherent measurements, where the mobility of each blend component in turn may be followed, will provide an important comparison for these data.

As a final comment, we mention that some decay in the scattering function occurs before the timescale of the NSE instrument. This fraction increases with increasing PEO content [see Fig. 4.10], and increasing temperature. This observation is consistent with the ideal of a bimodal distribution of PEO relaxation times in this blend. The fraction of PEO in a PEO rich environment would be expected to relax on timescales faster than the NSE technique, and to increase with PEO content and temperature. To test this possibility, a simulation study and the neutron scattering measurements that could extend to smaller time scales are necessary. In the following chapters, the results from molecular dynamics simulation and quasielastic neutron scattering are discussed.

Chapter 5
Simulation of Poly(ethylene oxide) with Different Models

This chapter compares static and dynamic properties obtained from two levels of modeling from molecular dynamics simulation of poly(ethylene oxide) (Chen et al., 2006a). Neutron scattering data are used as a test of each model's accuracy. The two simulation models are explicit atom (EA) model and a united atom (UA) model. Both models accurately describe the PEO static structure factor as measured by neutron diffraction. Dynamics are assessed by comparison to neutron time of flight data, which follows self motion of protons. Hydrogen atom motion from the EA model and carbon/oxygen atom motion from the UA model closely follow the experimental hydrogen motion, while hydrogen atoms reinserted in the UA model are too fast. The EA and UA models provide a good description of the orientation properties of C-H vectors measured by NMR experiments.

5.1 Introduction

As discussed in Chapter 2, molecular dynamics, which describes the movement of all the particles of a molecular system by iteratively solving Newton's equations of motion, has been used widely for understanding the chemical and physical properties of various materials on various length and time scales. Two most commonly used models of MD are explicit atom (EA) model and united atom (UA) model. There are some instances where EA modeling is required, for example, in the calculation of properties

such as the vibrational density of states, methyl group rotation, and elastic constants of crystalline polymers. The UA representation is widely used because it is computationally efficient, while providing results in reasonable agreement with available experimental data.

Force fields for EA and UA models are highly developed for many materials. They are typically obtained from ab initio calculations or by tuning parameters to experimental observables. A series of comparison studies (Smith and Yoon, 1993; Yoon et al., 1993; Paul et al., 1995; 1997) have been conducted on n-alkanes using EA and UA models. It was shown that both EA and UA models quantitatively reproduced both structural and dynamic data. McCoy and Curro (1998) and Tsige et al. (2003) proposed a UA/EA mapping procedure to obtain a UA potential from an EA potential which was tested on $C_{20}H_{42}$ and $C_{48}H_{98}$ in the liquid state. They found excellent agreement between liquid structure and chain dimensions from the two models, but the UA potential obtained from UA/EA mapping exhibited attractions that were too strong as evidenced by a negative pressure and high compressibility.

This chapter is to evaluate our simulation models for PEO by comparing results from the EA and UA levels of description with the neutron scattering. PEO has attracted a lot of attention because of its wide applications ranging from use as a solid polymer electrolyte to treatment of surfaces for resistance to protein adsorption. EA models for PEO have been developed by Smith and his colleagues (Smith et al., 1993; 2003; Borodin and Smith, 2003; Borodin et al., 2003) and Neyertz et al. (1994). Smith's model agrees with experimental data for both static and dynamic properties, while Neyertz's model reproduces the structures of crystalline and melt PEO. van Zon et al. (2001) obtained a

UA force field based on a modification of Neyertz's EA force field and showed that the intermediate scattering function calculated from this UA model is in good agreement with neutron spin-echo experiments.

In this chapter, we adopt Smith's EA and van Zon's UA force fields. We perform a series of comparisons on the structure and dynamics of PEO above the melting temperature using both models. Model performance is evaluated based on agreement with neutron measurements of both structural and dynamic observables.

5.2 Simulation details

5.2.1 Model

All the simulations were performed on a system of 27 chains with the structure of CH_3-CH_2-$[OCH_2CH_2]_{29}$-OCH_2CH_3 at a series of temperatures of 300, 343, 375, 400, 430, 450, and 500 K, all of which are above the melting point of PEO. The system was initially simulated at 500 K. Higher and lower temperatures were reached by cooling or heating in stages, allowing for equilibration at each stage. The PEO chains thus consist of 92 backbone atoms and have a molecular weight of 1350 g/mol. The cut-off distances for the nonbonded interactions are 10 Å in UA simulations and 8 Å in EA simulations. The force fields for the united atom model are obtained from Neyertz and Brown (1995) and de Leeuw et al. (2001), and those for the explicit model are taken from Smith et al. (2002). They are summarized in Tables 5.1 and 5.2.

Table 5.1 UA model Parameters.

Bonds	$u^{bond}(r_{ij}) = \frac{k_{bond}}{2}(r_{ij} - r_{ij}^0)^2$	
	k_{bond} (kJ/mol/Å^2)	r_{ij}^0 (Å)
C-C	2587.4	1.54
C-O	3094.0	1.43

Bends	$u^{bend}(\theta_{ijk}) = \frac{k_{bend}}{2}(\cos\theta_{ijk} - \cos\theta_{ijk}^0)^2$	
	k_{bend} (kJ/mol)	θ_{ijk}^0 (degrees)
O-C-C	727.7	110.0
C-O-C	1070.1	112.0

Torsion (kJ/mol)	$u^{torsion}(\phi_{ijkl}) = \sum_{k=0}^{6} a_k \cos^k \phi_{ijkl}$						
	a_0	a_1	a_2	a_3	a_4	a_5	a_6
O-C-C-O	2.211	15.194	17.844	−32.460	−13.871	−1.189	12.322
C-C-O-C	5.183	5.610	6.272	−15.428	−0.678	−4.568	3.567

Nonbonded interaction	$u^{nb}(r_{ij}) = \varepsilon_{ij}\left[\left(\frac{\sigma_{ij}}{r_{ij}}\right)^{12} - 2\left(\frac{\sigma_{ij}}{r_{ij}}\right)^{6}\right] + \frac{1}{4\pi\varepsilon_0}\frac{q_i q_j}{r_{ij}}$		
	Mixing rules	$\sigma_{ij} = \frac{1}{2}\sigma_i + \frac{1}{2}\sigma_j$	$\varepsilon_{ij} = \sqrt{\varepsilon_i \varepsilon_j}$
	σ_i (Å)	ε_i (kJ/mol)	q_i (e.c.)
CH_3	4.152	1.047	0
CH_2	4.068	0.831	0.174
O	3.405	0.401	−0.348

Table 5.2 EA model Parameters.

Bonds	$u^{bond}(r_{ij}) = \frac{k_{bond}}{2}(r_{ij} - r_{ij}^0)^2$	
	k_{bond} (kJ/mol/Å^2)	r_{ij}^0 (Å)
C-C	2587.4	1.513
C-O	3094.0	1.390
C-H	2742.4	1.090

Bends	$u^{bend}(\theta_{ijk}) = \frac{k_{bend}}{2}(\theta_{ijk} - \theta_{ijk}^0)^2$	
	k_{bend} (kJ/mol/rad)	θ_{ijk}^0 (degrees)
C-C-H	359.2	458.4
H-C-H	322.6	453.4
O-C-C	498.2	456.5
O-C-H	468.9	460.8
C-O-C	623.8	467.1

Torsions (kJ/mol)	$u^{torsion}(\phi_{ijkl}) = -0.5 \cdot \sum_{k=0}^{3} a_k \cos(k \cdot \phi_{ijkl})$			
	a_0	a_1	a_2	a_3
O-C-C-H	1.164	0.000	0.000	−1.164
H-C-O-H	1.164	0.000	0.000	−1.164
C-O-C-H	3.382	0.000	0.000	−3.382
O-C-C-O	10.886	0.209	−10.676	0.000
C-O-C-C	8.457	−4.187	−2.931	−1.340

Nonbonded interaction	$u^{nb}(r_{ij}) = A_{ij}\exp(-B_{ij}r_{ij}) - \frac{C_{ij}}{r_{ij}^6} + \frac{1}{4\pi\varepsilon_0}\frac{q_i q_j}{r_{ij}}$			
	A_{ij} (kJ/mol)	B_{ij} (Å)	C_{ij} (kJ/mol·Å^6)	q_i (e.c.)
C-C	62701.5	3.090	2682.9	−0.163, −0.1065*
O-O	317547.0	4.063	1670.0	−0.256
H-H	11093.3	3.740	114.6	0.097, 0.0355×
C-H	18087.0	3.415	578.8	
C-O	141105.2	3.577	2116.7	
O-H	59352.0	3.902	437.4	

*the second entry is for end group CH_3 methyl carbon atoms
×the second charge is for end group CH_3 methyl hydrogen atoms

The size of simulation box is set by the polymer densities at corresponding temperatures, which are calculated from

$$\rho = \frac{\rho_0}{\exp(\alpha \cdot (T - T_0))} \tag{5.1}$$

where ρ_0 is the reference density, T_0 is the reference temperature, and α the isothermal expansion coefficient, which is calculated from the data of Smith et al. (1996). The densities for the corresponding temperatures are listed in Table 5.3.

Table 5.3 Densities of PEO at different temperatures.

T (K)	Density (g/cm^3)
300	1.12200
343	1.08873
375	1.06461
400	1.04615
430	1.02441
450	1.01016
500	0.97542

5.2.2 Equilibration

All systems are equilibrated for at least 2 ns before collecting data, followed by production runs of 4 ns. In all the cases, the atoms have moved at least 1*Rg* during the equilibrium period, and no drifts in structural properties [intermolecular $g^{inter}(r)$] are evident. As a further test of equilibration, we choose a dynamic observable, the self intermediate scattering function *S(q,t)*, and calculate their values over three 1 ns blocks following the proposed equilibration of 2 ns. As shown in Fig. 5.1, no drifts are observed, suggesting that the equilibration time is sufficient. Similar results are also obtained for the models.

5.3 Experimental details

5.3.1 Neutron diffraction

Neutron diffraction experiments were performed on perdeuterated PEO [M_w = 460 000 g/mol] at the NIST Center for Neutron Research in Gaithersburg, MD. The sample used was perdeuterated to avoid the large incoherent signal from hydrogen, and ensure that the scattered intensity is dominated by coherent scattering. The BT-7 triple-axis spectrometer was employed with the standard configuration of a double-crystal pyrolytic graphite monochromator and an incident wavelength of 2.47 Å. A 5-cm thick pyrolytic graphite filter was employed to suppress higher order wavelength contaminations. Natural collimation was used before the sample with an effective divergence of 30′ and a Söller slit collimator of 27′ full-width-at-half-maximum. The sample was mounted in an

aluminum sample holder and in a closed cycle refrigerator. The investigated q range is from 0.5 $Å^{-1}$ to 3.9 $Å^{-1}$, and the temperature measured is 343 K.

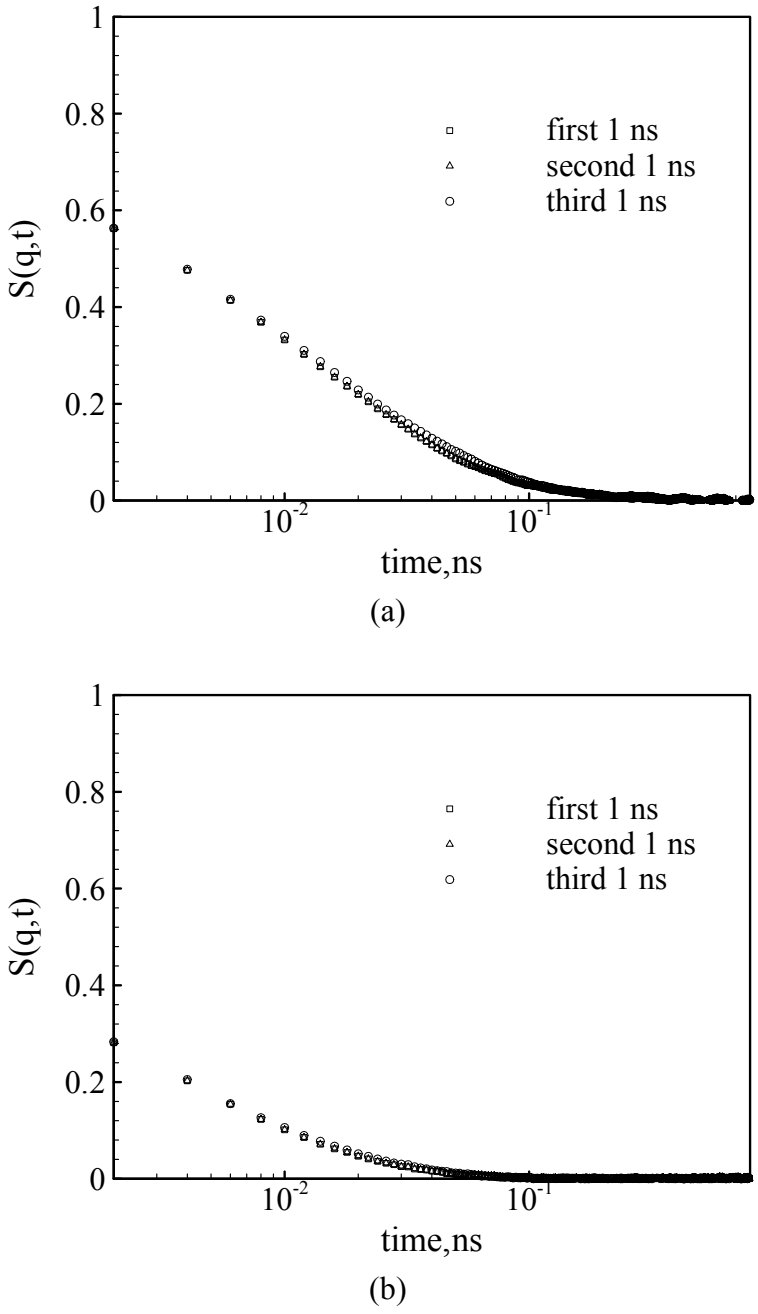

Fig. 5.1 Self-intermediate scattering function from the EA model of PEO calculated over 1 ns blocks at two q values of: (a) 1.5 $Å^{-1}$; (b) 2.3 $Å^{-1}$. (Chen et al., 2006a)

5.3.2 The disk chopper spectrometer (DCS)

Time-of-flight measurements were performed on the disc chopper spectrometer (Copley and Cook, 2003) [DCS] also at the NIST Center for Neutron Research. In this case hydrogenated PEO [M_w = 463 000 g/mol] was used, so that the large incoherent cross section of hydrogen ensures that the signal from the DCS measurement is dominated by self motion of the hydrogen atoms. The spectrometer was operated at an incident wavelength of 4.2 Å and at a resolution of 0.08 meV (full width at half-maximum). The sample is annular in shape and held in a thin-walled aluminum can mounted onto a closed-cycle refrigerator. Sample thicknesses were kept around 0.2 mm to achieve transmissions of ≈ 90% and avoid multiple scattering effects. The instrumental resolution was measured using a vanadium sample at 295 K and the same instrument configuration. The measured QENS spectra collected over 6 hr periods were corrected for detector efficiencies using software developed at NIST (Data Analysis and Visualization Environment, DAVE, http://www.ncnr.nist.gov/dave). Subsequently, the scatterings from the empty aluminum can and from the background were subtracted and the data were binned into q groups in the range 0.60-2.60 $Å^{-1}$.

5.4 Local structure and chain conformation

In this section we present results on the structure and conformational properties of PEO melts investigated by EA and UA simulations, and neutron diffraction experiments. Two levels of comparison are made: testing agreement with experiment by reinserting

missing atoms, and compare the structural properties directly between the simulation models.

5.4.1 Agreement with experiment

For the purpose of comparison between simulation models and diffraction data, the missing deuterium atoms were reintroduced into the UA systems as discussed in Section 2.7. This allows us to calculate an atomistic static structure factor *S(q)* of an isotropic sample using Eqs. (2.38) and (2.39). As the static structure factor *S(q)* is normally measured on deuterated samples, we use the coherent scattering length for deuterium rather than hydrogen.

The scattered intensity for PEO as calculated from Eqs. (2.38) and (2.39) and as measured by neutron diffraction is shown in Fig. 5.2. For the simulation data, we show *S(q)* calculated from EA and UA simulations with all the missing atoms reinserted. Because many factors (neutron flux, incoherent background, etc) influence the scattering intensity from diffraction experiments, the arbitrary rather than absolute coherent intensity, is obtained. The incoherent background may be removed with polarization analysis, but BT7 is not equipped to do so. To evaluate agreement between simulation *S(q)* and neutron diffraction, we match the intensity of the first peak at q = 1.5 $Å^{-1}$, and then compare the shapes of the two curves. The spectra obtained from the simulation closely follow the actual diffraction pattern and there is no evidence of crystallinity. This indicates that both simulation models capture the packing characteristics of PEO melts. Figure 5.2 also shows that pure PEO is characterized by a first peak at q = 1.5 $Å^{-1}$, and a second peak at q = 3.0 $Å^{-1}$. As expected and presented in Fig. 5.3, with EA simulation as

an example, the origin of the first peak is intermolecular, while the second peak is consistent with intramolecular packing.

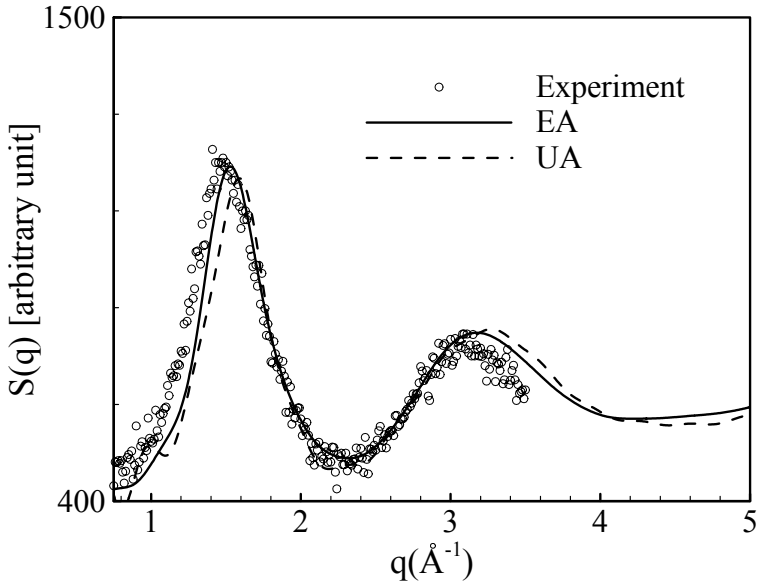

Fig. 5.2 Comparison of the static structure factors of PEO from UA and EA simulations and neutron diffraction experiments at 343 K (Chen et al., 2006a).

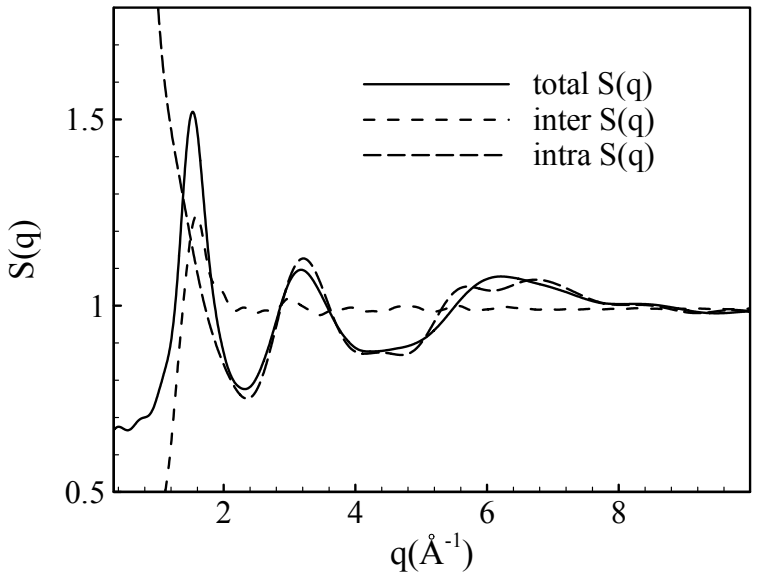

Fig. 5.3 Inter- and intramolecular contributions to the total structure factor *S(q)* from EA simulations (Chen et al., 2006a).

5.4.2 Comparison between simulation models

Here we assess chain dimensions from both models without inserting the missing atoms to united atom model. The radius of gyration (*Rg*) and end-to-end distance (*Re*) are calculated for both simulation models using Eqs. (2.34) and (2.35) and Eq. (2.36), respectively. In this case, all available atomic positions in each level of description are included. Table 5.4 presents the comparison results. Although in general agreement is good, UA chains are more extended than EA chains. This is expected, because the equilibrium bond lengths and angles in the EA model for groups involving carbon and oxygen are smaller than their UA counterparts.

Table 5.4 Comparison of conformational properties of PEO melts from EA and UA simulations.

models	EA	UA
Rg (Å)	10.65 ± 0.53	12.18 ± 0.60
Re (Å)	25.80 ± 1.21	30.02 ± 1.58

errors are standard deviation.

5.5 Local dynamics

5.5.1 Mean square displacement (MSD)

The mean squared displacement of individual atoms is evaluated by Eq. (2.41). Since the motion of protons is the relevant variable for comparison to neutron experiments, and they must be reintroduced to the UA model, in Fig. 5.4 we compare

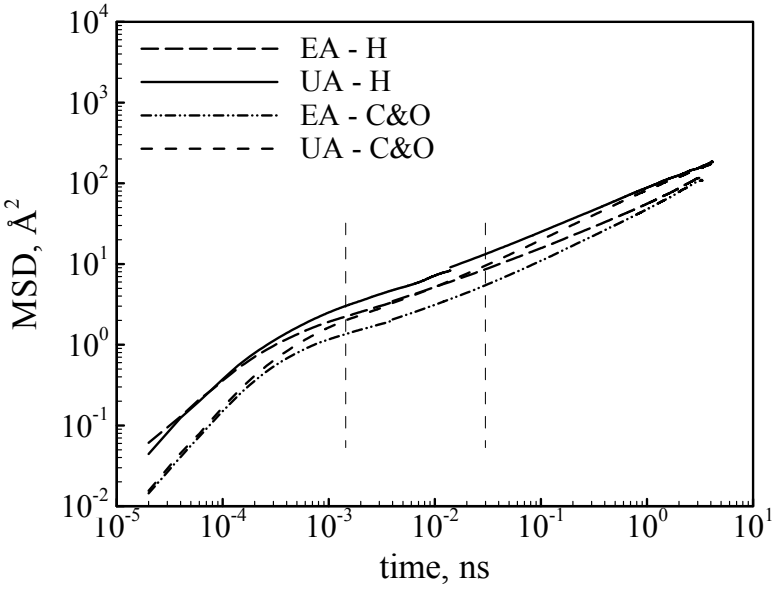

Fig. 5.4 Comparison of mean square displacements for hydrogen atoms and carbon/oxygen atoms from EA and UA simulations. The region between two dashed lines indicates the time range for our time of flight measurements (Chen et al., 2006a).

motion of hydrogen atoms in the EA model with motion of the hydrogen atoms that have been reinserted in the UA model. Carbon and oxygen atom motions, which are calculated explicitly in both models, are also shown. The figure illustrates that the difference in mobilities of EA and reintroduced UA hydrogen atoms is similar to that in EA and UA carbon/oxygen atoms, indicating that the reintroduction of protons to the UA coordinates is reasonable. Hydrogen atoms move further than backbone carbon and oxygen atoms. This is reasonable based on the smaller mass of the hydrogen atoms. At longer times [~1 ns], the mean squared displacements of hydrogen and backbone atoms move together in both models, as expected because motion at long times represents diffusion of the entire chain. There exists a time range [0.001 to 0.1 ns] where the UA carbon/oxygen and EA hydrogen atom mean square displacements are coincident. Since

this time range represents a major portion of that probed by quasielastic neutron scattering measurements, this suggests that neutron measurements will agree more closely with UA models if the hydrogen atoms are not reinserted. We return to this point below.

5.5.2 Self intermediate scattering function

DCS measures the dynamic structure factor $S(q,\omega)$, which is the time Fourier transform of the intermediate dynamic structure factor $S(q,t)$. As discussed above, in hydrogenated PEO, the signal is dominated by incoherent scattering of hydrogen atoms. Although in principle the experiment has a contribution from coherent scattering, this is small (~3%) and we do not include it. $S(q,t)$ can be determined for all atoms from simulation trajectories. The self intermediate scattering function is calculated through Eq. (2.44). For the EA model, this function was calculated using hydrogen atom positions, and again using carbon and oxygen atom positions. The same was done for the UA model after reinsertion of the hydrogen atoms. The performance of the UA and EA is evaluated by comparison to DCS data.

Plotted in Fig. 5.5 is the $S(q,t)$ calculated from UA and EA simulation trajectories and measured from DCS experiments at two q values (q = 1.5 Å^{-1} and q = 2.3 Å^{-1}). As described above, decays calculated using both hydrogen and backbone carbon/oxygen atom positions are shown for each model, for a total of 4 curves. The most direct comparison is that between hydrogen atom positions in the EA model and DCS experiments. In this case, reasonable agreement is found for times greater than 1 ps. In

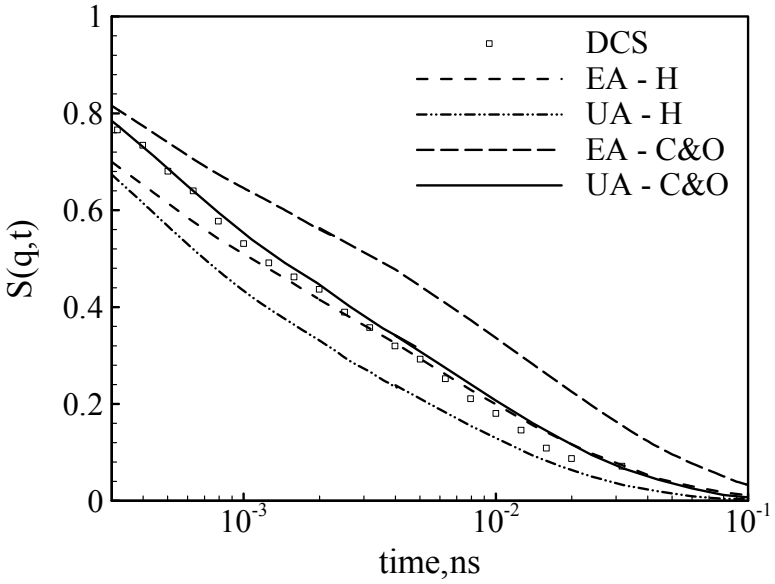

(a)

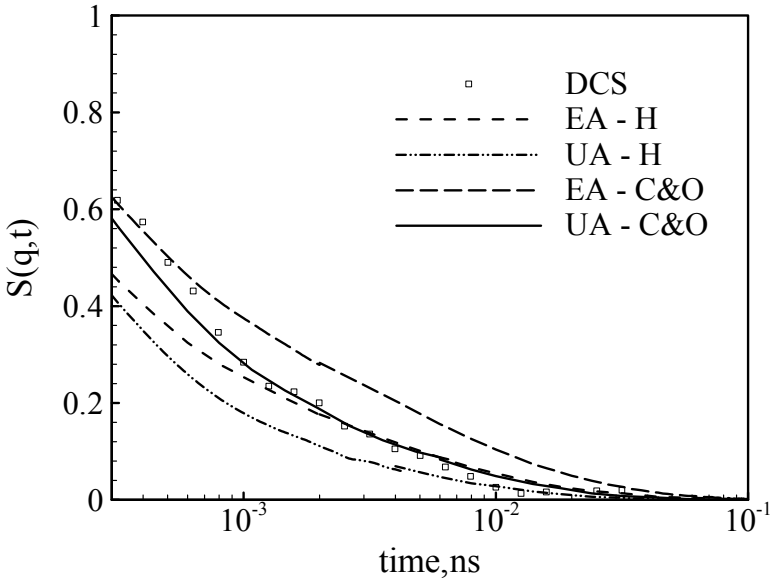

(b)

Fig. 5.5 Comparison of hydrogen atom and carbon/oxygen atom dynamics from EA simulations, UA simulations and DCS measurements at: (a) q = 1.5 Å^{-1}; (b) q = 2.3 Å^{-1}. (Chen et al., 2006a)

this time range the UA carbon/oxygen positions also match the experimental data quite well, as anticipated from Fig. 5.4. Surprisingly at shorter times, the DCS data is in better agreement with the UA carbon/oxygen data than that calculated from hydrogen positions. Although motion from the EA protons most closely represents the QENS data, it appears that the cross-over from the ballistic regime occurs too early, and the tail end of this local motion, observable in the DCS data, is missed for EA protons. Since this cross-over occurs later for backbone atoms, some of their fast decay appears in this time range such that it best describes the DCS data. As we expect a similar difference in ballistic motion regardless of the system and the coincidence of UA backbone and EA hydrogen motion appears to be related to the exit of the ballistic regime which occurs at nearly the same time for many polymers, we anticipate this correspondence to be observed in many systems where UA modeling is employed. This is indeed the case, as similar observations have been reported in other systems (Smith et al., 1997). We conclude that the best description of the experimental data derives from the backbone atoms of the UA model and that the EA hydrogens also provide an excellent description at times greater than 1 ps. The performance of the EA model appears better as q becomes smaller. Clearly, when using a UA model, it is preferable not to reinsert the hydrogen atoms, as the UA-H curve does not provide satisfactory agreement at any time.

While the fast process [times shorter than 1 ps] arises from the unhindered motion in a cage formed by nearest neighbors, the slow process [times longer than 1 ps] originates from the merged $\alpha\beta$ process. In order to quantify the second process and extend our comparison to all investigated q values, we fit this portion of curve with Eq. (2.47). The resulting fit parameters are reported in Fig. 5.6 for DCS measurements, and

for UA and EA simulations where both hydrogen and backbone motions are considered. We note that at the lower end of the q range depicted in this figure, the small molecular weight of the simulated system likely results in smaller relaxation times than would be obtained from a sample with longer chains.

It is clear from Fig. 5.6 (a) that as anticipated above, the relaxation times of UA carbon/oxygen atoms match those from DCS measurements at all available momentum transfers, while the EA hydrogens match for q smaller than 2 $Å^{-1}$. Relaxation times derived from EA carbon/oxygen atoms and UA hydrogen atoms are not accurate at any spatial scale. At q values greater than the intermolecular packing region ($q < 1$ $Å^{-1}$), the hydrogen and backbone atom relaxation times for both UA and EA simulations begin to merge, just as their mean squared displacements become coincident at long times. At even larger spatial scales, relaxation times from both levels of modeling merge. Outside the DCS range coincident values of hydrogen and carbon/oxygen relaxation times are apparent for spatial scales comparable to *Re* ($q \approx 0.23$ $Å^{-1}$). This confirms that for whole chain motion, it does not matter which type of atom is tracked. Note that the spatial scale corresponding to *Rg* [indicated by a dashed line in Fig. 5.6 (a)] is not large enough to produce this effect. Within the region where hydrogen and carbon/oxygen times have merged, but UA and EA models are distinct, UA relaxation times are approximately two times faster than those from the EA simulation indicating a potential disagreement in quantities such as diffusion coefficients.

The scatter in β is larger than that in τ with all values clustered around $\beta = 0.6$ as shown in Fig. 5.6. Both EA and UA models seem to adequately capture the experimentally observed distribution of relaxation times. β increases with decreasing q

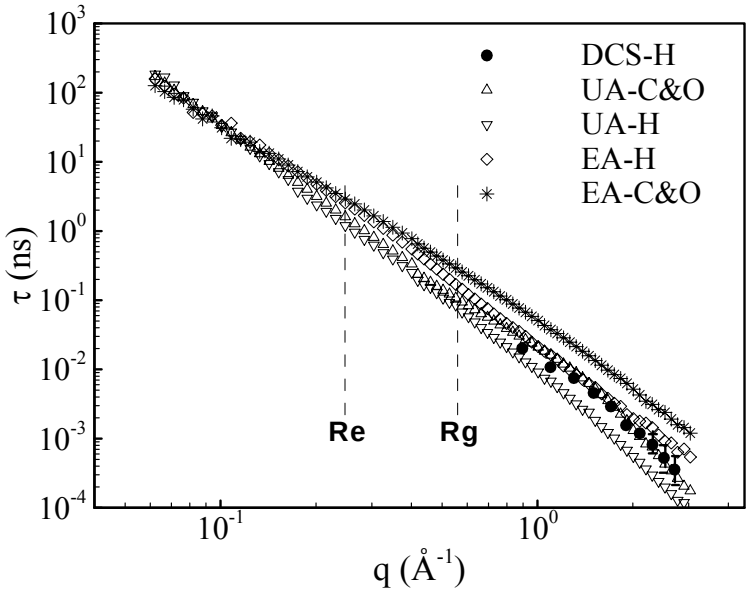

(a)

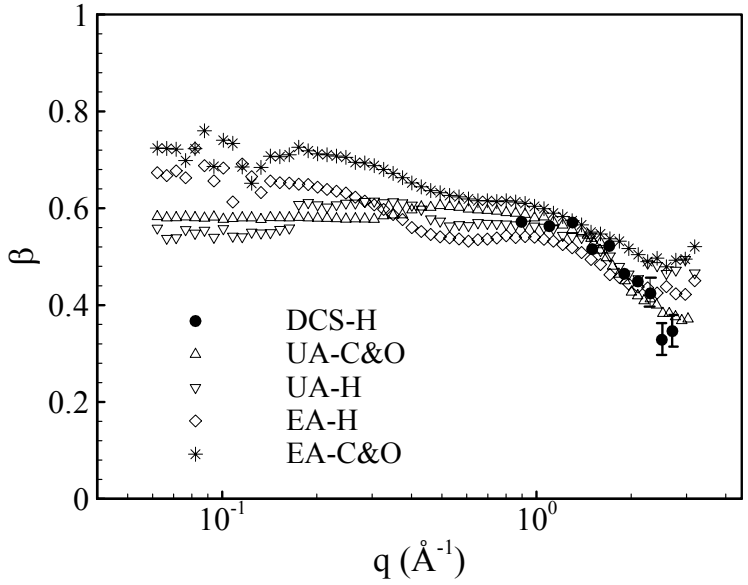

(b)

Fig. 5.6 The q dependence of KWW fitting parameters from EA simulations, UA simulations and DCS experiments: (a) relaxation time; (b) stretching parameter β. (Chen et al., 2006a)

and at larger spatial scales levels off at an almost constant value. The q value at which β begins to level off coincides with that where the backbone and proton relaxation times begin to merge, indicating that reaching a q independence of β is related to whole chain motion. At spatial scales on the order of interchain packing or less, it is more likely for individual atoms to encounter an environment that is locally slower or faster than the average arising from dynamic heterogeneity. As the spatial scale is increased, it will eventually be large enough to include a variety of locally slower or faster environments, which would result in an increasing value for β (smaller distribution), followed by a leveling off when increasing the spatial scale has no further effect. This would suggest that the typical spatial scale of a local dynamic region is less than *Rg*, and probably comparable to interchain packing.

5.5.3 Orientation autocorrelation function (OACF)

The orientation autocorrelation function is the frequency Fourier transform of a spectral density function $J(\omega)$ which is measurable in NMR experiments (Lutz et al., 2003). It describes the decorrelation of the orientation of the C-H bond vector. From the trajectory obtained from simulations, the OACF can be calculated according to Eq. (2.46). We present the results for UA, EA simulations and NMR experiments (Lutz et al., 2003) in Fig. 5.7. Note that to calculate the C-H bond properties, hydrogen atoms must be inserted to UA model. Both the EA and UA models describe the experimental data reasonably well with equal levels of agreement. It is reported that the C-H vector reorientation occurs via two mechanisms, librational and segmental motions, in which

case the OACF can be represented by the following functional form (Qiu et al., 2000; Min et al., 2001),

$$G(t) = a_{lib} \exp(-\frac{t}{\tau_{lib}}) + (1 - a_{lib}) \exp\left[-(\frac{\mathrm{t}}{\tau_{\mathrm{seg}}})^{\beta} \right] \tag{5.2}$$

where a_{lib} and τ_{lib} are the amplitude and relaxation time for librational motion and τ_{seg} the relaxation time for segmental motion. We fit *G(t)* presented in Fig. 5.7 using Eq. (5.2) with τ_{lib} = 1 ps as was done by Lutz et al. (2003). The resulting parameters are listed in Table 5.5. The value of a_{lib} is smaller in both the UA and EA representations indicating the contribution of librational motion is less in the simulation models. Stretching parameters and relaxation times from either simulation model are close to those from NMR experiments. We also report the correlation time for segmental dynamics $\tau_{seg,c}$ which is the time integral of the segmental portion of the correlation function:

$$\tau_{seg,c} = \frac{\tau_{seg}}{\beta} \Gamma(\frac{1}{\beta}) \tag{5.3}$$

These times, from both simulation models, also closely match the NMR results. We conclude that the local motion represented in the reorientation of the C-H bond vector can be adequately described by either the EA or UA representations.

Table 5.5 Comparison of parameters from current UA, EA simulations and NMR experiments by Lutz et al. (2003).

models	a_{lib}	β	τ_{seg}(ps)	$\tau_{seg,c}$(ps)
UA	0.07	0.34	7.9	42
EA	0.05	0.36	11.9	55
NMR	0.10	0.33	10	62

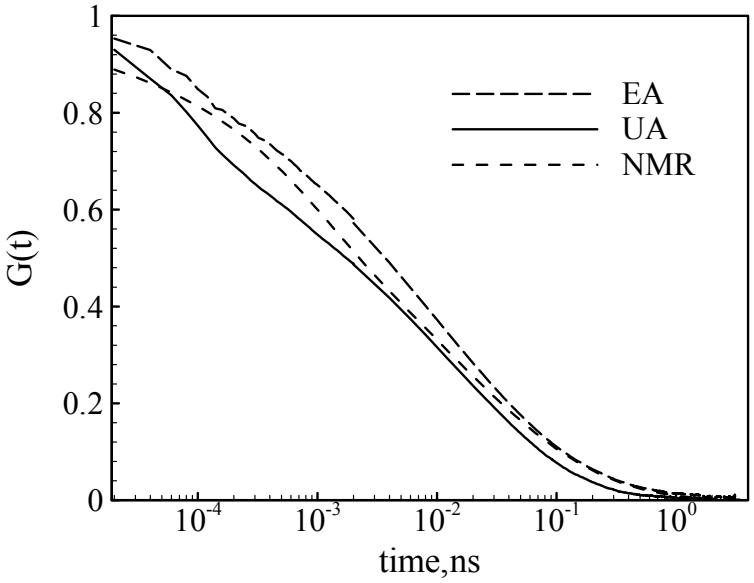

Fig. 5.7 Orientation autocorrealtion functions for C-H vectors calculated at 343 K from EA, UA models and NMR experiments. (Chen et al., 2006a)

5.6 Summary and conclusion

A variety of descriptions are available for chemically detailed simulations of polymer melts. Here we have presented a detailed comparison of two levels of modeling for a polymer, PEO, which is both well studied and has several important applications, including use as a solid polymer electrolyte, and as a coating to prevent adsorption of proteins to surfaces. We compare and evaluate the performance of EA and UA models for both static and dynamic observables, using neutron scattering and NMR data. We find no clear evidence that the EA model provides more accurate results than the UA model for any of the observables considered. The performance of both models is comparable and in agreement with neutron diffraction for static properties. The dynamics represented via QENS experiments are in reasonable agreement with the EA

model. The UA model also performs adequately, but only in the case that backbone carbon and oxygen atom motion is compared to the proton motion probed in the experiment. The dynamics of protons reinserted in the UA simulation do not agree well with QENS data. Both UA and EA data do provide a good description of NMR data, where the performance of both models is comparable.

Chapter 6
Local dynamics of Syndiotactic Poly(methyl methacrylate)

This Chapter investigates the local dynamics of syndiotactic poly(methyl methacrylate) by explicit atom molecular dynamics (MD) simulations and quasielastic neutron scattering (QENS) at temperatures well above the glass transition temperature. Using MD, we are able to isolate specific local motions well above *Tg*. These include rotations of the α- and ester methyls, rotations of the entire ester side group and segmental motion of the chain backbone. This capacity is unique to simulation as proton motion at high temperatures necessarily involves multiple motions. The force field used is validated by direct comparison to structural and dynamic neutron scattering measurements, and by comparison via temperature extrapolation of activation energies and rotational times for methyl group rotations. We find that the rotation of the ester side group is consistent with the β-relaxation at low temperatures: the activation energy closely matches that assigned from dielectric spectroscopy (DS), and relaxation times are also consistent with these measurements. The nature of the rotation does not appear to be a 2-fold jump as previously suggested, but through continuous small angle rotations with no preferred spatial orientation. The α-relaxation is associated with the motion of the main chain. Relaxation times for these protons are not Arrhenius, but rather begin to diverge as the temperature is lowered. Rotation of the slower α-CH_3 group occurs with rates similar to the α- and β-relaxations in the temperature range we investigate. Both this rotation and that of the ester side group are more prominent at smaller scales and explain why neutron

scattering measurements on PMMA reveal the α-relaxation as the spatial scale is increased.

6.1 Introduction

As discussed in Section 1.1, the α-relaxation, which arrests at the glass transition temperature *Tg*, is commonly associated with the segmental relaxation of the main chain. Polymer molecules, especially those with side groups, have other relaxation processes known as secondary relaxations (Ritchter et al., 1998; Karatasos et al., 2001 and 2002). Poly(methyl methacrylate) [PMMA] is one such polymer and its repeat unit is illustrated in Fig. 6.1. Secondary processes in PMMA include rotations of the ester and α-methyl groups and the β-relaxation, which has been linked with the reorientation of the entire ester side group around the C-C bond linking it to the backbone. At temperatures well above *Tg* all processes are active; below *Tg* the segmental relaxation is frozen and only secondary relaxations are active. As a result, at temperatures above *Tg*, secondary motions may merge with those of the main chain making individual assessment difficult.

The β-relaxation is normally prominent in dielectric measurements for PMMA. 2D and selective-excitation 3D exchange NMR techniques (Schmidt-Rohr et al., 1994) have been applied to explore the molecular motion underlying the β-relaxation in PMMA below *Tg*. These experiments show that the OCO plane of the side group undergoes 180^{o} flips which are related to the β-relaxation. This side-group flip is accompanied by a main chain rearrangement.

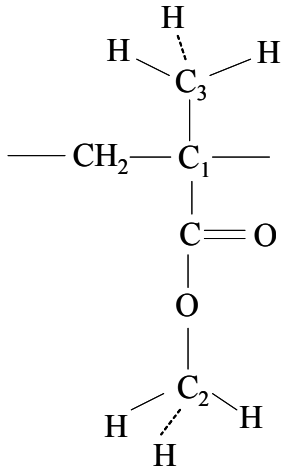

Fig. 6.1 Chemical structure of the repeat unit of PMMA (Chen et al., 2006b).

Recently our group initiated a quasi-elastic neutron scattering [QENS] study of the segmental dynamics of PMMA and how they are influenced by blending with poly(ethylene oxide) [PEO] (García Sakai et al., 2004). This neutron measurement showed that pure PMMA displays different relaxation behavior at different spatial scales. At spatial scales larger than the interchain peak, relaxation times increase rapidly as the temperature is decreased toward the glass transition temperature: typical for the α-relaxation. At intrachain spatial scales the temperature dependence of relaxation times is Arrhenius with an activation energy of 118 kJ/mol, consistent with the merged $\alpha\beta$ process. These experiments were performed above *Tg* and thus potentially include contributions from all motions, including secondary relaxations in PMMA.

Rotation of the methyl groups is the most straightforward motion in PMMA. This rotation is often approximated by an effective one-dimensional single particle potential, and is usually represented by instantaneous jumps between three equi-distant sites on a

circle (Prager and Heidemann, 1997; Moreno et al., 2001b). The resulting rotational motion often falls within the experimental frequency range of neutron scattering at temperatures below *Tg*. This technique, combined with deuterium labeling, has been successfully employed to investigate the rotational dynamics of ester methyl group rotations (Moreno et al., 2001a; Arrighi et al., 1995; Arrighi and Higgins, 1996; Allen and Higgins, 1973). Rotation of the α-methyl is slower and not as thoroughly investigated (Heijboer et al., 1987).

As discussed above, at higher temperatures the relaxation of PMMA appearing in the QENS window is a combination of α-methyl group rotation, ester methyl group rotation, β-relaxation, and α-relaxation. It is therefore difficult to retrieve specific local motions using this technique even with deuterium labeling, because the same protons may participate in more than one type of motion. In the current contribution, we use molecular dynamics simulation to separate these motions. Simulations also allow us to explore and validate specific mechanisms for motion directly: for example, the association of the α-relaxation with motion of the chain backbone, and connection of the β-relaxation to the rotation of the ester side group. At the same time, only a few works have been done on PMMA MD simulations (Soldera, 1998; Apel et al., 1995; Soldera and Metatla, 2005) and therefore we also propose a force field for this purpose and validate it against QENS data.

Note that in this chapter, we mainly focus on explicit atom simulation, since united atom model do not simulate hydrogen motions and thus it cannot be used to study the methyl rotational dynamics.

6.2 Simulation details

6.2.1 Model

We perform explicit atom (EA) simulations on a system of 27 PMMA chains of 200 atoms with 100% syndiotactic sequences, and thus the simulated PMMA has a molecular weight of 1316 g/mol. We run the simulations under conditions of constant volume and temperature (NVT ensemble). A series of temperatures are considered: 400, 420, 450, 470, 500, 520, 550 and 600 K, with 500 K first simulated and other temperatures reached by cooling or heating in stages. These temperatures are all above the glass transition temperature of PMMA (373 K), as determined by DSC measurements on a low molecular weight PMMA sample (see experimental details). The OPLS (Optimized Potential for Liquid Simulations) force field (Price et al., 2001; Kahn and Bruice, 2002) as detailed in Table 6.1 is adopted. The cut-off distance for the nonbonded interactions is 8 Å.

The simulation box size is determined to match the PMMA density (Wunderlich, 1989). The corresponding densities at different temperatures are illustrated in Table 6.2.

To generate initial configurations for our EA simulations, we begin with equilibrated united atom (UA) coordinates from prior runs. Hydrogen atoms are inserted on the equilibrated carbon positions as described in Section 2.7.

Table 6.1 EA model Parameters.

Nonbonded interaction	$u^{nb}(r_{ij}) = 4\varepsilon\left[\left(\frac{\sigma}{r}\right)^{12} - \left(\frac{\sigma}{r}\right)^{6}\right] + \frac{1}{4\pi\varepsilon_0}\frac{q_i q_j}{r_{ij}}$			
	Mixing rules	$\sigma_{ij} = \sqrt{\sigma_i \sigma_j}$	$\varepsilon_{ij} = \sqrt{\varepsilon_i \varepsilon_j}$	
	atom	σ_i (Å)	ε_i (kcal/mol)	q_i (e.c.)
C3	C in CH_3 group connected to main chain	3.52	0.067	−0.135
C2	C in CH_2 group	3.52	0.067	−0.09
C	C in the main chain	3.20	0.051	0.00
CD	C connect to O by double bond	3.75	0.105	0.51
OD	O connected to C by double bond	2.96	0.210	−0.43
O	O in ester group	3.00	0.170	−0.33
CO	C in CH_3 group connected to ester O	3.50	0.066	0.16
H	H in alkane CH_3 or CH_2 groups	2.50	0.030	0.045
HO	H in ester OCH_3 group	2.42	0.015	0.030

Bonds	$u^{bond}(r_{ij}) = k_{bond}(r_{ij} - r_{ij}^0)^2$	
	k_{bond} (kcal/mol/Å^2)	r_{ij}^0 (Å)
C3-C	368	1.539
C2-C	300	1.549
CD-C	326	1.517
CD-OD	968	1.209
CD-O	471	1.360
CO-O	342	1.446
CT*-HT[#]	331	1.09
CO-HO	331	1.09

* CT includes C3 and C2; HT includes H and HO

Bends	$u^{bend}(\theta_{ijk}) = k_{bend}(\theta_{ijk} - \theta^0_{ijk})^2$	
	k_{bend} (kcal/mol/rad^2)	θ^0_{ijk} (degrees)
C-C2-C	89.5	113.3
CT-C-CT	87.9	109.47
CT-C-CD	87.9	109.47
C-CD-O	74.5	111.4
C-CD-OD	63.3	125.6
OD-CD-O	126.5	123.0
CD-O-CO	84.8	116.4
H-CT-C	35.0	109.5
H-CT-H	35.0	109.5
HO-CO-HO	35.0	109.5
HO-CO-O	56.0	110.1

Inversion	$u^{inversion}(\theta_{ijk}) = K_1(\theta_{ijk} - \theta_0) + K_2(\theta_{ijk} - \theta_0)^2$		
	θ_0 (degrees)	K_1 (kcal/mol/rad)	K_2 (kcal/mol/rad^2)
CD	360	-60.0	30.0

Torsions (kcal/mol)	$u^{torsion}(\phi_{ijkl}) = V_1(1+\cos(\phi_{ijkl})) + V_2(1-\cos(2\phi_{ijkl})) + V_3(1+\cos(3\phi_{ijkl})) + V_4(1-\cos(4\phi_{ijkl}))$			
	V_1	V_2	V_3	V_4
CT-C-C2-C	0.27792	0.00000	0.00000	−0.27792
CD-C-C2-C	0.27792	0.00000	0.00000	−0.27792
CT-C-CD-O	0.80784	0.00000	0.00000	−0.80784
CT-C-CD-OD	2.60000	0.05000	−2.55000	0.00000
C-O-C-C	2.02000	−1.00000	−0.70000	−0.32000

Table 6.2 Densities for PMMA at different temperatures.

T (K)	Density (g/cm^3)
400	1.13033
420	1.11741
450	1.09830
470	1.08574
500	1.06717
520	1.05497
550	1.03693
600	1.00754

6.2.2 Equilibration

The EA configuration prepared as described above is further equilibrated for at least 4 ns before collecting data, followed by production runs of 6 ns. This equilibration time is selected such that the atoms have moved a distance comparable to their chain dimensions. No shifts in structural or dynamic properties are evident as illustrated by the self intermediate scattering function *S(q,t)* in Fig. 6.2, calculated over three 2 ns blocks following the proposed equilibration time of 4 ns. These results suggest that the equilibration time is sufficient.

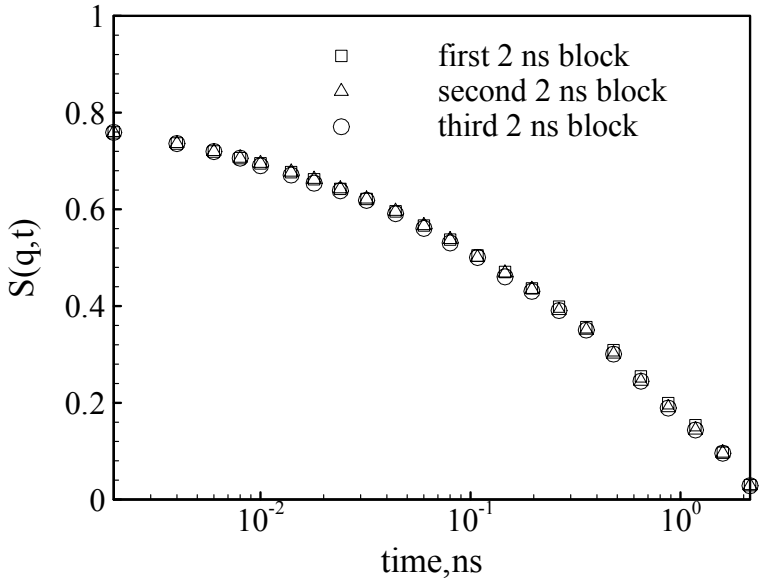

Fig. 6.2 A representative self-intermediate scattering function calculated over 2 ns blocks to illustrate the lack of drift in dynamic properties at q = 0.8 Å^{-1} and T = 500 K. (Chen et al., 2006b)

6.3 Experimental details

To validate the chosen force field, both structural and dynamic neutron measurements are used in this chapter. The structural measurements were performed on a sample of 80% syndiotactic sequences and a molecular weight of 375 000 g/mol. They are described by Farago et al. (2005). Two quasielastic neutron scattering measurements to assess dynamics are discussed below. These measurements were performed at the NIST Center for Neutron Research in Gaithersburg, MD.

6.3.1 High-flux backscattering spectrometer [HFBS] (Meyer et al., 2003)

In this spectrometer, neutrons of incident wavelength 6.271 Å (E_0 = 2.08 meV) are Doppler shifted to achieve a range of incident energies (± 20 μeV) about this nominal value. The neutrons are scattered by the sample, after which only those neutrons with final energy of 2.08 meV are detected. The dynamic range (energy transfer) of ± 20 μeV sets the shortest time available to the instrument. The instrumental resolution (full width at half-maximum), which sets the longest time, is dependent on the size of the Doppler shift and equal to 0.87 μeV for ± 20 μeV. For data reduction purposes, this resolution was measured with a vanadium sample at 295 K. The pressed polymer sample was held in a cylindrical aluminum can mounted on a closed cycle refrigerator unit. The thickness of the sample was around 0.1 mm, chosen to achieve 90% neutron transmission and minimize multiple scattering. The PMMA was purchased from Polymer Standards Service and has a molecular weight of 463 000 g/mol and 76% syndiotactic sequences.

6.3.2 Disk chopper time-of-flight spectrometer [DCS] (Copley and Cook, 2003)

The Disk chopper spectrometer uses a fixed incident wavelength, and energies of scattered neutrons are resolved by their flight times. The spectrometer was operated at an incident wavelength of 4.2 Å and at a resolution of 80 μeV. The instrumental resolution was measured using a vanadium sample at 295 K with the same instrument configuration. The measured QENS spectra collected over 6 hr periods were corrected for detector efficiencies using software developed at NIST. The scattering from the empty aluminum can and from the background were subtracted and the data were binned into q-groups in

the range 0.60 - 2.60 $Å^{-1}$. As with HFBS, the sample was annular in shape and held in a thin-walled aluminum can mounted onto a closed-cycle refrigerator, and of thickness of 0.1 mm to minimize multiple scattering. Two hydrogenated PMMA samples were used: the one described for HFBS [463 000 g/mol and 76% syndiotactic], and one closer to the simulated molecular weight [3500 g/mol], with the same percentage of syndiotactic sequences. The glass transition temperatures measured by DSC are 397 and 373 K, respectively.

Both HFBS and DCS experiments are performed at 500 K and measure the scattering intensity as a function of energy and momentum transfers, which sets the time and spatial scales, respectively. The momentum transfer is related to spatial scale by $q = 2\pi / r$ and the energy transfer to time by $t = h / \Delta E$. In order to combine the neutron scattering data from DCS and HFBS and compare these data to simulation results, the scattering functions were Fourier transformed to the time domain as discussed in Section 3.4.

The contribution of a single scattering event to the total scattering depends on the scattering cross sections of the atoms involved; both incoherent [self-motion] and coherent [relative motion] cross sections must be considered. Incoherent scattering reflects correlations between the same atom at different times, while coherent scattering reflects relative positions of atomic pairs. In the static case (diffraction experiment), the sample must be mostly deuterated and it reveals the corresponding sum of partial static structure factors. As the incoherent cross section of the proton is substantially larger than all others, the QENS experiments are performed on hydrogenated samples for which the incoherent scattering from hydrogen represents 93% of the total. The QENS results

reported here thus represent the self motion of protons. Further, in the comparisons of simulation to QENS experimental experiments, we neglect coherent contributions when computing dynamic observables from simulation coordinates.

6.4 Validation of the simulation model

To check the performance of the OPLS force field, we compare the static structure factor *S(q)* and the self-intermediate scattering function *S(q,t)* obtained from the simulation to available neutron scattering measurements (Farago et al., 2005) and described above.

We calculate the static structure factor *S(q)* assuming an isotropic sample using Eqs. (2.38) and (2.39). Figure 6.3 compares the static structure factor of PMMA calculated from simulation at 470, 500 and 600 K to neutron diffraction experiments at room temperature (Farago et al., 2005). Note that the experimental data have been renormalized to match with the simulation data at high q. The sharp peaks at $q = 2.7$ Å^{-1} and $q = 3.1$ Å^{-1} in the experimental data are due to the diffraction of the aluminum sample holder. In the investigated q range all data sets show three peaks. The first [lowest q] peak shifts to smaller q values and becomes more intense with increasing temperature, while the second and the third peaks are insensitive to temperature. These results suggest that the first peak represents intermolecular correlations while the second and third peaks reflect intramolecular packing. The height and location of the intermolecular peak obtained from the simulation depends strongly enough on temperature that the disagreement between experiment [300 K] and simulation [lowest temperature 470 K]

could be attributed to temperature dependence. Differences in the second and third peaks reflect a different intramolecular distribution (bond and torsional angles), most likely due to the sequence distribution, which is 100% syndiotactic for the simulations and 80% syndiotactic for the experimental sample.

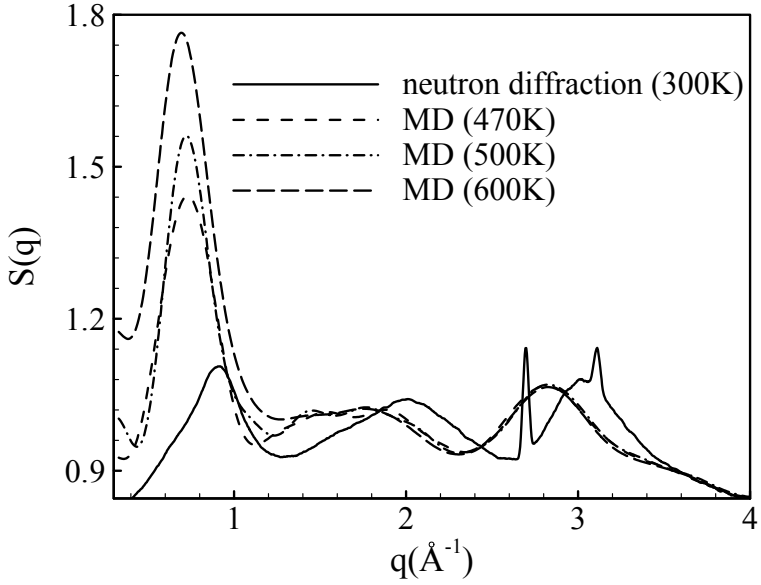

Fig. 6.3 Comparison of the static structure factor of syndiotactic PMMA calculated from simulations at temperatures of 470, 500 and 600 K with neutron diffraction experiments (Chen et al., 2006b).

The self-intermediate structure factor *S(q,t)* describes the mobility of atoms in the system, which is calculated through Eq. (2.43). To compare with DCS and HFBS experiments in which the signal is dominated by hydrogen atoms, we include only hydrogen atoms in the calculation of *S(q,t)*. Plotted in Fig. 6.4 is the *S(q,t)* from simulation and DCS and HFBS experiments at two q values (0.9 $Å^{-1}$ and 1.5 $Å^{-1}$) at 500 K. For the experimental data, a fit line is also given to estimate the decay in the time gap

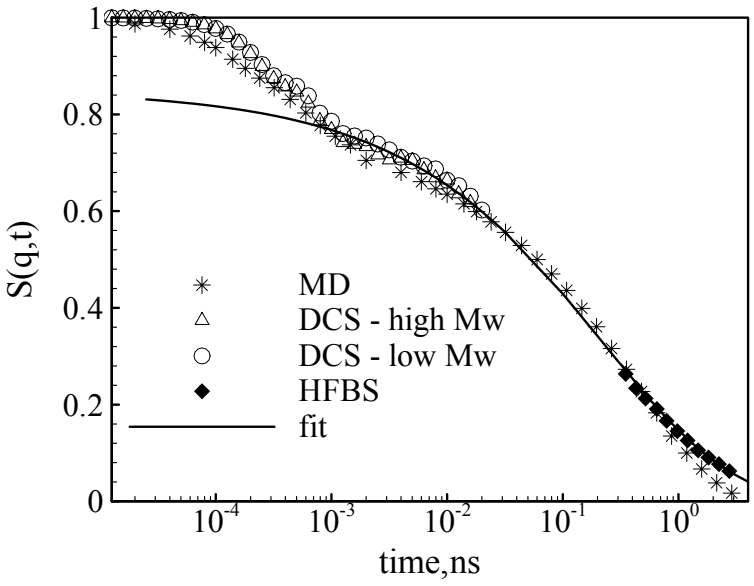

(a)

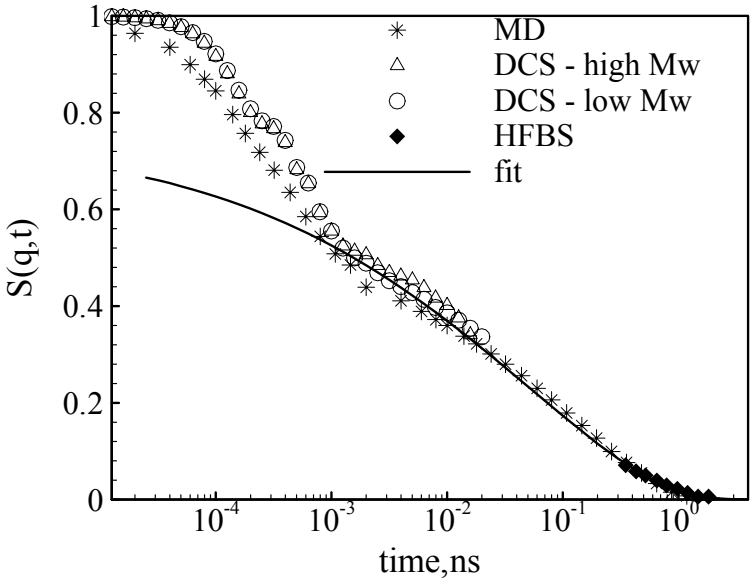

(b)

Fig. 6.4 Comparison of the self-intermediate structure factors of PMMA from simulations with DCS and HFBS measurements at 500 K and two q values: (a) q = 0.9 Å^{-1}; (b) q =1.5 Å^{-1}. (Chen et al., 2006b)

between the two instruments. Two things should be noted: the simulations are in reasonable agreement with experiment and different molecular weight samples yield almost identical DCS results. This indicates that molecular weight has little effect on the local dynamics of PMMA, and that the simulation model provides fair description of dynamics of real PMMA samples. The fits indicated in this figure are described below.

6.5 Local dynamics

Above we provided evidence that the simulation model we adopted is able to capture both structural and dynamic properties of PMMA. We now use this model to analyze and separate the local dynamics of PMMA at high temperatures: ester and α-methyl group rotations, rotation of the entire ester side group and main chain motion. Before going into the details of these motions, it should be noted that in this paper we always calculate neutron observables: the local dynamics are represented by the self-intermediate scattering function calculated through Eq. (2.44) and in our calculations only hydrogen motion is included. To isolate rotation around a specific bond, translation motion of the terminal atom of that bond must be removed. We thus calculate *S(q,t)* using Eq. (2.44) but "virtually fixing" the terminal position of the rotating group. Virtually fixing refers to removing contributions from translational motion by calculating hydrogen positions relative to the position of the appropriate carbon atom. As examples, in ester methyl group rotation the position of C_2 [in Fig. 6.1] is fixed, whereas for rotation of the entire ester side group, the position of C [in Fig. 6.1] is fixed. Clearly, these

carbon atoms do move throughout the simulation: their position is rendered fixed by calculating the hydrogen positions relative to the position of the appropriate carbon atom.

6.5.1 α- and ester-methyl group rotation

As discussed in the Introduction, it is challenging to use QENS to investigate ester CH_3 group rotation at high temperatures; even with selective deuteration, the position of atom C will translate such that rotation cannot be isolated. The resulting motion would be fit using a combination of translational and rotational models, which require assigning a large number of fit parameters from a small decay. Although experimental reports of ester CH_3 rotation are available in the temperature range of 80 - 200 K (Arrighi et al., 1995), little information is available for α-methyl group rotation. Genix et al. (2005) provide some simulation data for α- and ester methyl group rotation, but only at 400 K, which is close to *Tg* of PMMA. We separate both rotations from other motions, and thus provide data for both methyl rotations at high temperatures. As explained above we isolate rotation by fixing the terminal position of the rotating group, the dynamics of methyl group rotation are thus calculated from Eq. (2.44) by taking the relative distance between hydrogen atoms and the carbon atom positions they are bonded to. Figure 6.5 shows the rotational *S(q,t)* for α- and ester CH_3 groups at two *q* values. It can be seen from the graphs that two processes contribute. The short time (< 0.3 ps) process, which is more prominent for the ester methyl, results from internal vibrations within molecules, and is followed by decay due to the rotation of the ester methyl group. At long times, *S(q,t)* decays to an almost constant value for both methyl group rotations. The plateau in

S(q,t) indicates the presence of an elastic incoherent structure factor [EISF]. Physically this indicates motion over a restricted spatial area, and the *q* dependence of the EISF characterizes the geometry of that spatial area. In the case of CH_3 rotation, a 3-fold rotation (Pérez Aparicio et al., 2006; Saelee et al., 2000) is often used: the protons jump between three equivalent sites. This results in a temperature independent EISF of the form (Bée, 1998):

$$EISF = \frac{1}{3}\left[1 + 2\frac{\sin(qr_{H-H})}{qr_{H-H}}\right] \tag{6.1}$$

where $r_{H\text{-}H} = 1.78$ Å is the H-H distance.

Figure 6.6 compares the EISF calculated from 3-fold, as well as 4-fold and 6-fold rotation models and that obtained from the plateau value in the simulations. As can be seen from the figure, the EISF obtained from the simulation is temperature independent and consistent with the prediction from all three rotational models at *q* values lower than 1.8 $Å^{-1}$. At larger *q*, the simulated data is more consistent with 4- and 6-fold rotation models. QENS Experimental data on the methyl group rotation of polyisoprene appear to be consistent with 3-fold rotation (Zorn et al., 2002), but they are only available for *q* values lower than 2 $Å^{-1}$ due to instrumental limitations. Moreno and colleagues (2001a; 2001b) found that a 6-fold correction to the 3-fold potential was required to describe rotation of the methyl group in PMMA and in glassy toluene.

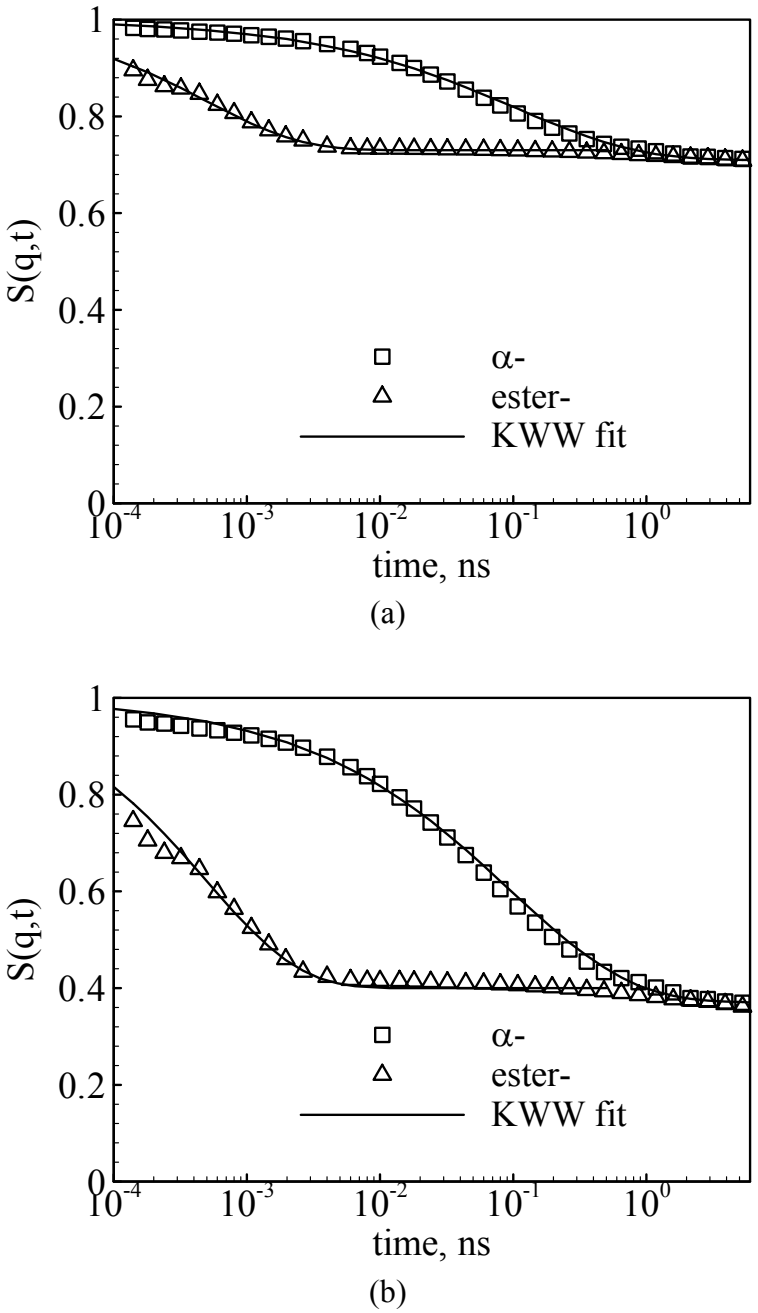

Fig. 6.5 The rotational *S(q,t)* for α- and ester CH_3 groups at 500 K and two q values: (a) $q = 0.9$ Å^{-1}; (b) $q = 1.5$ Å^{-1}. The KWW fits are for the long-time decay ($t > 0.3$ ps). (Chen et al., 2006b)

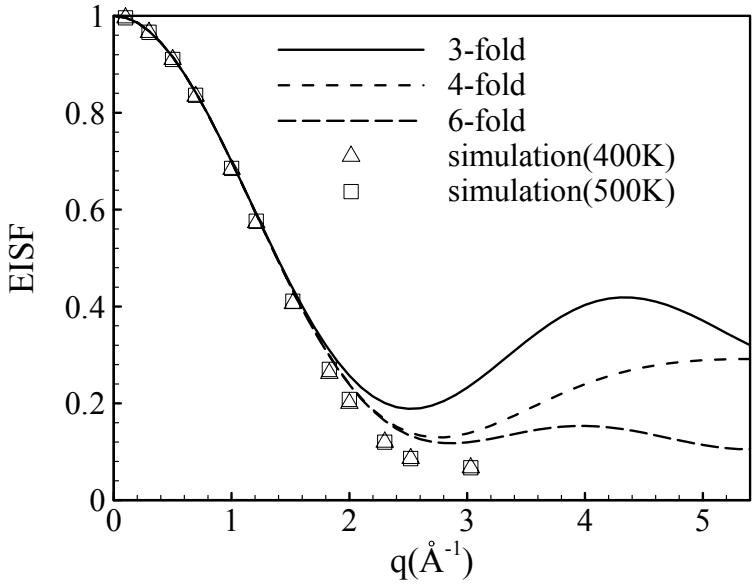

Fig. 6.6 q dependence of the simulated EISF compared to theoretical predictions for CH_3 rotation in 3-fold, 4-fold and 6-fold models. (Chen et al., 2006b)

In any of the rotational jump models, it is presumed that the rotating atoms jump between the designated number of sites, with the residence time in each site much larger than the time required to change from site to site. In addition, rotational models neglect librational motion within each site. This requirement will clearly be satisfied at low temperatures. It is possible that at high temperatures, the residence times will become so small that the total amount of time a proton spends in rotational sites is roughly equal to the time it spends jumping from one site to another. This could result in an EISF that does not reflect the true nature of the rotation. To address this issue, we have calculated the torsional angle of a proton in each type of methyl group at 500 K as a function of time. The results are presented in Fig. 6.7, where it is apparent that the torsional angle of the α proton [H-C_3-C_1-C] undergoes librational motion in each of three different sites [-120, 0

& 120 degrees], punctuated by quick jumps between sites, as expected. The torsional angle of the ester proton [H-C_2-O-C] also occupies three sites, but as the jumps between them are far more frequent, the proton spends more time transitioning between sites. As both types of methyl groups present the same EISF, it does not appear likely that more frequent transitions lead to deviations from 3-fold rotation. On the other hand, both methyl groups execute librational motions approximately ± 30 degrees from the jump site. This would have the effect of smearing out the apparent shape of the motion from a triangle [3-fold rotation] to a hexagon [6-fold rotation], as illustrated in Fig. 6.8. The reasonable agreement between our simulation data and the predicted EISF for CH_3 rotation validates both the utility of the simulation and our method for isolating rotational motion.

In order to perform a quantitative analysis of CH_3 rotation, the portion of the decay curve attributed to this motion is fit with:

$$S(q,t) = A\left\{ EISF + (1 - EISF)\exp\left[-(\frac{t}{\tau_{KWW}})^{\beta} \right] \right\} \tag{6.2}$$

where A is the prefactor describing the first decay, τ_{KWW} the relaxation time, β the distribution of relaxation times, and the EISF is taken from the long time plateau of the *S(q,t)* decay curve. All rotational times reported here are the τ_{KWW} resulting directly from fitting with Eq. (6.2). As discussed in Arrighi et al. (1995), the stretched exponential function accounts for the existence of a distribution of rotational frequencies instead of a single rotational frequency, and provides more reasonable results than a single exponential when applied to QENS measurements.

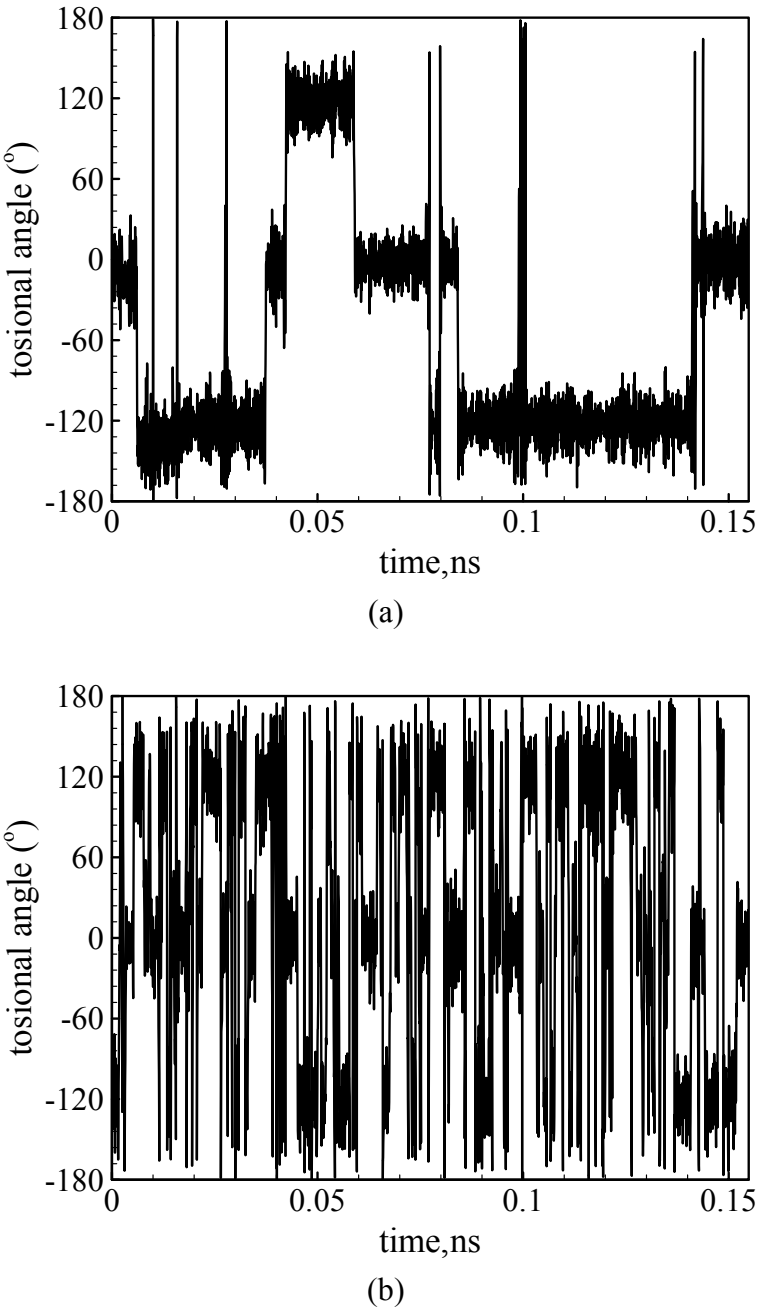

Fig. 6.7 Dihedral angle as a function of time with the time interval of 0.04 ps for: (a) α-methyl group; (b) ester methyl group at 500 K. (Chen et al., 2006b)

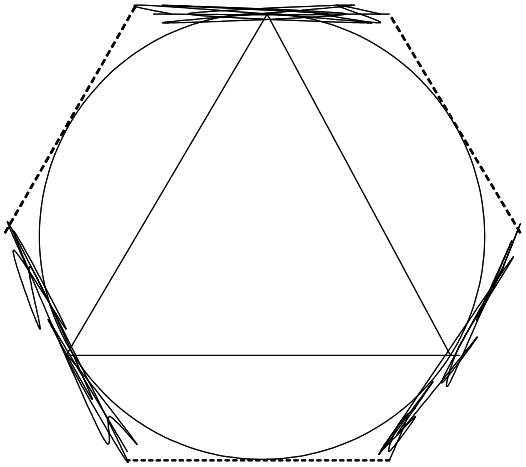

Fig. 6.8 A schematic of a methyl rotation between three sites. Dashed lines represent proton jump between different energy levels. Solid lines represent librational motion. The triangle indicates an ideal 3-fold jump and the hexagon represents an approximated 6-fold jump. (Chen et al., 2006b)

Times for rotation are expected to be q independent with an Arrhenius temperature dependence. As seen in Fig. 6.9 (a) the relaxation times fit with Eq. (6.2) for both α- and ester methyl group rotations at 500 K verify the independence of spatial scale, with the ester rotation much faster than the α rotation as is known experimentally. Figure 6.9 (b) shows that β values for both methyl rotations are not sensitive to q.

The Arrhenius temperature dependence of rotation times is illustrated in Fig. 6.10. We also include neutron (Arrighi et al., 1995; Higgins and Benoît, 1994) and NMR data (Higgins and Benoît, 1994) for comparison. As can be seen from the graph, both rotations are Arrhenius in temperature. The activation energy calculated from Eq. (2.48) for α-methyl group rotation as shown in Fig. 6.10 (a) is 36.6 kJ/mol, close to the value of 34 kJ/mol derived by Higgins and Benoît (1994) and the value of 32 kJ/mol reported by

Allen et al. (1974). As is clear from the figure, the α-methyl rotational behavior at high temperature is obviously a continuation of that from NMR measurements at low temperatures (Higgins and Benoît, 1994), and its rotational times are also consistent with those from neutron scattering (Higgins and Benoît, 1994). For ester methyl group rotation as shown in Fig. 6.10 (b), the activation energy is 8.9 kJ/mol, which is close to 10 kJ/mol reported from NMR experiments (Heijboer et al., 1987) although further from the 5.4 kJ/mol obtained from QENS measurements (Arrighi et al., 1995) and 5.9 kJ/mol obtained from inelastic neutron measurements (Moreno et al., 2001a) at low temperatures. MD and NS (Arrighi et al., 1995) relaxation times in Fig. 6.10 (c) for the ester CH_3 rotation fall on a smooth curve, and a change in activation energy seems hinted by the experimental data at around 160 K.

Plotted in Fig. 6.10 (d) are the stretching parameters for both ester and α-methyl group rotation as a function of temperature. In the case of the ester group, there is little difference with temperature, while for the α-methyl, a slight increase with increasing temperature is evident. The ester methyl rotation was analyzed using a stretched exponential by Arrighi et al. (1995), and we note that the stretching parameter is observed to increase slightly and level off around 0.6 at temperatures above 200 K. This is consistent with our results.

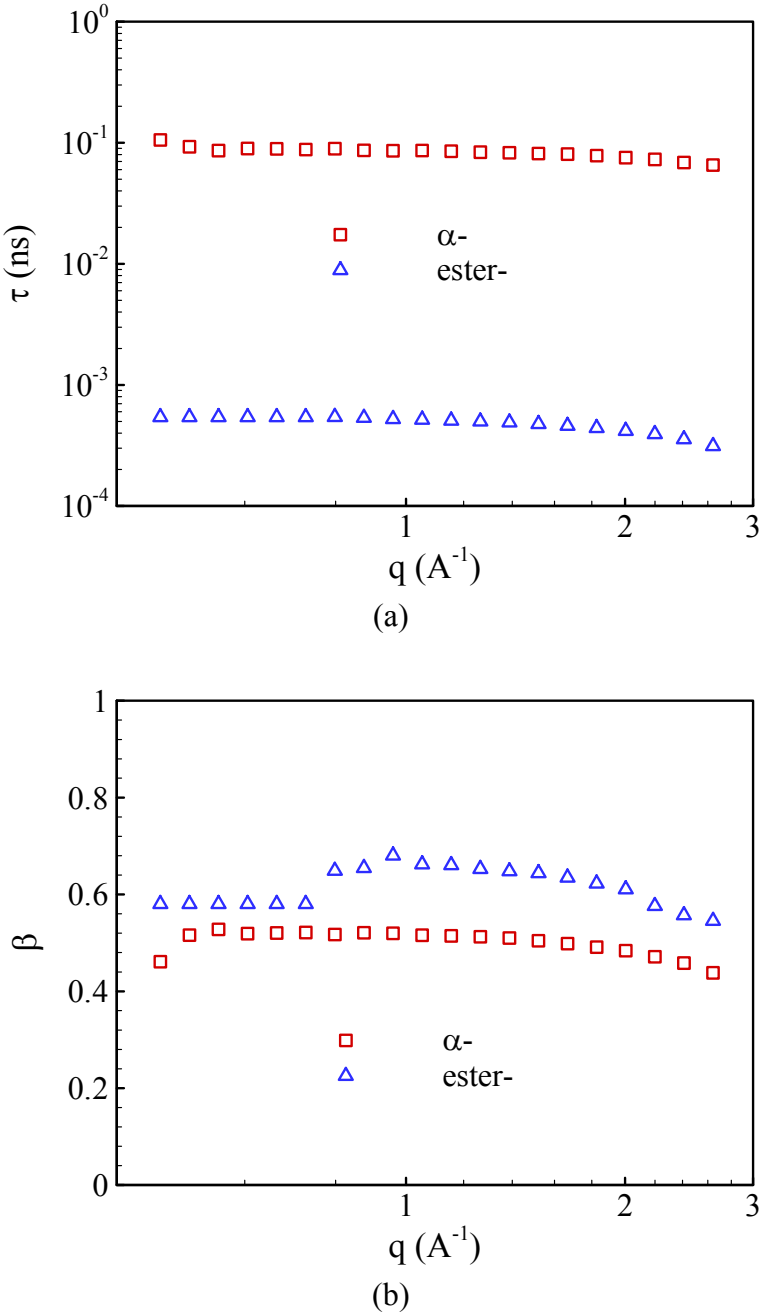

Fig. 6.9 q dependence (a) rotation times and (b) β parameter for α- and ester CH_3 groups at 500 K. (Chen et al., 2006b)

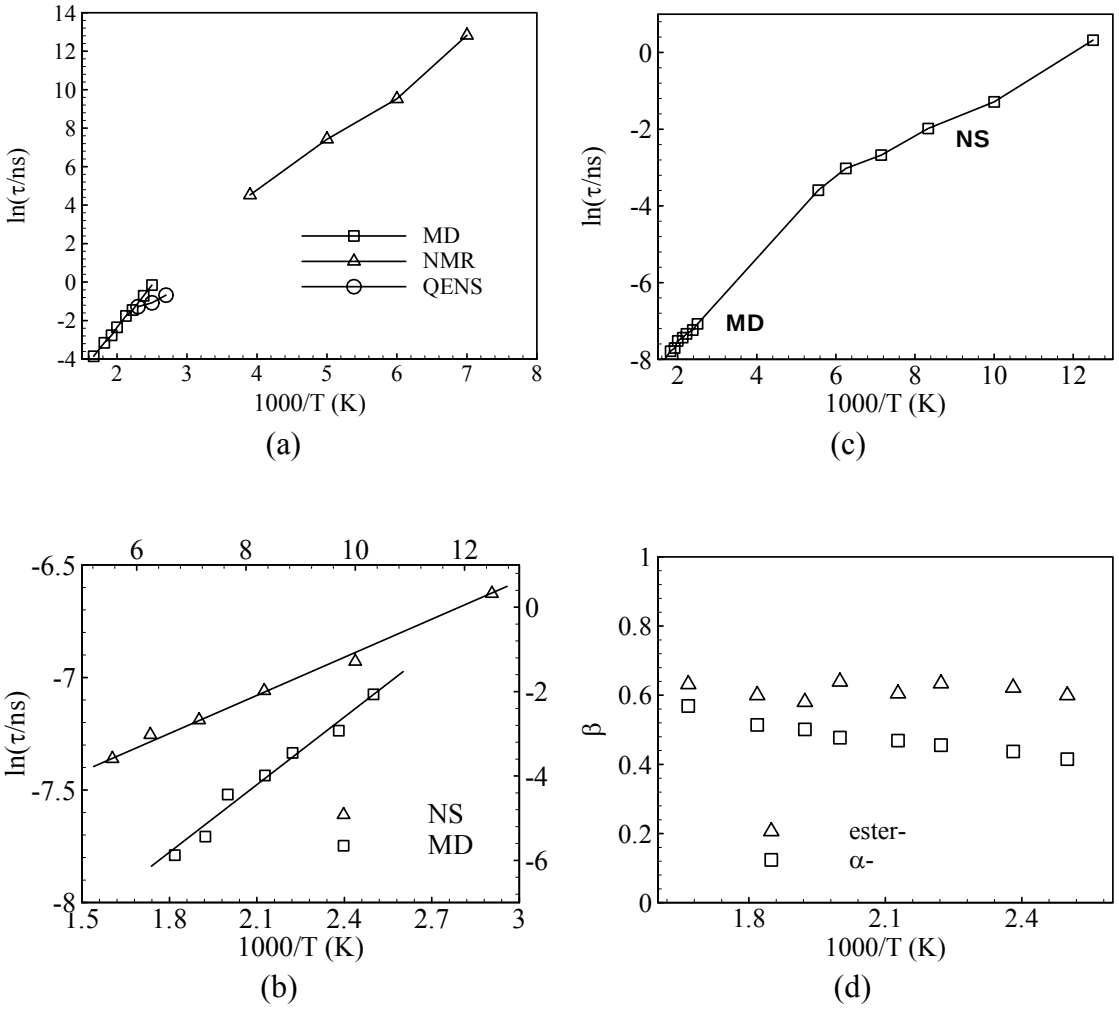

Fig. 6.10 Temperature dependence of relaxation times and the β parameter for CH_3 group rotations at q = 1.5 Å^{-1}: (a) α-methyl rotation, and its comparison with NMR and QENS results (Higgins and Benoît, 1996); (b) ester where the MD and neutron data (Arrighi et al., 1995) are plotted on separate scales; (c) ester, with neutron and MD data on a common scale; (d) β parameter for both methyl group rotations. (Chen et al., 2006b)

Our results provide relaxation times of α- and ester methyl group rotations at high temperatures. The main characteristics of methyl rotations are observed: q independent relaxation times, an EISF close to theoretical predictions, and Arrhenius temperature dependence of relaxation times. The range of our simulations is limited to temperatures well above *Tg*. Over the investigated temperature range, the activation energy for the ester methyl rotation is higher than that obtained from neutron scattering experiments (Arrighi et al., 1995). Potential explanations apart from a change in activation energy as mentioned above is the different molecular weight or tacticity of the simulated sample. Rotation of methyl groups is very local and should not depend on molecular weight. Both rotation times and activation energies depend on tacticity. However, the barrier for rotation of isotactic PMMA is higher than that of syndiotactic PMMA (Cereghetti et al., 2004) so the higher activation energy in our simulated systems [100% syndiotactic] would be expected to be lower than the experiments [predominantly syndiotactic] (Arrighi et al., 1995).

6.5.2 Entire carboxyl group rotation

As discussed in Introduction, the β-relaxation is prominent in the dielectric spectra of PMMA, and it has been associated with hindered rotation of the $-COOCH_3$ group around the C-C bond linking it to the main chain (Schmidt-Rohr et al., 1994). By isolating this specific motion and studying the resulting spectra, we test this idea. This motion is isolated by considering the motion of the ester hydrogens relative to carbon C [see Fig. 6.1]. The *S(q,t)* for ester side group rotation is thus calculated from the positions of the three hydrogen atoms relative to this carbon atom. This calculation,

explicitly excludes rearrangement of the main chain, thereby separating the structural relaxation from carboxyl group rotation. Structural relaxation is addressed in Section C. Figure 6.11 shows the rotational *S(q,t)* for the entire ester group at 600 K and at three *q* values (0.6, 0.9 and 1.5 $Å^{-1}$). As with CH_3 group rotation, fast vibrations appear at short times. The rotation of the ester CH_3 group also contributes. A plateau in *S(q,t)*, i.e. the EISF, is again observed at longer times, however in this case its value is much smaller than for CH_3 group rotation.

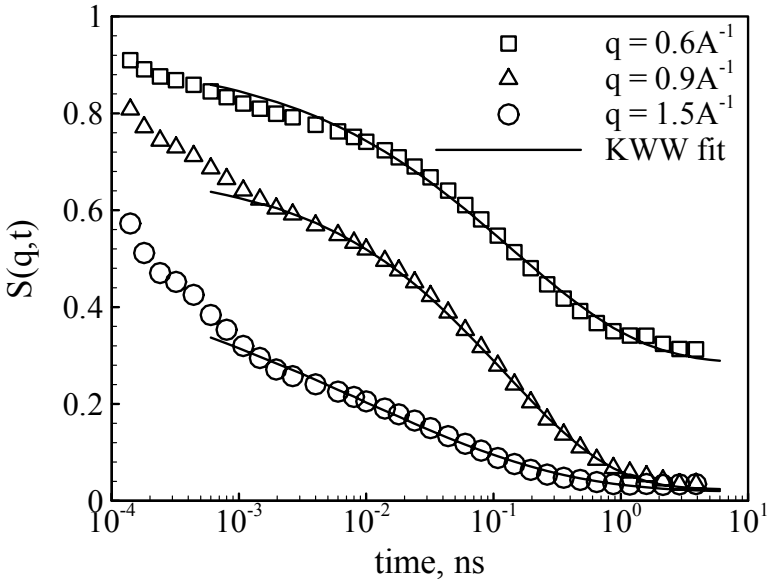

Fig. 6.11 *S(q,t)* for the rotation of ester hydrogen atoms around C-C bond connecting to the main chain at 600 K and at three *q* values. The KWW fits shown in this graph are for the long-time decay (t > 1 ps). (Chen et al., 2006b)

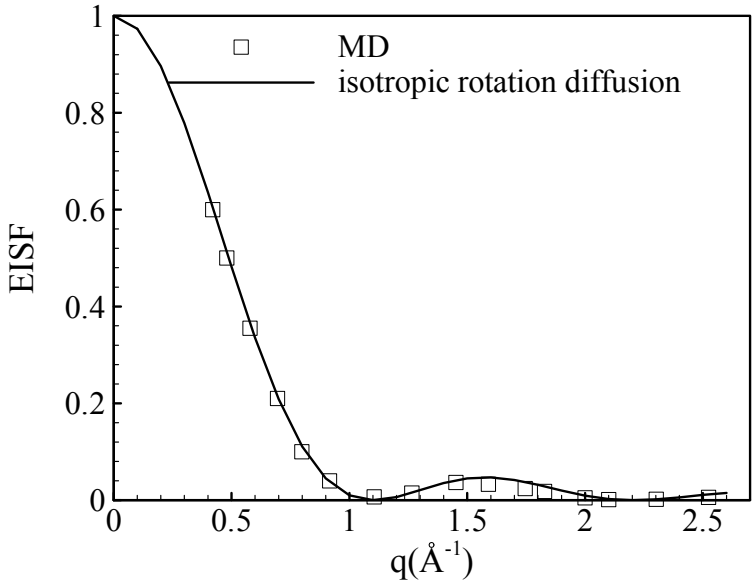

Fig. 6.12 q dependence of the simulated EISF for rotation of the entire ester group rotation at 600 K, compared to the isotropic rotational diffusion model, where $r = 2.85$ Å^{-1}. (Chen et al., 2006b)

Because the rotating protons are separated from the point of rotation by three bonds, we expect the rotation to occur not through discrete jumps, but instead in a more continuous manner. In addition, the area of rotation should be larger. To test these ideas, we fit the EISF obtained from the plateau values of *S(q,t)* to the prediction of the isotropic rotational diffusion model, in which continuous small angle rotations occur and the rotating molecule has no preferred spatial orientation (Bée, 1988).

$$EISF = \left(\frac{\sin(qr)}{qr} \right)^2 \tag{6.3}$$

In the above equation, r represents the radius of the area of rotation. As shown in Fig. 6.12, simulation data agree well with the isotropic rotational diffusion prediction with r = 2.85 Å. This suggests that ester methyl protons rotate around the C_1-C bond by randomly

moving throughout a circle of radius 2.85 Å. Both the continuous nature of the motion and the size of the circle are a result of the two intervening bonds. Intramolecular packing in PMMA causes a broad second peak in *S(q)* corresponding to length scales of approximately 3 to 4.5 Å. This likely reflects the length scales involved in packing of adjacent ester groups. Thus it is reasonable that the ester group is confined to a circle of radius slightly less than 3 Å. To test this idea, we show the pair distribution function [Fig. 6.13] between ester protons on the same chain. The peak at ~ 4 Å is consistent with the spatial extent of rotation indicated by EISF.

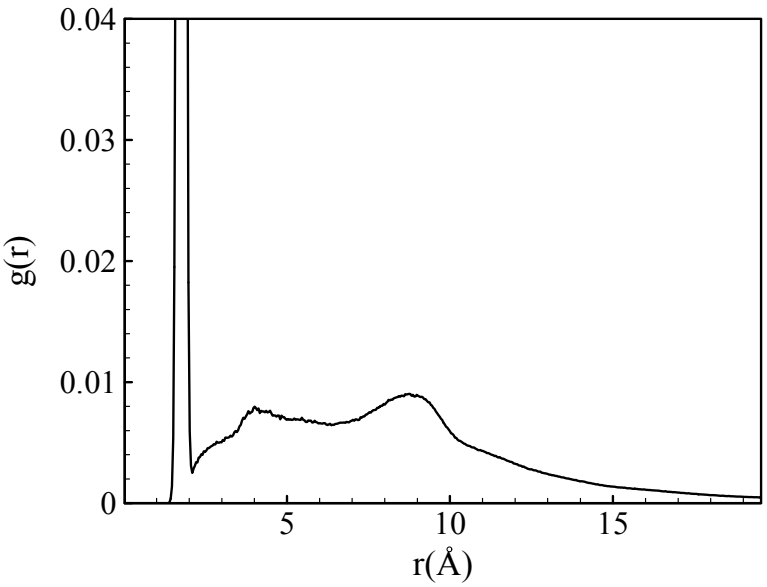

Fig. 6.13 Intramolecular pair distribution function between ester protons at 500 K. (Chen et al., 2006b)

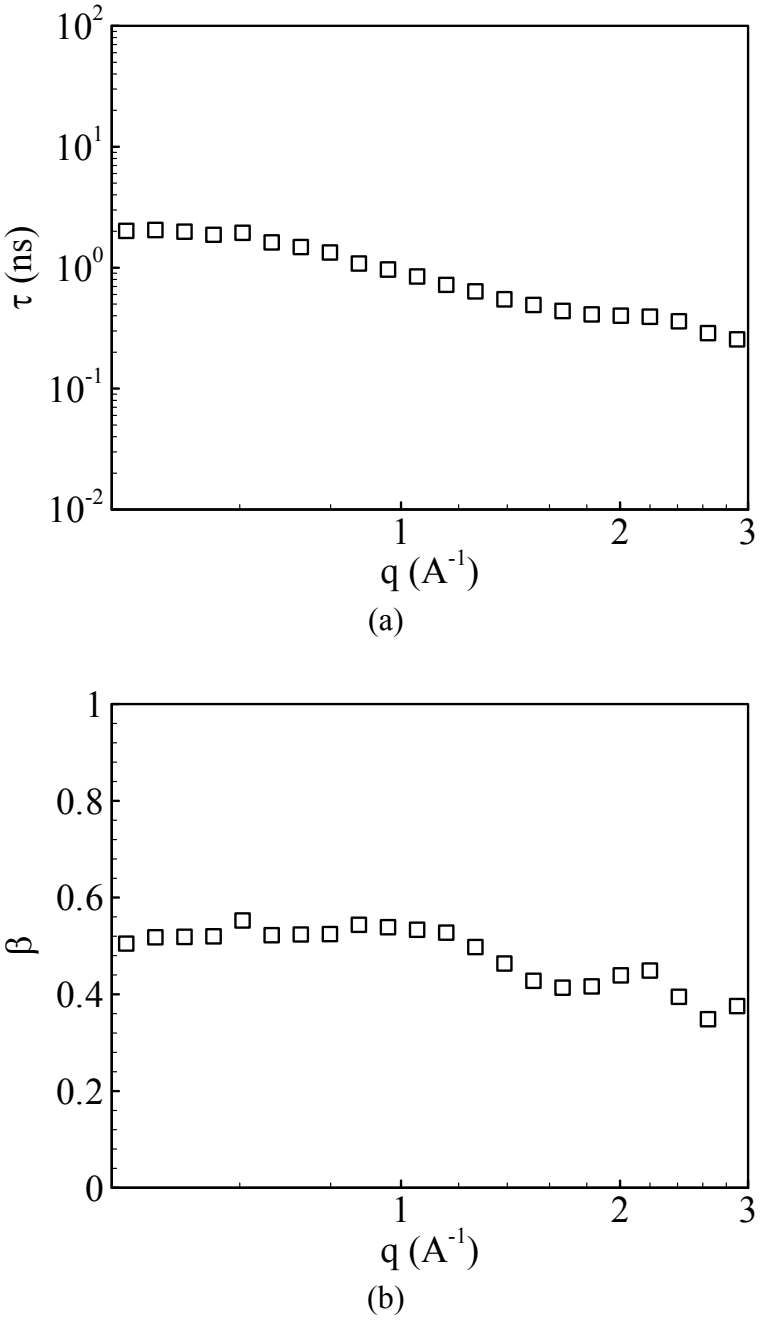

Fig. 6.14 q dependence of relaxation times and stretching exponents for rotation of the entire ester side group at 500 K. (Chen et al., 2006b)

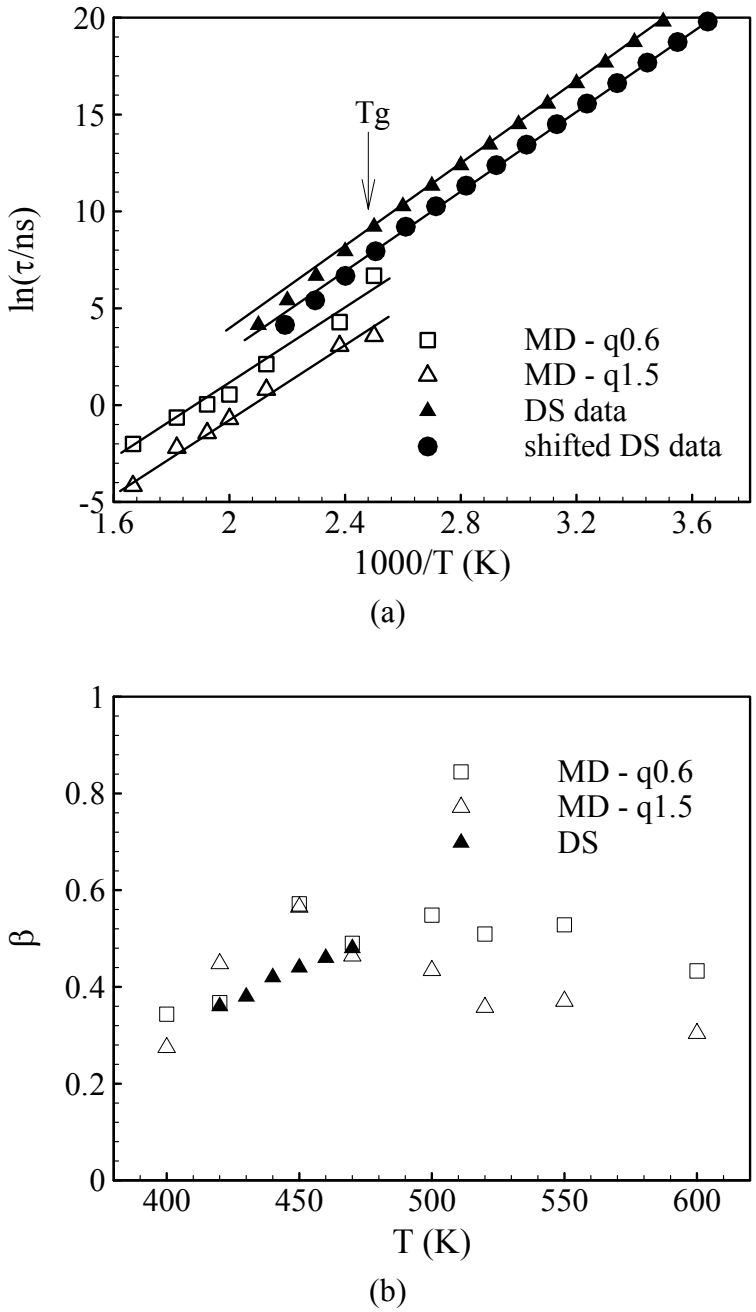

Fig. 6.15 Comparison of the temperature dependence of entire ester side group rotation behavior to DS β-relaxation: (a) τ vs. 1000/T; (b) β vs. T. (Chen et al., 2006b)

Since rotation is slower for the entire ester group, the plateau in *S(q,t)* can only be clearly ascertained within 6 ns for 600 K, and thus other temperatures are not shown. We expect that the EISF is independent of temperature, and have used the value from 600 K, along with Eq. (6.2) to fit ester group rotation at all temperatures. In Fig. 6.14 we show the spatial dependence of the relaxation times and stretching parameters obtained in the fits. The relaxation times are only weakly q dependent, as expected for rotation. The stretching parameters cluster around 0.43, consistent with dielectric measurements of the β-relaxation for which $\beta = 0.45$ at 475 K (Bergman et al., 1998).

Figure 6.15 shows the temperature dependence of relaxation times and β for the ester group rotation. In Fig. 6.15 (b), we plot the stretching parameter obtained from fits of ester side group motion with that obtained from DS data for the β-relaxation (Bergman et al., 1998) at two q values (0.6 and 1.5 $Å^{-1}$). Our results show the same trend with temperature over the range where DS data is available. The activation energy calculated using Eq. (2.48) does not depend on q and has a value of 77.4 kJ/mol, which is consistent with the 79.42 kJ/mol for the β process at temperatures below *Tg* from broad-band dielectric spectroscopy (Bergman et al., 1998).

Figure 6.15 (a) compares the relaxation times obtained from the above analysis of ester group rotation and dielectric spectroscopy measurements of the β-relaxation. It is apparent that the slopes are coincident but the values of relaxation times are not in agreement. Because the *Tg* of PMMA is molecular weight and tacticity dependent, the *Tg*s of the simulated and measured (*Mw* 550 000, *Tg* 404 K) samples differ by approximately 17 K. To test if this might have an influence, we have shifted the DS data

to account for this difference. While one would expect that the β-relaxation is a local process, independent of effects from slowing of segmental motion at *Tg*, it does appear that the actual times are more consistent with experimental data if the latter are shifted. This is consistent with the finding that ester group rotation is accompanied by main chain rearrangement (Schmidt-Rohr et al., 1994). It is interesting that even for temperatures well below *Tg*, where main chain motion should be arrested, the dielectric data must be shifted to be consistent with the high temperature simulation data where main chain motion is omitted from the calculation. In the temperature range of our simulations, the β-relaxation is merged with the α-relaxation in dielectric measurements. The merged process has an activation energy of 110 kJ/mol. For the simulation results, in this temperature range, the rotation of the ester side group appears to be a high temperature isolation of the local motion responsible for the β-relaxation, and thus its activation energy is consistent with that of the β process measured via dielectric spectroscopy at low temperatures, where its motion is not coupled with main chain reorientation. This confirms that its origin is rotation of the ester group, as has been suggested previously. Reported by Schmidt-Rohr et al. (1994), the β-relaxation is described as consisting of 180^{o} side group flips, accompanied by rotational readjustments of the main chain. These adjustments are not included in the scattering function calculated for the rotation of the ester group. However, if, as is argued by Schmidt-Rohr et al. (1994), the ester group rotation only occurs with corresponding main chain motion, then this is included implicitly in the rates because the rotation would not occur in absence of torsional rearrangement. At least with respect to the rotation of the ester protons, 180° flips [2-site

rotation] as suggested by Schmidt-Rohr et al. (1994), are not consistent with our data. As with rotation of the methyl groups, we present in Fig. 6.16 the torsional angle involving rotation of the ester oxygen around the C_1-C bond [O-C-C_1-C_3]. Although the sampling time is small compared to the residence time in each site, two sites are visited, consistent with a 180° flip. Moreover, librations within these sites lead to torsional angle variations of ± 60 degrees. As with methyl group rotation, this variation smears out the apparent site such that the shape visited by the ester oxygen more resembles a square [4-fold rotation] as shown in Fig. 6.17.

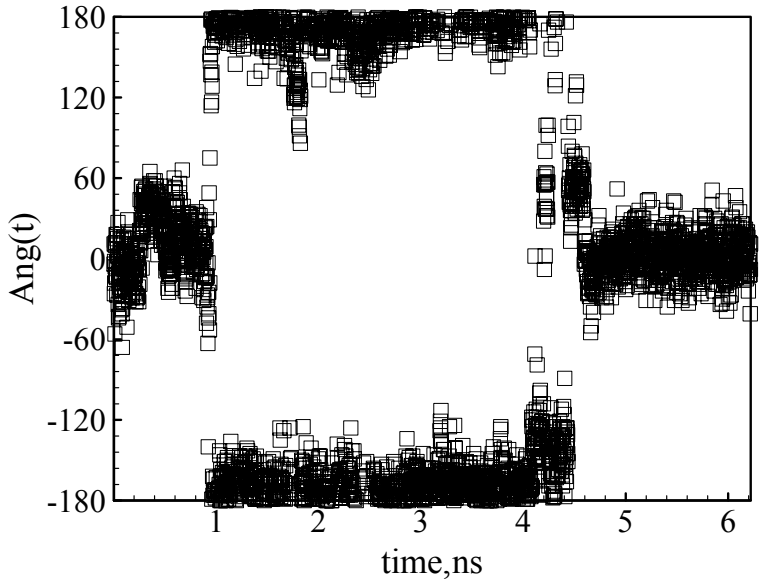

Fig. 6.16 Torsional angle involving rotation of the ester oxygen around the C-C_1 bond (C_3-C_1-C-O) as a function of time with the time interval of 2 ps at 500 K. (Chen et al., 2006b)

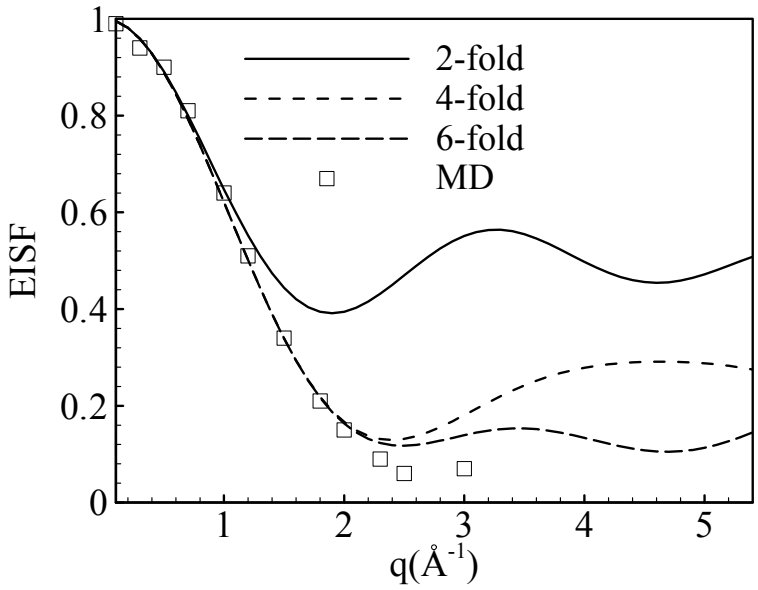

Fig. 6.17 EISF from ester oxygen rotation compared to theoretical predictions from 2-fold, 4-fold, and 6-fold models, where $r_{O\text{-}O}$ is 2.1 Å^{-1}. (Chen et al., 2006b)

6.5.3 Main chain dynamics

The α-relaxation is often associated with the chain backbone. To test this for PMMA, we investigate the main chain dynamics by including only hydrogen atoms on the main chain when computing *S(q,t)*. The resulting decay curves are shown in Fig. 6.18. As expected, main chain motion is highly temperature dependent. For the highest temperatures, *S(q,t)* decays to zero at long times for all *q* values, indicating there is no EISF as expected. We thus fit the main chain decay with Eq. (2.47). As with rotational times, all times reported for main chain relaxation are the τ_{KWW} times resulting directly from fits to Eq. (2.47). Good agreement is found between our simulation data and the DS data, as shown in Fig. 6.20. They all suggest that the α-relaxation is more strongly

temperature dependent than the β-relaxation, and that the α-relaxation is less stretched at high temperatures.

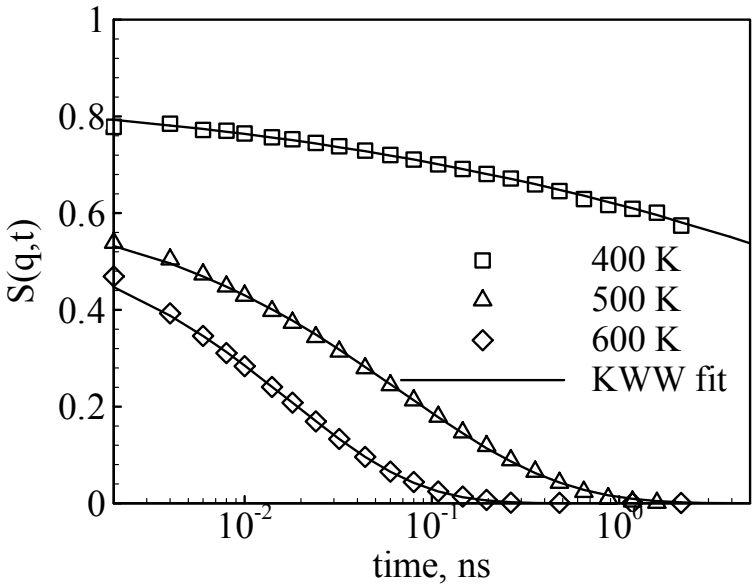

Fig. 6.18 Main chain relaxation processes at different temperatures and q = 1.5 Å^{-1}. (Chen et al., 2006b)

The q dependence of relaxation times as shown in Fig. 6.19 (a), as well as all the other temperatures, follows $\tau \propto q^{-2/\beta}$, which is often observed for the α-relaxation in polymers (Richter, 1997). Our prior neutron measurements (García Sakai et al., 2004) showed that $\tau \propto q^{-2/\beta}$ is expected at temperatures within 40 K of *Tg*. The temperature dependence of relaxation times, as shown in Fig. 6.19 (b) for two q values, is obviously non-Arrhenius. These results suggest that the motion of the chain backbone is the primary contribution to the α-relaxation in PMMA. The time scale of this motion is coincident with that of ester group rotation in the higher end of the temperature range, as

can be seen in Fig. 6.20. This is expected from the merging of α- and β-relaxations in DS. At higher spatial scales, rotation of the α-methyl also appears on the same time scales. We will return to this figure below. The stretching parameter obtained from fits of main chain motion is compared to that obtained from DS for the α-relaxation in Fig. 6.20 (c). The comparison indicates again and emphasizes the correlation between main chain motion and the α-relaxation.

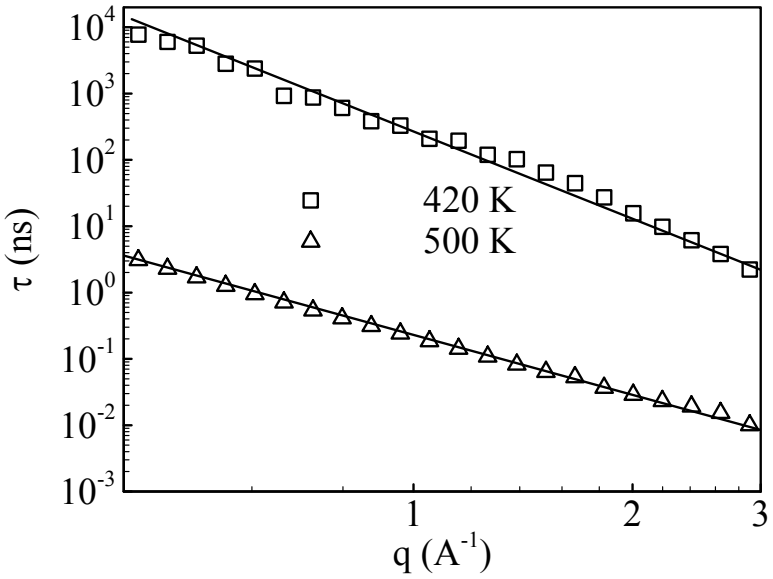

(a)

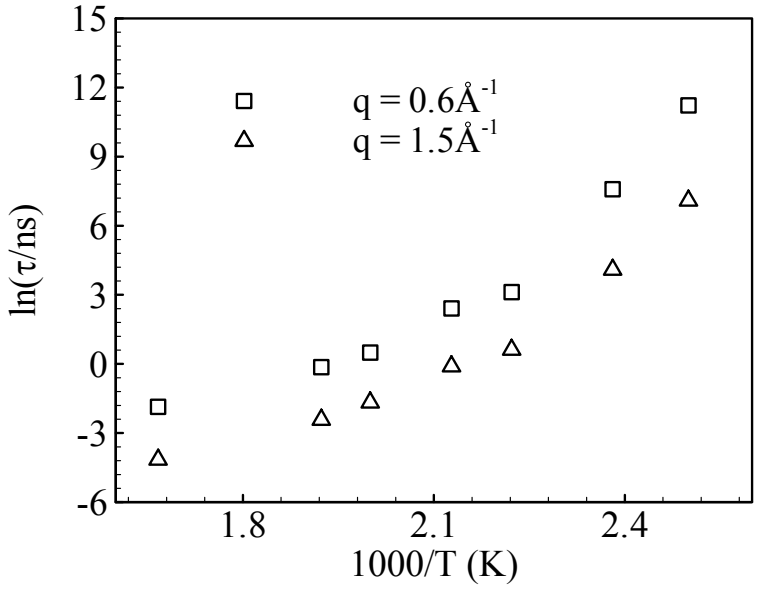

(b)

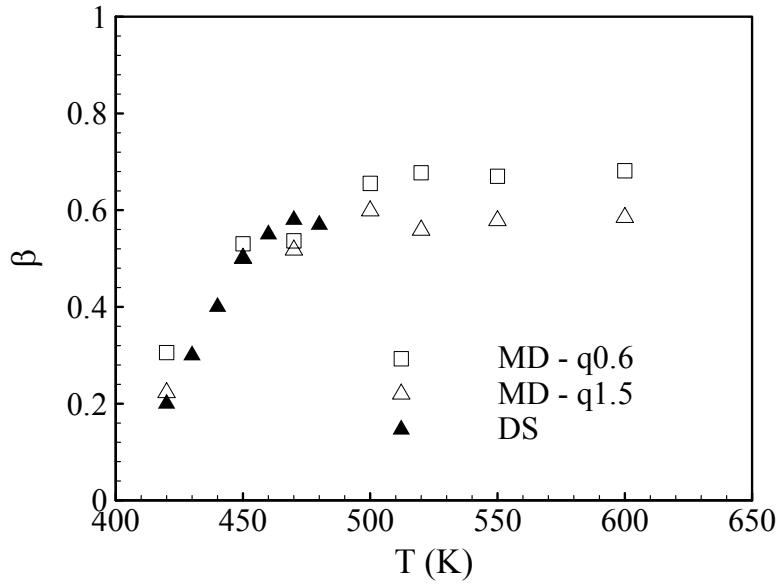

(c)

Fig. 6.19 Main chain motion dynamics: (a) q dependence of relaxation times; (b) T dependence of relaxation times; (c) T dependence of β parameter and its comparison to DS data. (Chen et al., 2006b)

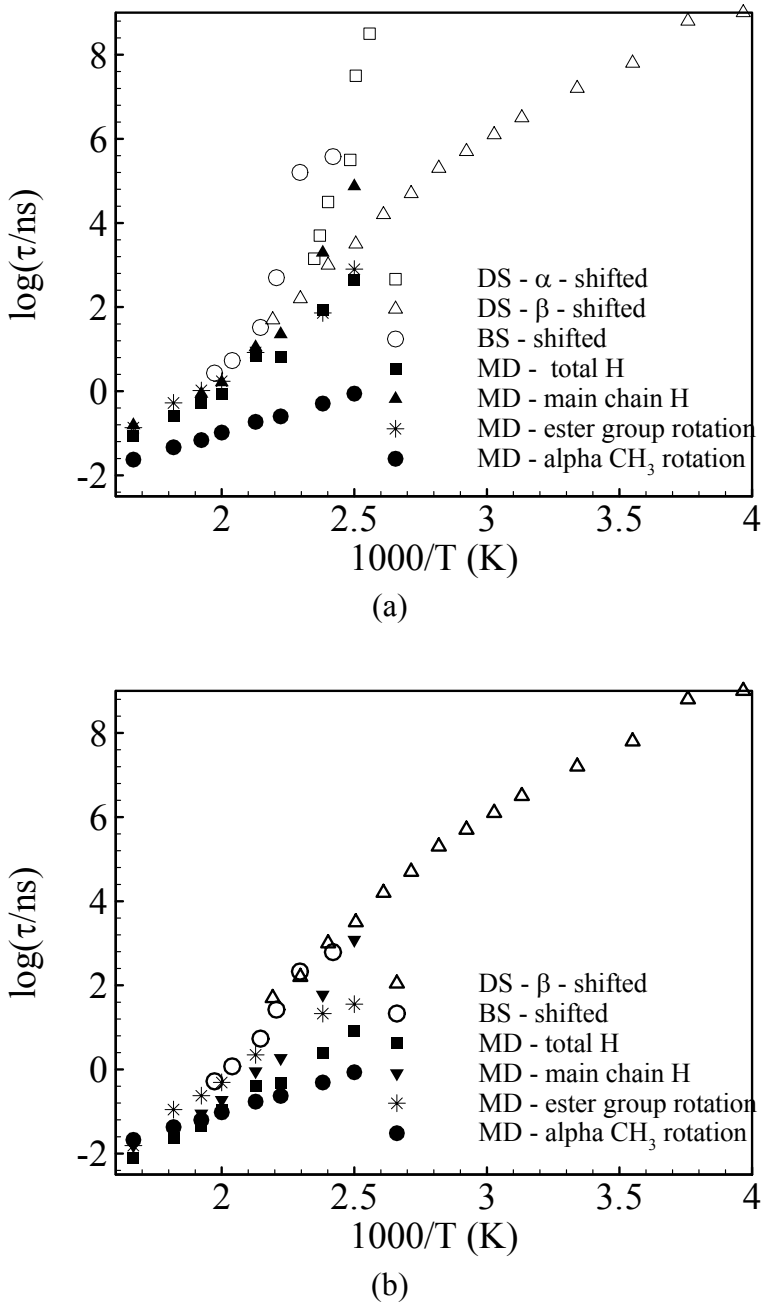

Fig. 6.20 Comparison of simulation data to dielectric (Bergman et al., 1998) and neutron (García Sakai et al., 2004) scattering results at: (a) q = 0.6 Å^{-1}; (b) q = 1.5 Å^{-1}. (Chen et al., 2006b)

6.5.4 Comparison with dielectric and backscattering measurements

In addition to considering the four motions described above on an individual basis, we have also calculated the scattering function *S(q,t)* including all hydrogens. This decay is fit with Eq. (2.47), and produces both the simulation data and the fit lines shown in Fig. 6.4. This result would compare directly to the neutron measurement (García Sakai et al., 2004). Three of the individual motions we address here have comparable time scales and should contribute to this overall decay. The overall relaxation is thus compared with ester group rotation, the main chain motion, and α-CH_3 group rotation in Fig. 6.20. Experimental data, from both QENS and DS, are also shown. The experimental data, both QENS and DS, have been shifted to account for differences in *Tg*. Figure 6.20 (a) illustrates a spatial value, q = 0.6 Å^{-1}, larger than the interchain spacing. Here the rotations do not contribute as much (the EISF is 0.88 for methyl group rotation and 0.36 for ester group rotation) and thus the α-methyl rotation time does not influence the decay of all protons to a large extent. This can be seen by comparing the times for all proton motion, main chain motion and α-methyl group rotation in Fig. 6.20 (a). Although the α-methyl rotation times are quite different, they do not contribute much to the decay calculated with all protons. This is the reason that this spatial scale shows α-relaxation character. This is also the spatial scale which most closely agrees with relaxation times from DS, and accordingly these times are also given. In Fig. 6.20 (b), we illustrate a smaller spatial scale, q = 1.5 Å^{-1}. Although DS data are more consistent with QENS at q = 0.6 Å^{-1}, we also show this data here to facilitate comparison with the β-relaxation. Here the EISF for methyl rotation is 0.4 and that for ester rotation is 0.05. As a result,

both β-relaxation [rotation of the ester side group] and rotation of the α-CH_3 group contribute more than at q = 0.6 $Å^{-1}$. Since both are Arrhenius, the overall decay appears more skewed towards the β-relaxation. This is the reason the experimental QENS data appears more consistent with the β-relaxation at large q.

6.6 Summary and conclusion

Although a variety of experiments are available to explore the dynamics of methyl group rotation, the β-relaxation and the α-relaxation in PMMA, it is difficult to retrieve specific local motions using these techniques because the response in a particular experiment includes all types of motion grouped together. This is particularly true at temperatures above *Tg*. Here we have adopted molecular dynamics simulations to isolate several motions in PMMA, which is both well studied and has several important applications due to its high transparency in visible light. We evaluate the performance of our EA model for both static and dynamic observables using neutron scattering data. The performance of this model is comparable and in agreement with neutron diffraction for static properties. The dynamics represented via QENS experiments are also in reasonable agreement. We use the model to study four different molecular motions in PMMA: main chain motion, rotation of the ester side group, and rotation of both methyl groups. Our main conclusions are summarized in the form of Arrhenius plots for the relaxation times of all four motions in Fig. 6.21. An Arrhenius temperature dependence is evident for all three rotations: the α-methyl, the ester methyl and the entire ester side group. The activation energies follow ester side > α-methyl > ester methyl, consistent with available

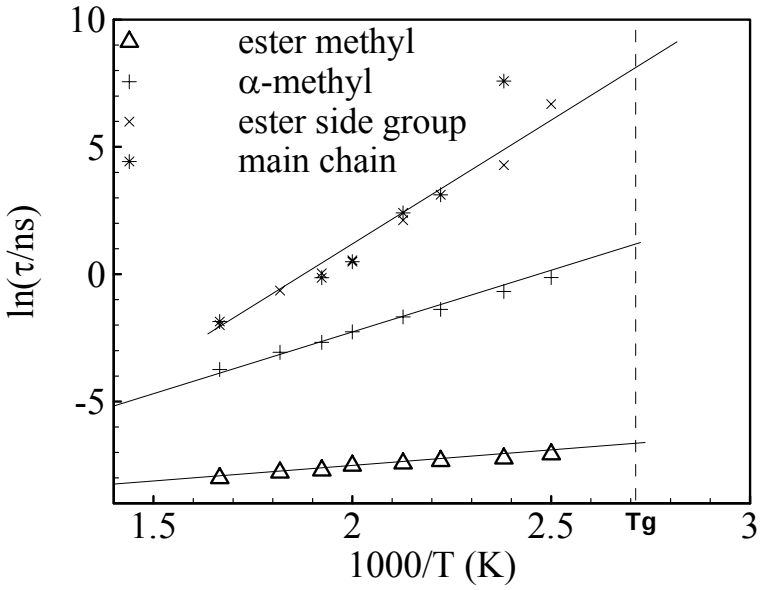

(a)

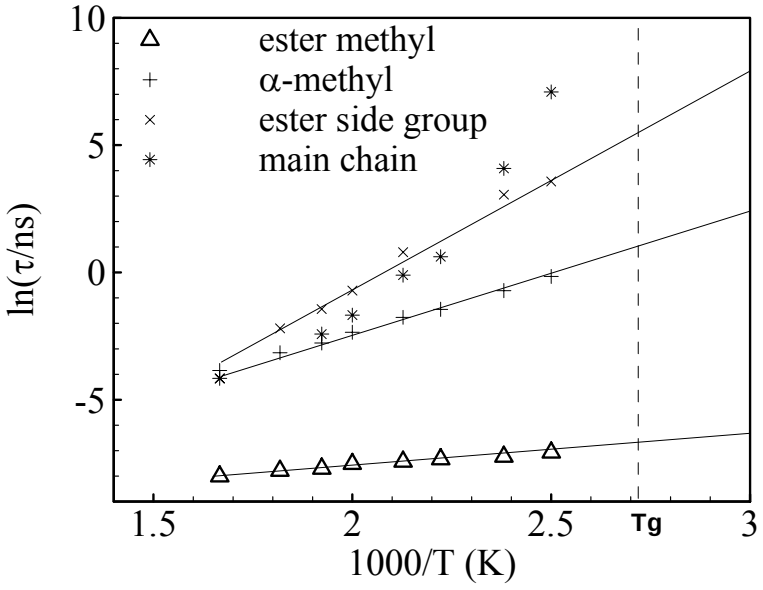

(b)

Fig. 6.21 Summary of temperature dependence of relaxation times for different relaxations at: (a) q = 0.6 Å^{-1}; (b) q = 1.5 Å^{-1}. (Chen et al., 2006b)

data. Further, α- and ester CH_3 activation energies approach values reported in literature, and rotation times for both CH_3 rotation agree well with the experimental measurements. The activation energy for the entire ester side group rotation is consistent with the value reported for the β-relaxation measured from dielectric experiments. We confirm that the β-relaxation originates from rotation of the ester side group, as first suggested from NMR experiments. This rotation contributes with the same activation energy above *Tg*. Finally motion of the main chain does not show Arrhenius temperature dependence but rather diverges as *Tg* is approached. The spatial dependence of main chain relaxation times follow $\tau \propto q^{-2/\beta}$, indicative of translational motion. Both of these observations support the idea that the α-relaxation is associated with the motion of the main chain in PMMA.

Chapter 7
Effects of Blending on the Dynamics of Poly(ethylene oxide) and Syndiotactic Poly(methyl methacrylate)

This chapter investigates the dynamics of poly(ethylene oxide) and syndiotactic poly(methyl methacrylate) in the PEO/PMMA blend with PEO weight concentration of 20% by means of molecular dynamics simulation (MD). The results are compared to the pure component dynamics well above glass transition temperature *Tg*. As discussed in Chapter 6, using this method we successfully isolate the side group rotation from other motions in PMMA and thus we can directly compare CH_3 rotation, ester rotation and main chain backbone motion between blend and pure PMMA. The elastic incoherent scattering function (EISF) obtained from the methyl group rotation of PMMA in the blend is consistent with that in pure PMMA and both of them approach a multi-fold rotation model. Our results also indicate that the methyl group rotation and β-relaxation is sensitive to blending, which is in contrast with general observations below *Tg* in blends. We attribute this affected local dynamics to the higher temperature and the long side chain of PMMA. Finally we show that distinct dynamics is observed in this blend. The change in the dynamics of PMMA upon blending with PEO is solely a result of the shift in the glass transition temperature.

7.1 Introduction

In Chapters 5 and 6, the dynamic behavior of pure PEO and pure PMMA melts were investigated using molecular dynamics simulations. We showed that the simulation models for both components are successful in describing the structure and dynamics of real samples. PMMA was found to exhibit complex dynamics. Four different relaxation processes are observed in PMMA: α-methyl group rotation, ester methyl group rotation, β-relaxation and the α-relaxation. Using molecular dynamics simulation, these motions are successfully isolated at temperatures above *Tg*.

The α-relaxation is believed to be strongly influenced by environment (Gómez et al., 2001; Arbe and Richter, 1996). More localized motions, such as the β-relaxation and side group rotations are presumed to be independent of local environments (Bieze et al., 1994; Zhu et al., 1994; Merenga et al., 2001). One way to characterize this is by looking at mixtures. This has been done with polymeric glass formers. An example is the PEO/PMMA blend, which has been the target of numerous studies (Arbe et al., 2001; Adams and Adolf, 1999). When these materials are blended, the relaxation times move closer together, with the fast process slowed and the slow process becoming faster. Rotation of the methyl groups and the β-relaxation in polymer blends are examples of more localized motions which are expected to be unchanged. From quasielastic neutron scattering (QENS) it is found that the methyl group rotation of poly(vinyl methyl ether) [PVME] is hardly sensitive to blending with polystyrene [PS] even for blends with 80 wt% of PS (Mukhopadhyay et al., 1998). Arbe et al. found that the β-relaxation for poly(vinylethylene) (PVE) is not modified by blending with polyisoprene (PI) (Arbe et

al., 1999). All this indicates that more localized a molecular motion is, the less it would be affected by blending. In our work we find that this is not true for PMMA when mixed with PEO.

In this chapter, we will examine the local dynamics in a mixture of PEO [Tg ~ 220 K] and PMMA [Tg ~ 370 K] at temperatures above blend *Tg* with emphasis placed on the effect of blending on the methyl group rotation and the β-relaxation of PMMA.

7.2 Simulation details

7.2.1 Model

The explicit atom (EA) simulations were performed on 20 wt% PEO/ 80wt% syndiotactic PMMA with 42 chains of PMMA and 8 chains of PEO in the system at temperatures of 400, 420, 440, 470, 500, 550, and 600 K. PMMA chains consist of 155 atoms, while PEO chains consist of 218 atoms.

Three kinds of interactions are involved in the force fields for this blend model: the interaction between PMMA atoms themselves, the interaction between PEO atoms themselves and the intermolecular interaction between PEO and PMMA atoms. The force field equation and parameters used for the first two parts are detailed in previous chapters. The force field for the third part is summarized in Table 7.1. The cut-off distance for the nonbonded interactions is 8 Å.

Assuming that there is no volume change when PEO and PMMA are blended, the density of the blend can be obtained from those of the pure components by

$$\rho^{blend} = \frac{m}{\frac{m_1}{\rho_1} + \frac{m_2}{\rho_2}} \tag{7.1}$$

In the above equation, m is the total mass of the blend, and m_1 and m_2 are the masses of PEO and PMMA, respectively. ρ_1 and ρ_2 are the corresponding densities.

Table 7.1 Interaction Parameters between PEO and PMMA molecules.

molecule	$u^{nb}(r_{ij}) = 4\varepsilon\left[\left(\frac{\sigma}{r}\right)^{12} - \left(\frac{\sigma}{r}\right)^{6}\right] + \frac{1}{4\pi\varepsilon_0}\frac{q_i q_j}{r_{ij}}$				
	Mixing rules $\sigma_{ij} = \sqrt{\sigma_i \sigma_j}$ $\varepsilon_{ij} = \sqrt{\varepsilon_i \varepsilon_j}$				
	Atom type		σ_i (Å)	ε_i (kcal/mol)	q_i (e.c.)
PMMA	C3	C in CH_3 connected to main chain	3.52	0.067	−0.135
	C2	C in CH_2 group	3.52	0.067	−0.09
	C	C in the main chain	3.20	0.051	0.00
	CD	C connected to O by double bond	3.75	0.105	0.51
	OD	O connected to C by double bond	2.96	0.210	−0.43
	O	O in ester group	3.00	0.170	−0.33
	CO	C in CH_3 connected to ester O	3.50	0.066	0.16
	H	H in alkane CH_3 or CH_2 groups	2.50	0.030	0.045
	HO	H in ester OCH_3 group	2.42	0.015	0.030
PEO	C3	C in CH_3 group	3.88	0.095	0
	C2	C in CH_2 group	3.88	0.095	−0.066
	O	O in PEO	3.51	0.215	−0.256
	H	H in CH_2 group	3.20	0.010	0.097
	HC	H in CH_3 group	3.20	0.010	0

7.2.2 Equilibration

Systems are equilibrated for at least 3 ns before collecting data, followed by production runs of 5 ns for the EA simulations. Structural [intermolecular packing $g^{inter}(r)$] and dynamical [self intermediate scattering function $S(q,t)$] properties calculated over two 2 ns blocks following the proposed equilibration of 3 ns have no indication of drifts, suggesting that the equilibration time is sufficient. Figure 7.1 gives an example of the illustration of self intermediate scattering function $S(q,t)$ calculated at two different blocks following the allowed equilibrium time.

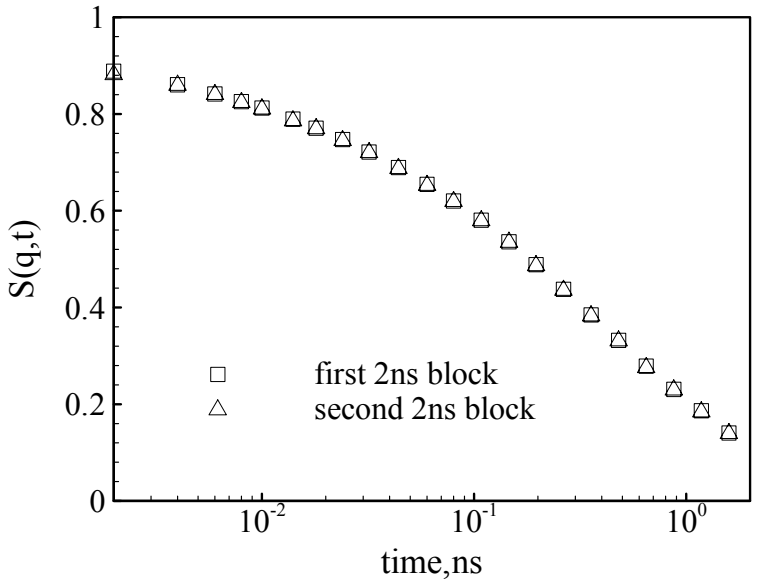

Fig. 7.1 A representative self-intermediate scattering function calculated over 2 ns blocks to illustrate the lack of drift in dynamic properties at q = 0.4 Å^{-1} and T = 500 K.

7.3 Verification of blend simulation model

To validate the simulation model, both structural and dynamic neutron measurements are used in this chapter. The static structure factor *S(q)*, which represents preferred packing distance in the system, was evaluated and compared to available neutron scattering results (Farago et al., 2005). The dynamics structure factor *S(q,t),* which describes the mobility of atoms in the system, was calculated and compared to the our DCS measurements (For the DCS instrument details, refer to Chapter 6). The orientation autocorrelation function *G(t)*, which describes the decorrelation of the orientation of the C-H bond vector, was calculated and compared to NMR results (Lutz et al., 2003).

7.3.1 Static structure factor

Figure 7.2 shows the static structure factor *S(q)* of the blend and pure PMMA calculated from Eqs. (2.38) and (2.39) at 500 K as well as measured by means of neutron diffraction experiments (ILL, Grenoble, France) at room temperature (Farago et al., 2005). Since the scattered neutron intensities depend on neutron flux and sample size, to compare between different samples, the intensity from neutron diffraction measurements has to be rescaled to overlap in the q range of 2.5 – 4 $Å^{-1}$. It is believed that the intensities in this q range do not vary significantly with blend composition. The simulation data in this figure is also renormalized to match with the experimental data at high q.

In the investigated q range neutron data shows three peaks for both the blend and pure PMMA. The sharp peaks at q = 2.7 Å^{-1} and q = 3.1 Å^{-1} are due to the scattering from aluminum holder. The first peak position doesn't change, but the peak intensity becomes stronger with adding PEO to PMMA. The second peak shifts to low q value and the third peak remain the same in the blend. Similar behavior can be observed in the simulation data for pure PMMA and PMMA in the blend.

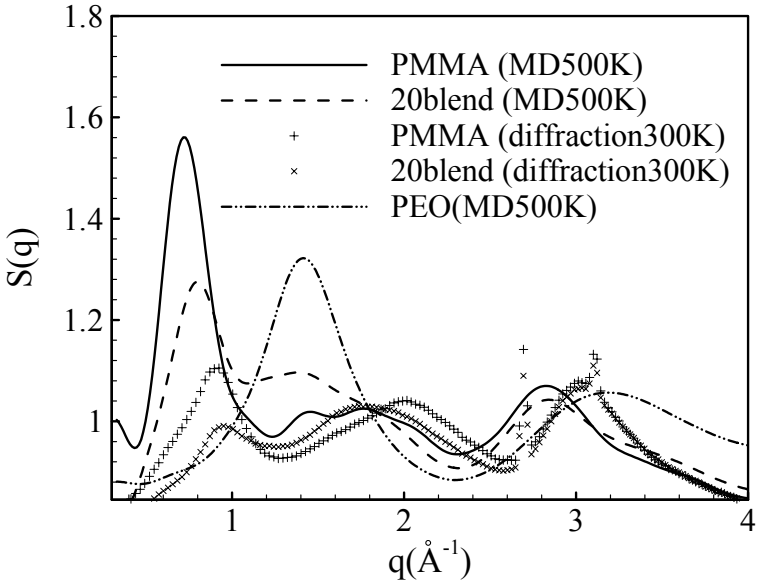

Fig. 7.2 Structures of 20% PEO/PMMA blend from simulations and experiments.

For both simulation data and neutron data, the blend has less intensity in the first peak than pure PMMA, which can be explained that added PEO introduces more disorder for the PMMA intermolecular correlations. The first peak located at q = 0.8 Å^{-1} in the simulation data has no significant change in the blend, whereas it is located at lower q

values than neutron data, possibly due to the thermal contraction since simulation data and neutron data are taken at different temperatures. The second peak is broader and actually in simulation data it appears as two small peaks, while with adding PEO in the PMMA, it moves to low q values and the second peak intensity in the blend becomes stronger. Both experimental and simulation data show this trend. It indicates adding PEO increase the packing distance pair that is located in the second peak range. As shown in Chapter 5, the first peak for pure PEO is located at q = 1.4 Å^{-1}, indicating that the region of enhanced intensity corresponds to packing of PEO. Compared to their counterpart from neutron data, both the second and the third peaks in the simulation shift to low q values, which as discussed in Chapter 6 suggests that the sequence difference between the real experimental sample (80% sequence) and simulation sample (100% sequence) might contribute.

7.3.2 Self intermediate structure factor

The self-intermediate structure factor *S(q,t)* is calculated through Eq. (2.44). To compare with DCS measurements in which a 20 wt% hPEO/dPMMA sample was used and the signal is dominated by hydrogen atoms in PEO, we include only hydrogen atoms of PEO in the calculation. Plotted in Fig. 7.3 is the *S(q,t)* from simulation and DCS experiments at q = 1.45 Å^{-1} and T = 420 K. As shown in this figure, the simulated PEO in the blend has faster dynamics than PEO in the experimental samples. Since the investigated experimental sample contains deuterated PMMA with a weight fraction of 80%, the coherent signal from PMMA cannot be negligible. For this purpose, in Fig. 7.3 we also include MD results with coherent scattering from deuterated PMMA accounted.

After this correction, the fast dynamics (t < 3 ps) from MD results is in good agreement with experimental data. Difference is observed in the slow dynamics (t > 3 ps), which may be due to different molecular weight used in simulation (1350 g/mol) and experiments (460 000g/mol).

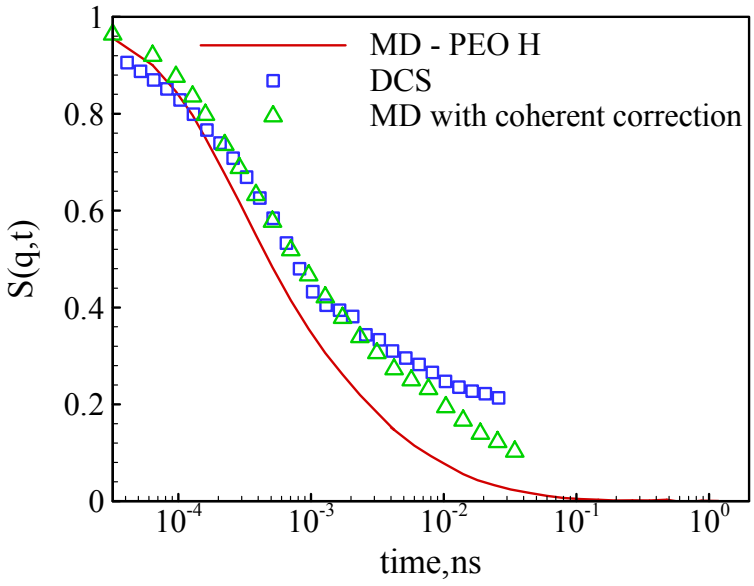

Fig. 7.3 Self-intermediate structure factor of pure PEO and PEO in 20% PEO/PMMA blend from simulations and experiments at q = 1.45 Å^{-1} and T = 420 K.

7.3.3 Orientation autocorrelation function (OACF)

As discussed in Section 5.5.3, the orientation autocorrelation function is measurable in NMR experiments (Lutz et al., 2003). From the trajectory obtained from simulations, the OACF can be calculated according to Eq. (2.46). We present the results from simulations in Fig. 7.4 and then fit $G(t)$ using Eq. (5.2) with τ_{lib} = 1 ps as was done by Lutz et al. (2003). The resulting parameters including those from NMR measurements

(Lutz et al., 2003) are listed in Table 7.2. The value of a_{lib}, stretching parameters and relaxation times from simulation are close to those from NMR experiments indicating that the local motion represented in the reorientation of the C-H bond vector can be adequately described by our simulations. All these results suggest that our simulation model provide reasonable description of real samples.

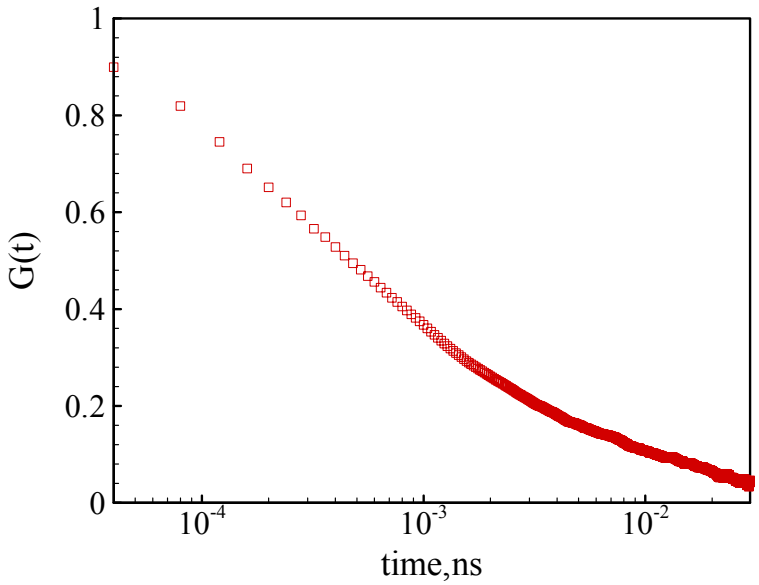

Fig. 7.4 Orientation autocorrealtion functions for C-H vectors calculated at 500 K from simulations.

Table 7.2 Comparison of fit parameters from simulations to NMR experiments (Lutz et al., 2003).

methods	a_{lib}	β	τ_{seg}(ps)
MD	0.12	0.32	1.1
NMR	0.10	0.28	1.9

7.4 Effect of blending on the local dynamics of PMMA

Although a lot of experimental techniques have been applied to investigate the dynamics of the PEO/PMMA blend, no data is available concerning the effect of blending on the localized relaxations in PMMA. In this section, we aim to provide a detailed picture how these relaxations are affected with the presence of PEO at temperature above blend *Tg*.

7.4.1 Methyl group rotation

The barrier for the ester methyl group rotation in pure PMMA is very low. In order to capture this rotation in blend, experiments have to be performed at temperatures below the *Tg* of PEO. The α-methyl group has a larger barrier than ester methyl due to the stereoisomer hindrance. At spatial scales less than 4 Å, it has comparable time scale to β-relaxation (Chen et al., 2006b), which makes harder to differentiate it from other motions experimentally. As shown in Chapter 6, we successfully isolate methyl group rotations occurring in pure PMMA at temperatures above *Tg* using molecular dynamics simulation. The same method will be used to investigate the behavior of both methyl rotations in the blend.

Neglecting translational motion by fixing the terminal position of the rotating group, the self correlation function *S(q,t)* for both methyl group rotations is calculated through Eq. (2.44). For example, in ester methyl group rotation the position of C connecting to the ester oxygen is fixed, whereas for the rotation of α-methyl side group, the position of α-C connecting to the main chain is fixed. Figure 7.5 shows the rotational

dynamics of ester and α-CH_3 groups calculated at 500 K and two q values of 0.9 $Å^{-1}$ and 1.5 $Å^{-1}$ in pure PMMA and PMMA in 20% PEO/PMMA blend. Following a fast process, rotation of the CH_3 group causes a decay which reaches a plateau at longer times. As discussed in Chapter 6, this plateau is a characteristic feature of CH_3 group rotation: The EISF represents the limited decay of rotational motion (the atoms are not free to move in any direction) and its spatial dependence describes the geometry of the motion. The EISF observed in our simulations is the same for α- and ester rotations, and is consistent with the geometry expected for methyl group rotation.

As shown in Fig. 7.6 , the EISF is not temperature dependent, nor does it change with blending, which is in agreement with some neutron scattering results from Arrighi et al. (1995b; 1996). They observed that the EISF for the PS/PVME blend with PS content lower than 40% is comparable to the EISF of pure PVME. For the same blend, in the work reported by Mukhopadhyay et al. (1998), a concentration-dependent EISF is observed. For both works, a 3-fold rotation model is assumed for the methyl group in PVME. Since the H-H distance ($r_{H\text{-}H}$) in the methyl group is the only determining factor in the calculation of the EISF [as indicated by Eq. (6.1)] and this does not change with blending, the EISF shouldn't depend on blend concentration. Figure 7.6 also presents the comparison of EISF from 3-fold, 4-fold and 6-fold rotation models with simulations. As with pure PMMA, the EISF from simulation data approaches a multi-fold rotation prediction in the blend. As discussed in Chapter 6, the librational motion of the protons on three different sites may smear out the apparent shape of the motion from a triangle [3-fold rotation] to a hexagon [6-fold rotation].

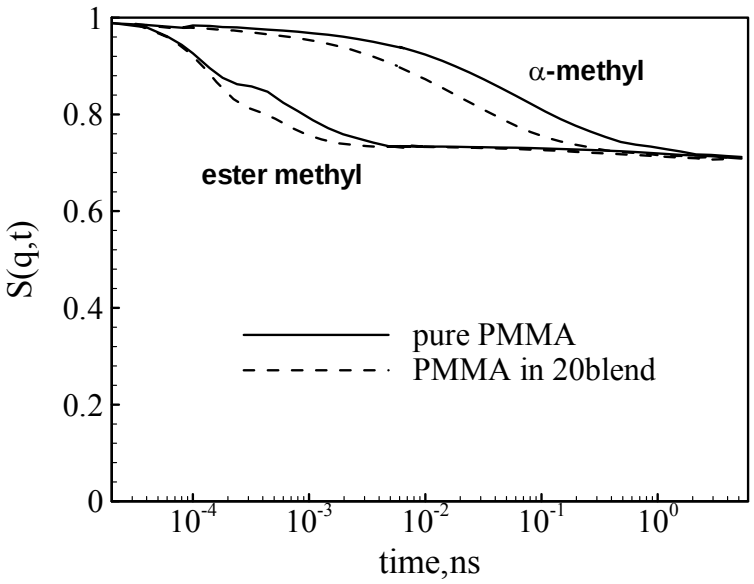

(a)

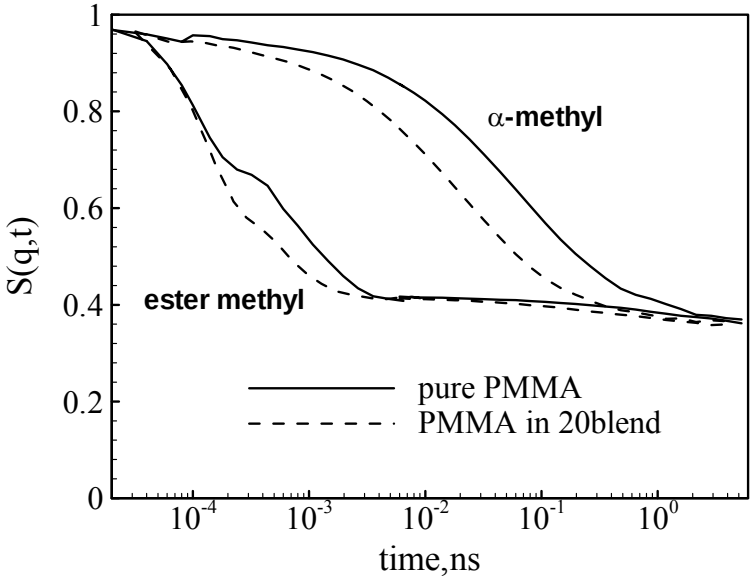

(b)

Fig. 7.5 Comparison of α- and methyl CH_3 group rotation dynamics in pure PMMA and in 20% PEO/PMMA blends at 500 K: (a) q = 0.9 Å^{-1}; (b) q = 1.5 Å^{-1}.

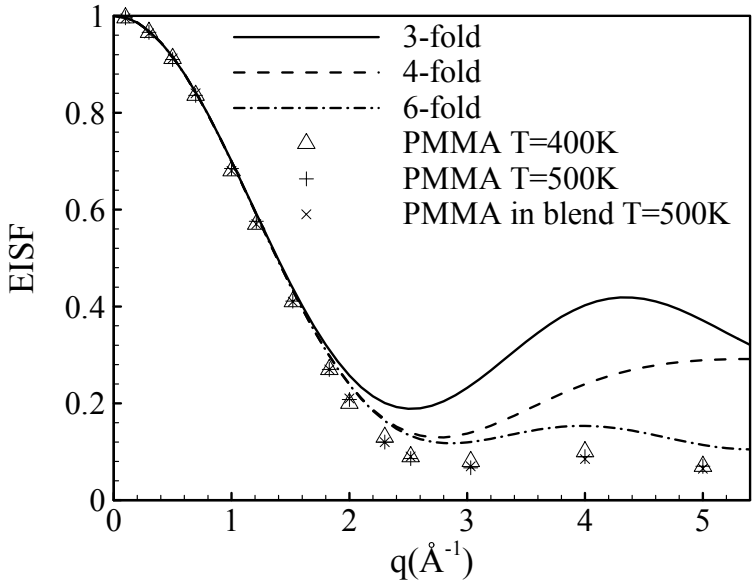

Fig. 7.6 Comparison of EISF between simulations and theoretical rotation models.

We have fit the rotational part of the *S(q,t)* for the blend using Eq. (6.1). The stretched exponential function β accounts for the existence of a distribution of rotational frequencies instead of a single rotation frequency, and have provided more reasonable results in QENS (Arrighi et al., 1995) and the pure PMMA data analysis. Figure 7.7 presents the q dependence of relaxation times calculated from Eq. (6.1) for both α- and ester methyl group rotations at 500 K for the blend and pure PMMA. Rotational times for methyl groups are insensitive to q in both cases, as is the stretching exponent β. However, the methyl rotations including both α- and ester groups are speeded in blend, which indicates that the methyl group rotations are affected by intermolecular interactions present in the PEO/PMMA blend. It is inconsistent with some general observation in experiments that the methyl group rotation is not sensitive to blending. QENS measurements (Arrighi et al., 1995b) show that the temperature dependence of

relaxation times collapse on the same curves for the ester methyl group rotation in pure PVME and in PVME/PS blends. However, Mukhopadhyay et al. (1998) examined the methyl group dynamics in this blend over a large compositional range. They found that for a large concentration of PS (80%), the PVME methyl group rotation is affected by blending. They attribute this to the additional heterogeneity introduced by the PS chains. Arrighi et al. (1995b) also present a QENS study on a blend of solution chlorinated polyethylene and PMMA (SCPE/PMMA). They found that the rotation motion of the ester CH_3 group in PMMA is sensibly altered by blending with SCPE and they attribute this to the specific interactions between the α-hydrogen of the SCPE chain and the carboxyl oxygen of PMMA.

In our case, methyl group dynamics are sensitive to blending even at a low concentration of PEO (20%). It is well believed that the rotation of methyl group rotation is driven by the torsional angle potential. To have a better understanding of the methyl group rotation, the torsional autocorrelation function (TACF), which measures how fast the torsional angle decays, is calculated.

$$G(t) = \frac{\langle \cos\phi(t)\cos\phi(0)\rangle - \langle \cos\phi(0)\rangle^2}{\langle \cos\phi(0)\cos\phi(0)\rangle - \langle \cos\phi(0)\rangle^2} \tag{7.2}$$

where ϕ is the torsional angle. These results are presented in Fig. 7.8. For both methyl groups, adding PEO accelerates this decay indicating that the conformation changes of PMMA are also speeded by the presence of PEO.

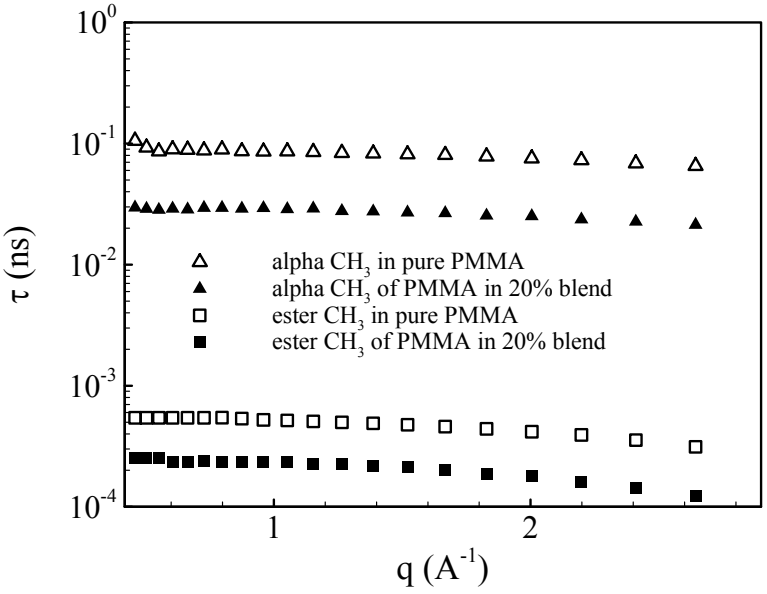

(a)

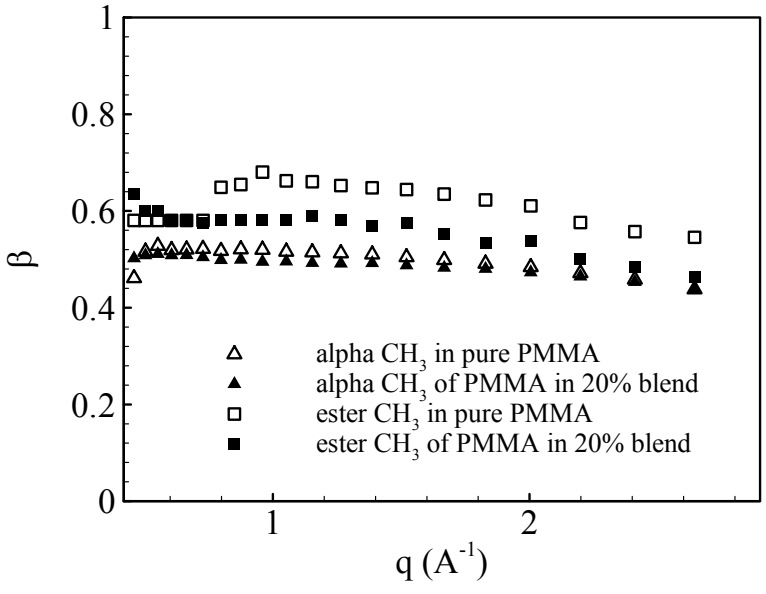

(b)

Fig. 7.7 q dependence of relaxation time and stretching paprameter β of α- and ester CH_3 group rotation in pure PMMA and in 20% PEO/PMMA blend.

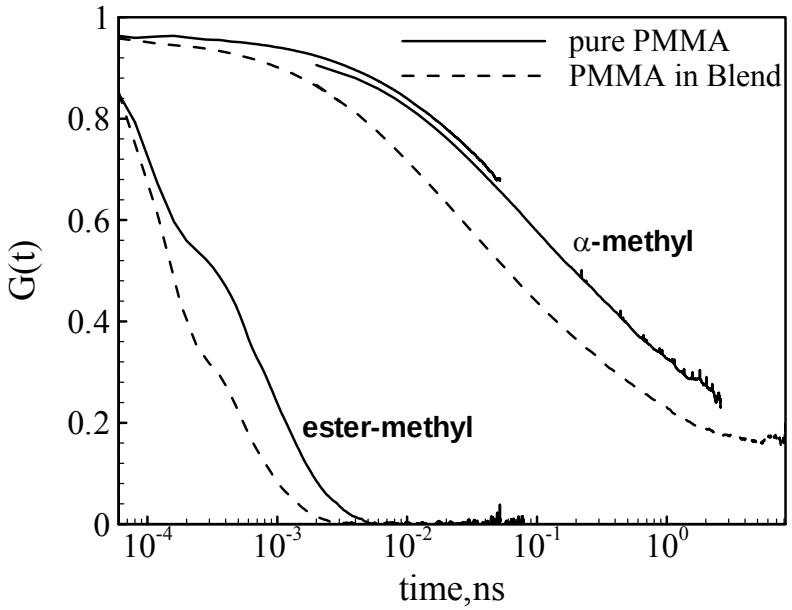

Fig. 7.8 Torsional autocorrelation function for α-methyl hydrogen and ester methyl hydrogen torsions at 500 K.

As a comparison to pure PMMA, we also calculated the torsional angle of a proton in each type of methyl group at 500 K as a function of time for the blend. The results are presented in Fig. 7.9. As with pure PMMA discussed in Section 6.5.1, the torsional angle of the α proton [H-C_3-C_1-C] in the blend also undergoes librational motion in each of three different sites [-120, 0 & 120 degrees], punctuated by quick jumps between sites. The libration motion for the ester proton [H-C_2-O-C] is so fast that the three site jump is not significant as for α proton.

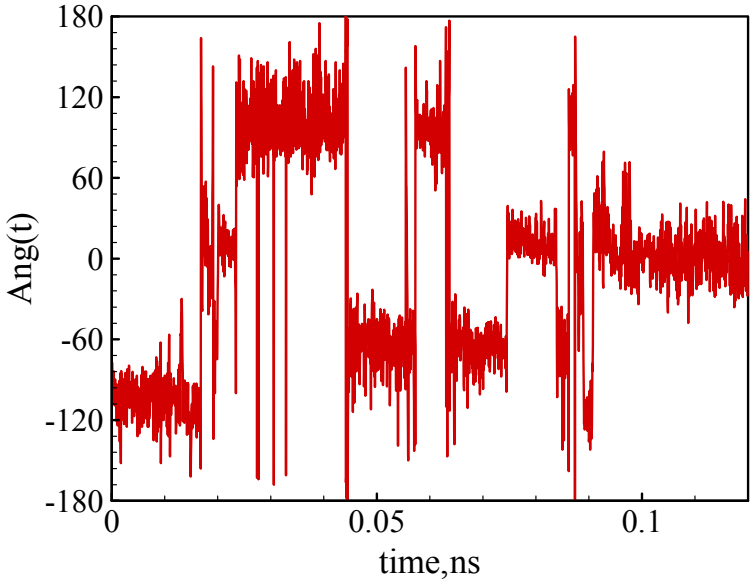

(a)

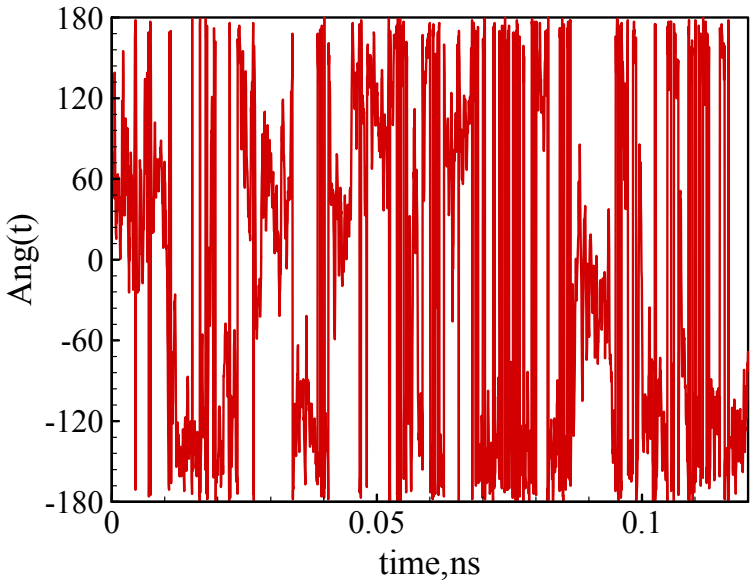

(b)

Fig. 7.9 Dihedral angle of the blend as a function of time with the time interval of 0.04 ps for: (a) α-methyl group; (b) ester methyl group at 500 K.

Since no specific interaction exists between PEO and PMMA, we now discuss a potential explanation. Most of the experiments are taken at low temperatures such that the methyl group rotation is surrounded by molecules that are immobile. Those molecules may impose little effect on the conformation changes, while the fast mobility of surrounding polymer melts at high temperatures might cause significant effect. In addition, a longer side group will be easily affected by surroundings than shorter ones. Therefore, the low *Tg* of PEO, the long side chain of PMMA, and the high simulation temperatures may contribute to the speeded ester methyl group rotation. The rotation of α-methyl group is also affected. One way to test this idea is to frozen the sample below the PEO *Tg*, however due to computational limits, it is not accomplished in this work.

In Fig. 7.10, we plot the relaxation time as a function of inverse temperature for both α- and ester methyl group rotation. As can be seen from the graph, for both rotations there exists an Arrhenius temperature dependence of relaxation time. The activation energies calculated from Eq. (2.48) for CH_3 group rotation in pure PMMA and PMMA in 20% blend are illustrated in Table 7.3. The activation energies for both α- and ester methyl group rotations in blend are a little lower than those in pure PMMA, while they are both close to the value reported in literature for pure PMMA at low temperatures (Arrighi et al., 1995a and 1995b; Higgins and Benoĭt, 1999; Allen et al., 1998). These results suggests that the addition of PEO lowers the barrier to the rotations of both α- and ester methyl groups.

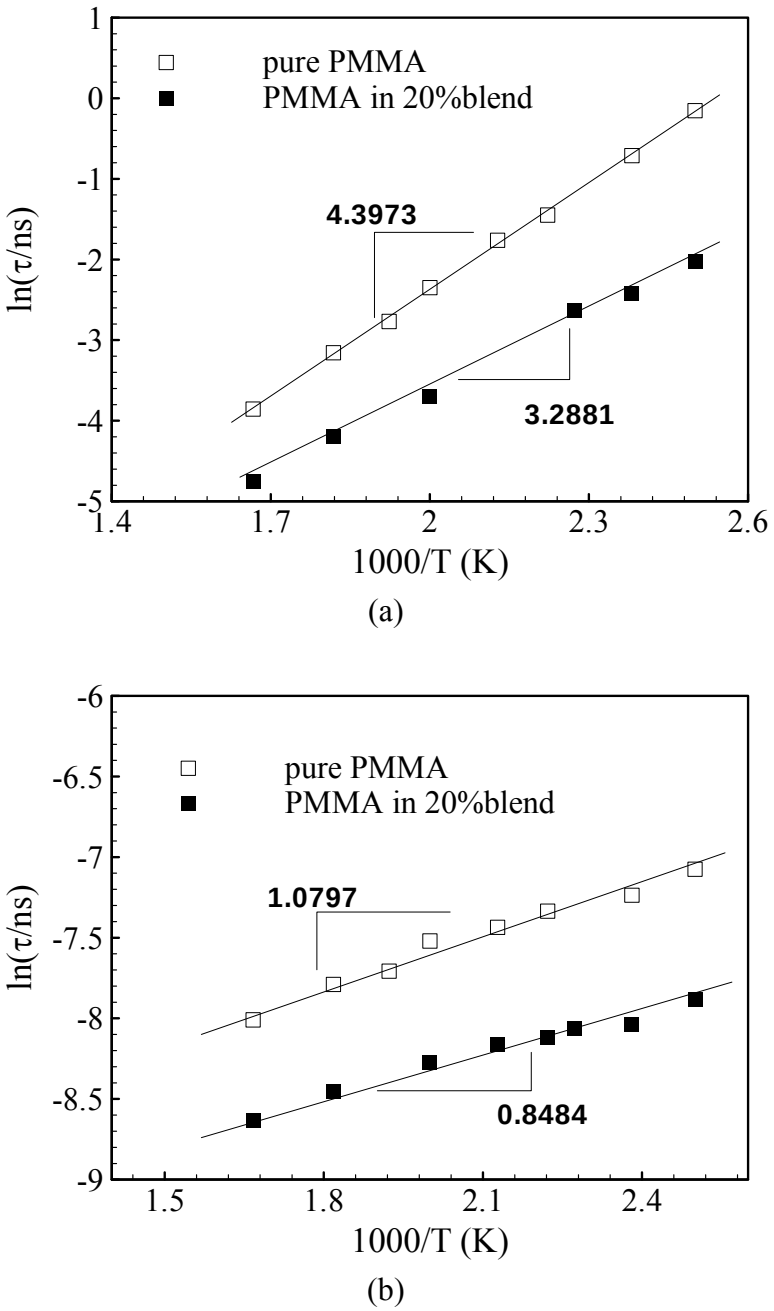

Fig. 7.10 *T* dependence of relaxation time methyl; group rotation in pure PMMA and in 20% PEO/PMMA blend at $q = 1.5$ Å^{-1} for: (a) α-methyl group; (b) ester methyl group.

Table 7.3 Activation energies of methyl group rotations in pure PMMA and PMMA in 20% blend.

Activation energies (kJ/mol)	Pure PMMA	PMMA in 20% blend
α-methyl	36.56	27.34
ester methyl	8.98	7.05

7.4.2 Entire carboxyl group rotation

In Chapter 6, we demonstrated that the possible origin of *β*-relaxation is the rotation of the entire side group, i.e. the $–COOCH_3$ group, around the C-C bond linking it to the main chain. In this chapter, we will investigate how this is affected by blending with PEO. The self intermediate scattering function *S(q,t)* for ester side group rotation is calculated using Eq. (2.44) by fixing the position of C connecting it to the main chain. Figure 7.11 shows the results at 500 K and two *q* values of 1.5 $Å^{-1}$ and 2.1 $Å^{-1}$. Four processes are observed. The fastest process taking place at times shorter than 0.1 ps is attributed to the cage motion discussed in Section 7.5. Second fastest process, which occurs in the time range of 0.2-2 ps, is due to the ester methyl group rotation. The rotation of the entire side group, which is slower than the methyl group rotation, contributes to the slow process lying in the time range of 2 ps - 1 ns. The constant value (EISF) is reached at longer times and illustrated in Fig. 7.12. The same EISF is observed for the entire side group rotations in pure PMMA and in blend. Both rotations follow the prediction of the isotropic rotational diffusion model, in which continuous small angle rotations occur and the rotating molecule has no preferred spatial orientation.

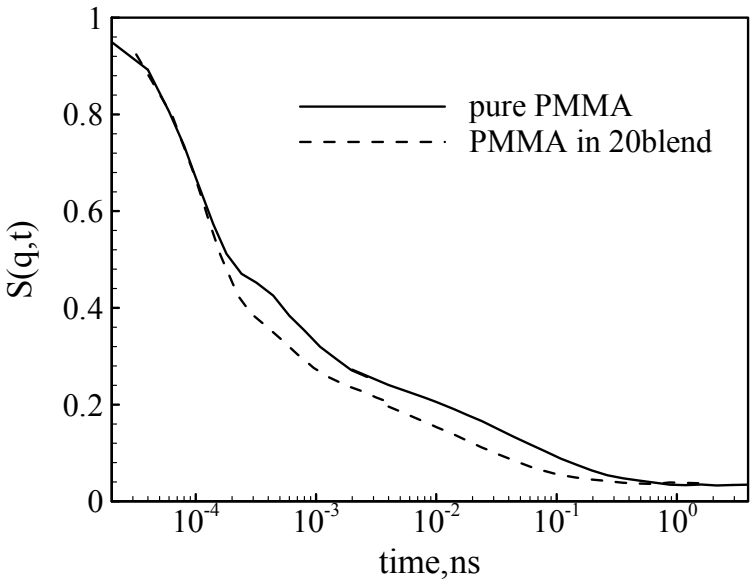

(a)

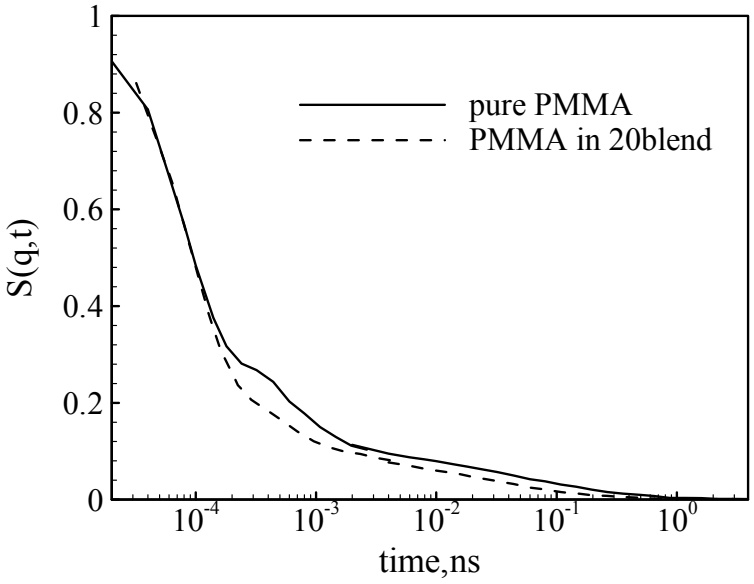

(b)

Fig. 7.11 Comparison of entire side group rotation dynamics in pure PMMA and in 20% PEO/PMMA blends at 600 K and at: (a) q = 1.5 Å^{-1}; (b) q = 2.1 Å^{-1}.

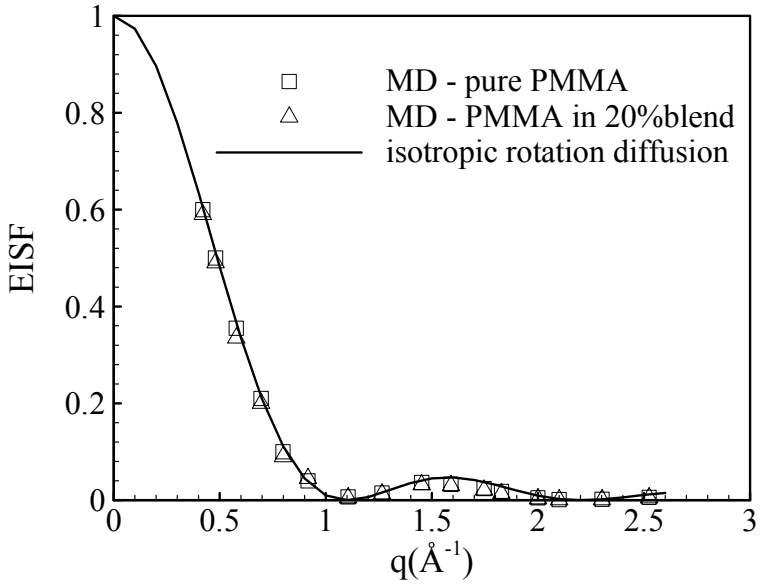

Fig. 7.12 q dependence of the simulated EISF from pure PMMA and PMMA in 20% blend for rotation of the entire ester group rotation at 600 K, compared to the isotropic rotation diffusion model.

In the analysis of the entire ester group rotation, we use Eq. (6.1) to fit the ester group rotation part. At all temperatures the relaxation times and stretching parameter β have weak q dependence and the result is shown in Fig. 7.13. At all q values, the relaxation times calculated from Eq. (6.1) appear to have an Arrhenius temperature dependence and the activation energy calculated from different q values are almost the same.

Figure 7.14 shows the relaxation time for the entire ester group rotation at q = 1.5 $Å^{-1}$. The activation energy calculated for PMMA in blend is around 69.8 kJ/mol, which is slightly lower than the value of 77.4 kJ/mol for pure PMMA. Smaller relaxation times and activation energy suggest that the entire side group rotation is speeded in blend. Based on previous analysis, this is expected since the long chain is more easily affected

by PEO than more localized methyl rotation. The distribution of the relaxation times seems not changed by blending as it is evidenced by the same value of β.

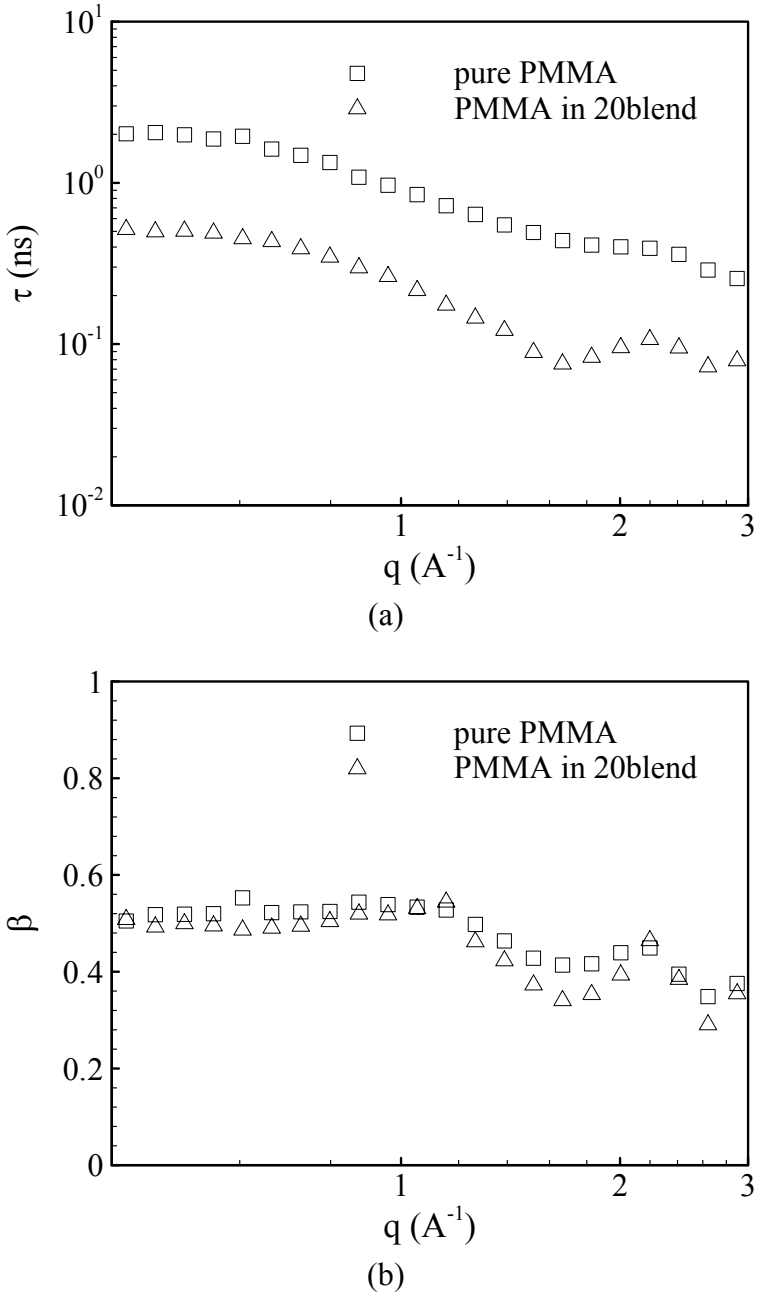

Fig. 7.13 q dependence of relaxation time and stretching paprameter β of entire side group rotation in pure PMMA and in 20% PEO/PMMA blend.

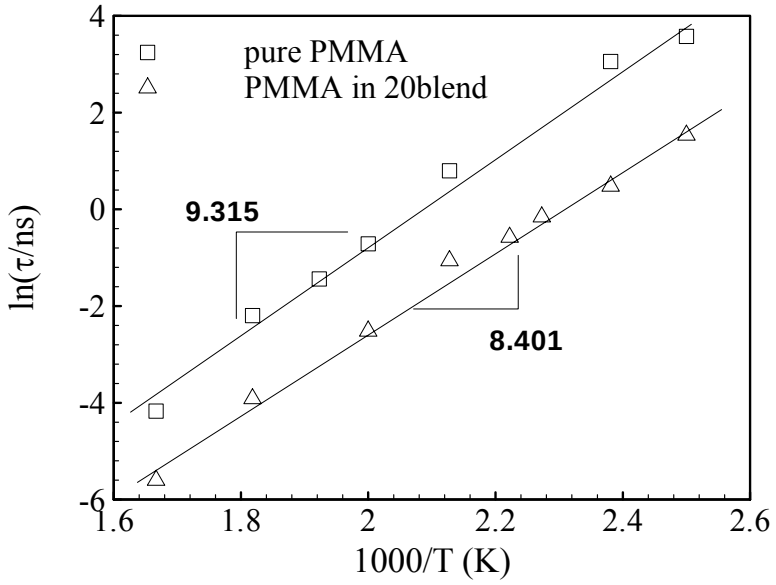

Fig. 7.14 Temperature dependence of relaxation times of entire side group rotation in pure PMMA and in 20% PEO/PMMA blend at q = 1.5 Å^{-1}.

7.4.3 Main chain motion

In Chapter 6, α-relaxation is confirmed to originate from the main chain backbone motion. For the investigation of the effect of blending on α-relaxation, *S(q,t)* is calculated using Eq. (2.44) with only hydrogen atoms in the main chain considered. Figure 7.15 presents *S(q,t)* for the main chain motion at different temperatures. As shown in the graph, PMMA moves faster when blending with PEO. Since there is no EISF, we fit the main chain decay with Eq. (2.47). The q and temperature dependences of relaxation times are shown in Figs. 7.16 and 7.17, respectively. The q dependence of relaxation times follows $\tau \propto q^{-2/\beta}$ rules, which is characteristic of α-relaxation in polymers. The stretching exponent β is smaller in the blend, indicating that the main chain relaxation has a broader distribution. This is expected due to a larger distribution

of relaxations introduced by new environments. As shown in Fig. 7.17, the main chain motion accelerates with increasing temperature for pure PMMA and PMMA in the blend. Relaxation times for pure PMMA increase rapidly as the temperature decreases toward *Tg*, while for PMMA in blend an Arrhenius temperature dependence with an activation energy of 54 kJ/mol is observed at temperatures far above *Tg* of the blend. The activation energy is much smaller than that observed in QENS experiments (110 kJ/mol) (García Sakai et al., 2004), which may be due to the different investigated temperature range (QENS: $Tg + 30 \sim Tg + 150$; MD: $Tg + 70 \sim Tg + 270$).

To test if PMMA dynamics in the blend can be scaled with glass transition temperature, we attempt to collapse all the data on a single curve by comparing the data at a temperature the same distance above the glass transition. These results are presented in Fig. 7.18. As shown in this figure, the data collapse on the same curve, indicating that the change in the time scale of the main chain motion is solely a result of the change in the glass transition temperature. This is consistent with the observation from neutron scattering measurements (García Sakai et al., 2004).

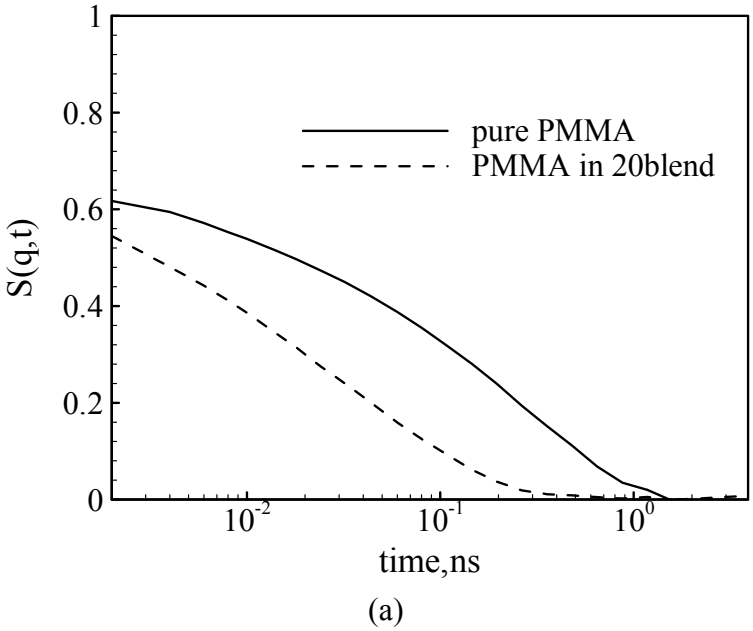

(a)

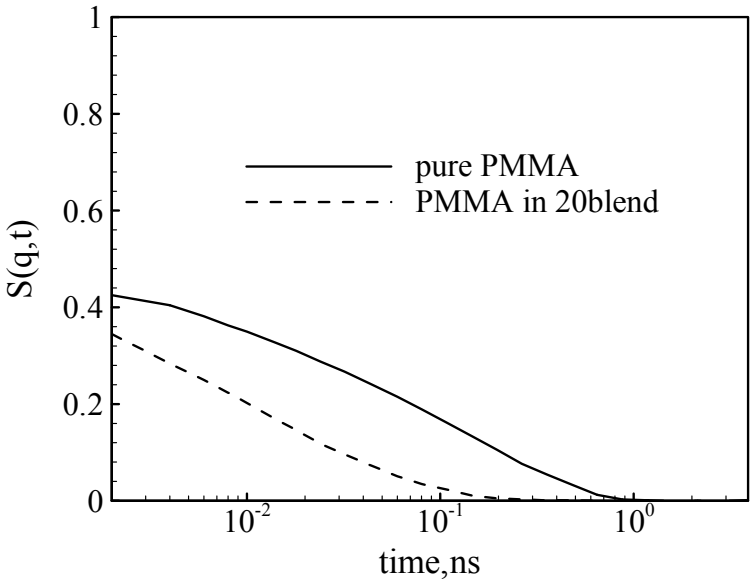

(b)

Fig. 7.15 Comparison of main chain dynamics in pure PMMA and in 20% PEO/PMMA blends at 500 K at two q values: (a) q = 1.5 Å^{-1}; (b) q = 2.1 Å^{-1}.

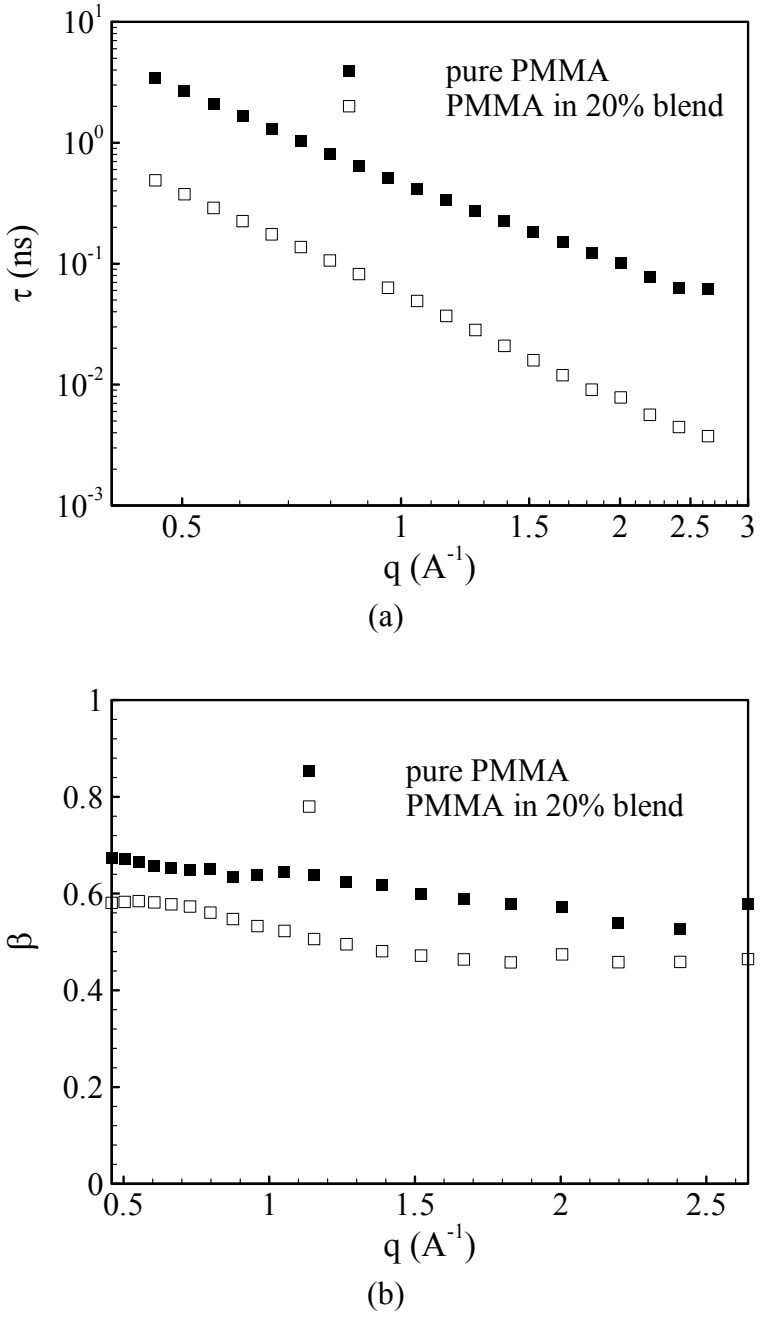

Fig. 7.16 q dependence of relaxation time and stretching parameter β of main chain motion in pure PMMA and in 20% PEO/PMMA blend at 500 K.

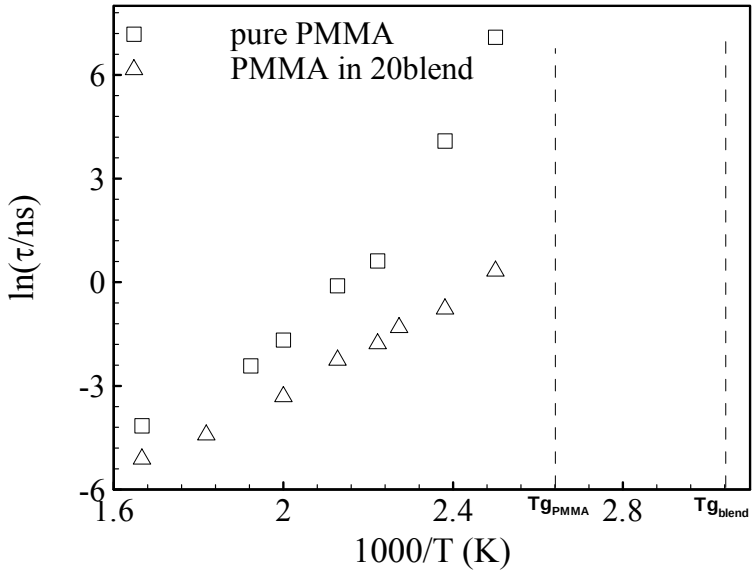

Fig. 7.17 Temperature dependence of relaxation of main chain motion in pure PMMA and in 20% PEO/PMMA blend at q = 1.5 Å^{-1}.

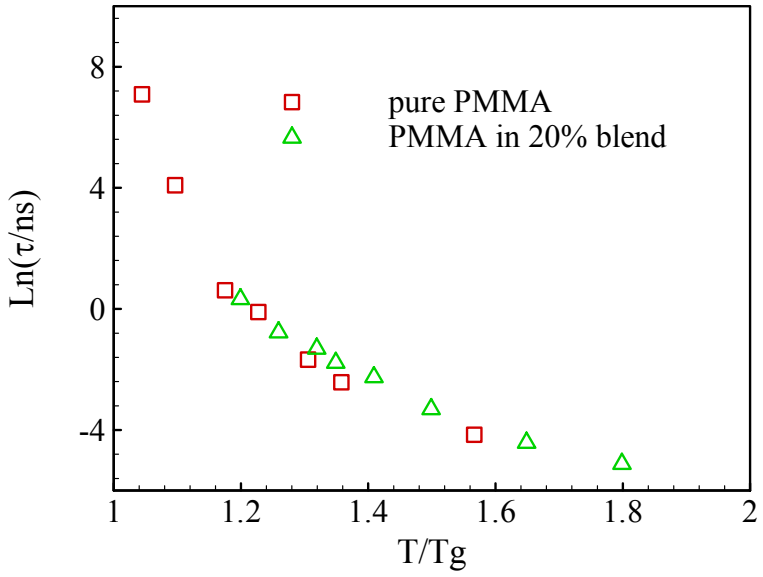

Fig. 7.18 Comparison of relaxation times of main chain motion in pure PMMA and in 20% PEO/PMMA blend at q = 1.5 Å^{-1} and the same *T/Tg*.

7.5 Distinct dynamics of PEO and PMMA in blend

To characterize the mobilities of PEO and PMMA in blends, from the atomic trajectories obtained from simulation, we calculate the self intermediate scattering function *S(q,t)* using Eq. (2.44) for PEO and PMMA, respectively. To be consistent with previous results for pure components, only hydrogen motion is accounted for this calculation.

Figure 7.19 presents the calculated *S(q,t)* for hydrogen dynamics in PEO and PMMA of the blend at *q* values of 0.4 $Å^{-1}$ and 1.5 $Å^{-1}$ and a temperature of 500 K. In this figure *S(q,t)* for pure PEO and PMMA are also included. All the spectra are characterized by a two-step decay with a fast process at times shorter than 2 ps, and a slow process at longer times, which is a typical behavior observed in polymers (Chen et al., 2006a). The fact that the fast process is identical for pure PEO and PEO in the blend confirms that it arises from unhindered motion in a cage formed by nearest neighbors. In contrast, motions at smaller times decay faster for PMMA in blend than pure PMMA. As discussed above, the ester methyl group rotation, which is speeded in blend, falls within this time range for in PMMA. The slow process (times longer than 2 ps) at temperatures above *Tg* groups all the relaxations present together. At both *q* values PEO hydrogen atoms decay faster than PMMA ones, indicating that PEO and PMMA display distinct dynamics in this blend. Compared with their pure component, PMMA moves faster in blend, while PEO moves slower. These findings are in agreement with the usual observation in miscible polymer blends that the low-*Tg* component is slowed and the high-*Tg* component is accelerated.

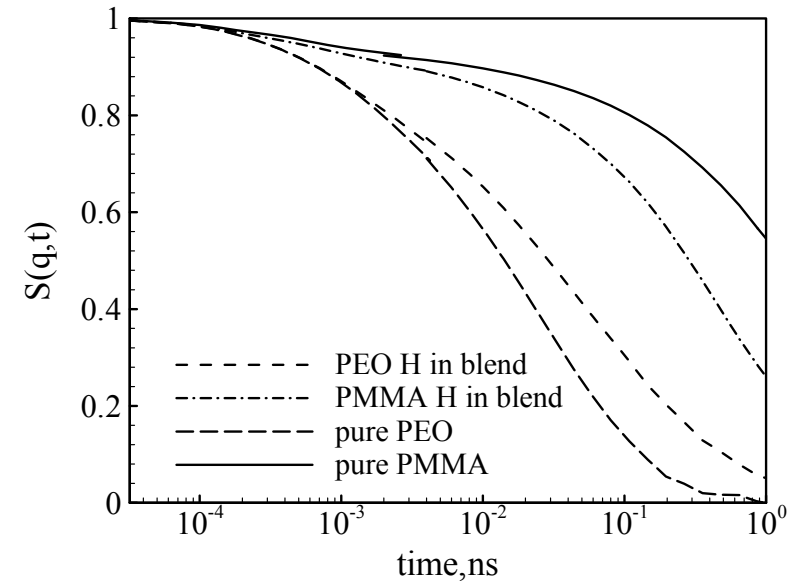

(a)

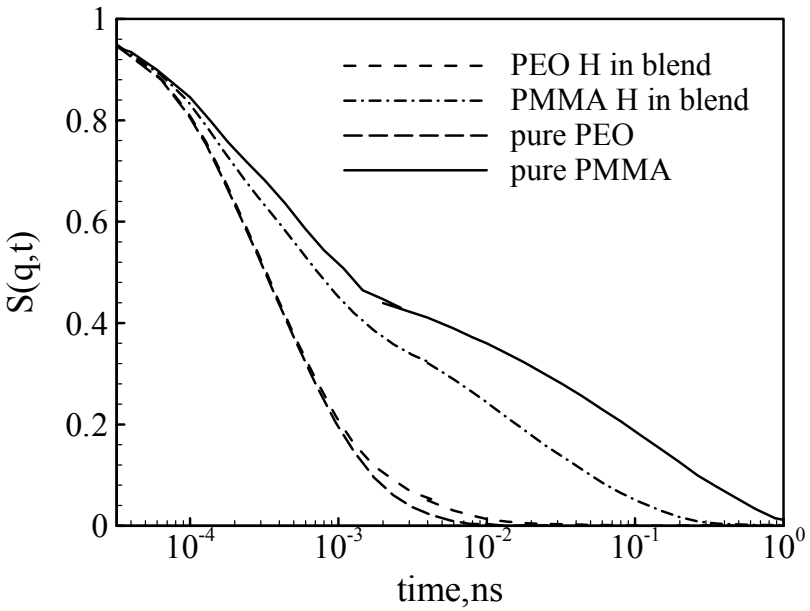

(b)

Fig. 7.19 Comparison of PEO and PMMA dynamics in the pure components and the 20% blend at 500 K and two q values: (a) q = 0.4 Å^{-1}; (b) q = 1.5 Å^{-1}.

7.6 Summary and conclusion

We have investigated the dynamics of PEO/PMMA blend with PEO weight concentration of 20% well above glass transition temperature *Tg* by means of an explicit atom molecular dynamics simulation with the emphasis focused on the effect of blending on localized processes in PMMA. This mixture is a model miscible polymer blend which received a lot of attention due to the minimum interaction and widely separated glass transition temperatures. The performance of the simulation model for blend is evaluated using neutron scattering and NMR data. This model has been shown to be able to capture both static and dynamic properties of real blend samples. Using this model we successfully isolate the methyl group rotations from other motions at high temperature in the blend. Our results show that the both α- and ester methyl group rotations in the blend are speeded, as indicated by the smaller rotational time and lower activation energy in the blend, which are not consistent with the normal findings at low temperatures that the methyl rotation is insensitive to blending. The accelerated β-relaxation in blend is also observed. We suggest that the measurement temperature and the long side chain may contribute to this difference. The change in the dynamics of PMMA upon blending with PEO is solely a result of the shift in *Tg*, which is consistent with our experimental observations (García Sakai et al., 2004).

Chapter 8
Summary and Future Work

8.1 Summary

Blending has been recognized as a potential tool to tune polymers with designed properties. The present work investigates the segmental dynamics of a miscible polymer blend using molecular dynamics simulations with neutron scattering as a test of simulation model accuracy. The system under consideration is 20 wt% PEO/PMMA blend, an excellent candidate for the current study due to its minimal interaction and widely separated component glass transition temperatures.

First a detailed comparison of two levels of modeling, i.e. united atom (UA) and explicit atom (EA) for a polymer, PEO, is presented. EA and UA models for both static and dynamic observables is compared and evaluated using neutron scattering and NMR data. Both models are comparable and in agreement with neutron diffraction for static properties. The dynamics represented via QENS experiments are in reasonable agreement with the EA model. The UA model also performs adequately, but only in the case that backbone carbon and oxygen atom motion are compared to the proton motion probed in the experiment. The dynamics of protons reinserted in the UA simulation do not agree well with QENS data. Both UA and EA data do provide a good description of NMR data, where the performance of both models is comparable.

PMMA shows complex local dynamics including α-methyl rotation, ester methyl rotation, the β-relaxation and the α-relaxation. To examine all the processes in PMMA,

an explicit model is required. The performance of the PMMA EA model for both static and dynamic observables is then evaluated using neutron scattering data. The performance of this model is comparable and in agreement with neutron diffraction for static properties. The dynamics represented via QENS experiments are also in reasonable agreement.

Molecular dynamics simulations are adopted to successfully isolate the local motions, i.e. main chain motion, rotation of the ester side group, and rotation of both α- and ester methyl groups occurring in PMMA, which is hard to achieve with experimental techniques at high temperatures. An Arrhenius temperature dependence is evident for all three rotations: the α-methyl, the ester methyl and the entire ester side group. The activation energies follow ester side > α-methyl > ester methyl, consistent with available data. Further, α- and ester CH_3 activation energies approach values reported in literature, and rotation times for both CH_3 rotation agree well with the experimental measurements. The activation energy for the entire ester side group rotation is consistent with the value reported for the β-relaxation measured from dielectric experiments. We confirm that the β-relaxation originates from rotation of the ester side group, as first suggested from NMR experiments. This rotation contributes with the same activation energy above *Tg*. Finally motion of the main chain does not show Arrhenius temperature dependence but rather diverges as *Tg* is approached. The spatial dependence of main chain relaxation times follow $\tau \propto q^{-2/\beta}$, indicative of translational motion. Both of these observations support the idea that the α-relaxation is associated with the motion of the main chain in PMMA.

Finally, the segmental dynamics in 20% PEO/PMMA blend is investigated. This simulated sample shows no sign of crystallinity at all the temperatures. Distinct segmental dynamics are observed. Compared with the pure components, PEO is retarded while PMMA is speeded, which is consistent with what is normally observed in polymer blends.

The effect of blending on the dynamics of the main chain motion, rotation of the ester side group, and rotation of both methyl groups in PMMA are also explored. Contrary to the normal observation, which shows the localized motions are not sensitive to blending, we found that both the methyl group rotation and β-relaxation in PMMA are speeded on blending with 20% PEO, which is evidenced by the smaller values of relaxation times and activation energies. The conformation change is also accelerated when 20% PEO is added, which may be responsible for the faster methyl group rotation and faster ester side group rotation (β-relaxation).

8.2 Major contributions and conclusions

(1) A detailed comparison between UA and EA models of PEO is provided.

(2) A new analytical method is provided related to the isolation of different relaxation processes involved in polymers at high temperatures.

(3) High-temperature data for α-methyl rotation, ester methyl group rotation, the entire side group rotation, and the backbone motion of pure PMMA and PMMA in the blend are provided.

(4) Both relaxation times and activation energies for α-methyl rotation, ester methyl group rotation and the entire side group rotation at high temperatures are confirmed to be a continuity of experimental data from low temperatures.

(5) The possible origins of α- and β-relaxations in PMMA are investigated using molecular dynamics. The entire side group rotation and the backbone chain motion are suggested to be responsible for the α- and β-relaxations, respectively.

(6) The effects of blending on α-methyl rotation, ester-methyl group rotation, the entire side group rotation, and the backbone motion are investigated. It is found that both times and activation energies for α-methyl rotation, ester-methyl group rotation, the entire side group rotation, and the backbone motion of PMMA are reduced when adding PEO. It may be attributed to the speeded conformation changes of PMMA in blend.

8.3 Recommendation for future work

Our simulation models have been shown to provide a fair description of the self motions occurring in the PEO/PMMA blend as well as its pure components, while the collective motions are still beyond understanding. As shown in Fig. 8.1, the MD results are not consistent with neutron spin echo data. Does the molecular weight make this difference? This is the problem we need to figure out. It should be useful to conduct neutron spin echo experiments on a low molecular weight sample to check this difference.

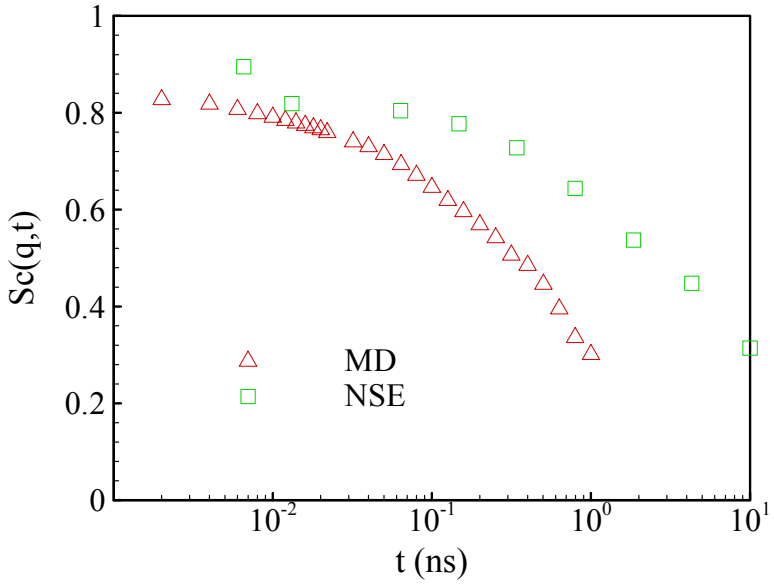

Fig. 8.1 Comparison of collective intermediate scattering function calculated from simulation to the neutron spin echo results at q = 0.89 Å^{-1} and 500 K for pure PMMA.

The current work studied the structure and dynamics of 20 wt% PEO/PMMA blend. To get a full picture of the effect of blend concentration on the methyl group rotation and the entire side group rotation, it is necessary to explore other blend concentrations.

The present blend simulation is performed on a molecular system that consists of around ten thousand particles, which takes about one month to equilibrate and another a few months to collect the data needed for analysis. It is necessary to parallelize the program to save computational time.

The data about the effect of tacticity on the rotation dynamics is lacking. It is useful to provide these data and give a clear picture of how dynamics are affected by tacticity. Based on the current work, this effect can be explored by studying the α-methyl

and ester methyl rotations and entire ester methyl group rotation in syndiotactic and isotactic PMMA.

Bibliography

[1] Adams, S. and Adolf, D. B. (1999). “Component dynamics of a miscible polymer blend: Polyisoprene and polyvinylethylene.” *Macromolecules* **32**(9): 3136-3145.

[2] Akkermans, R. L. C. and Briels, W. J. (2000). “Coarse-grained dynamics of one chain in a polymer melt.” *Journal of Chemical Physics* **113**(15): 6409-6422.

[3] Alegría, A., Colmenero, J., Ngai, K. L., and Roland, C. M. (1994). “Observation of the component dynamics in a miscible polymer blend by dielectric and mechanical spectroscopies.” *Macromolecules* **27**(16): 4486-4492.

[4] Allen, G. and Higgins, J. S. (1973). “Physicochemical aspects of neutron studies of molecular motion.” *Reports on Progress in Physics* **36**(9): 1073-133.

[5] Allen, G., Wright, C. J., and Higgins, J. S. (1974). “Effect of polymer microstructure on methyl group torsional vibrations.” *Polymer* **15**(5): 319-22.

[6] Alvarez, F., Arbe, A., and Colmenero, J. (2000). “Methyl group dynamics above the glass transition temperature: a molecular dynamics simulation in polyisoprene.” *Chemical Physics* **261**(1-2): 47-59.

[7] Ao, Z. M. and Jiang, Q. (2006). "Size effects on miscibility and glass transition temperature of binary polymer blend films." *Langmuir* **22**(3): 1241-1246.

[8] Apel, U. M., Hentschke, R., and Helfrich, J. (1995). “Molecular dynamics simulation of syndio- and isotactic poly(methyl methacrylate) in Benzene.” *Macromolecules* **28**(6): 1778-85.

[9] Arbe, A., Alegria, A., Colmenero, J., Hoffmann, S., Willner, L., and Richter, D. (1999). “Segmental dynamics in poly(vinylethylene)/polyisoprene miscible blends revisited. A neutron scattering and broad-band dielectric spectroscopy investigation.” *Macromolecules* **32**(22): 7572-7581.

[10] Arbe, A., Colmenero, J., Farago, B., Monkenbusch, M., Buchenau, U., and Richter, D. (2003). "Intermediate length scale dynamics in glass forming polymers: coherent and incoherent quasielastic neutron scattering results on polyisobutylene." *Chemical Physics* **292**(2-3): 295-309.

[11] Arbe, A., Monkenbusch, M., Stellbrink, J., Richter, D., Farago, B., Almdal, K., and Faust, R. (2001). “Origin of internal viscosity effects in flexible polymers: A comparative neutron spin-echo and light scattering study on poly(dimethylsiloxane) and polyisobutylene.” *Macromolecules* **34**(5): 1281-1290.

[12] Arbe, A., Richter, D., Colmenero, J., and Farago, B. (1996). "Merging of the α and β relaxations in polybutadiene: a neutron spin echo and dielectric study." *Physical Review E: Statistical Physics, Plasmas, Fluids, and Related Interdisciplinary Topics* **54**(4-B): 3853-3869.

[13] Arbe, A., Richter, D., Colmenero, J., and Farago, B. (1997). "Coherent quasielastic scattering from internal relaxations in polymers." *Physica B: Condensed Matter (Amsterdam)* **234-236**: 437-441.

[14] Arrighi, V. and Higgins, J. S. (1996). "Side group rotations in amorphous polymers." *Physica B: Condensed Matter (Amsterdam)* **226**(1-3): 1-9.

[15] Arrighi, V., Higgins, J. S., Burgess, A. N., and Howells, W. S. (1995a). "Rotation of methyl side groups in polymers: A Fourier transform approach to quasielastic neutron scattering. 1. Homopolymers." *Macromolecules* **28**(8): 2745-53.

[16] Arrighi, V., Higgins, J. S., Burgess, A. N., and Howells, W. S. (1995b). "Rotation of methyl side groups in polymers: A Fourier transform approach to quasielastic neutron scattering. 2. Polymer blends." *Macromolecules* **28**(13): 4622-30.

[17] Arrighi, V., Pappas, C., Triolo, A., and Pouget, S. (2001). "Temperature dependence of local chain dynamics in atactic polypropylene: A neutron spin-echo study." *Physica B: Condensed Matter (Amsterdam, Netherlands)* **301**(1&2): 157-162.

[18] Bée, M. (1988**)**. *Quasielastic neutron scattering*, Adam Hilger, Bristol.

[19] Berendsen, H. J. C., Postma, J. P. M., Vangunsteren, W. F., Dinola, A., and Haak, J. R. (1984). "Molecular-dynamics with coupling to an external bath.' *Journal of Chemical Physics* **81**(8): 3684-3690.

[20] Bergman, R., Alvarez, F., Alegria, A., and Colmenero, J. (1998). "The merging of the dielectric *α*- and *β*-relaxations in poly-(methyl methacrylate)." *Journal of Chemical Physics* **109**(17): 7546-7555.

[21] Bieze, T. W. N., Vandermaarel, J. R. C., Eisenbach, C. D., and Leyte, J. C. (1994). "Polymer dynamics in aqueous poly(ethylene oxide) solutions - an NMR-study." *Macromolecules* **27**(6): 1355-1366.

[22] Borodin, O. and Smith, G. D. (2003). "Development of quantum chemistry-based force fields for poly(ethylene oxide) with many-body polarization interactions." *Journal of Physical Chemistry B* **107**(28): 6801-6812.

[23] Borodin, O., Douglas, R. J., Smith, G. D., Trouw, F., and Petrucci, S. J. (2003a). "MD simulations and experimental study of structure, dynamics, and

thermodynamics of poly(ethylene oxide) and its oligomers." *Journal of Physical Chemistry B* **107**(28): 6813-6823.

[24] Borodin, O., Smith, G. D., and Douglas, R. J. (2003b). "Force field development and MD simulations of poly(ethylene oxide)/LiBF4 polymer electrolytes." *Journal of Physical Chemistry B* **107**(28): 6824-6837.

[25] Brown, D., Clarke, J. H. R., Okuda, M., and Yamazaki, T. (1994). "A molecular-dynamics study of chain configurations in n-Alkane-like liquids." *Journal of Chemical Physics* **100**(2): 1684-1692.

[26] Carlsson, P., Zorn, R., Andersson, D., Farago, B., Howells, W. S., and Borjesson, L. (2001). "The segmental dynamics of a polymer electrolyte investigated by coherent quasielastic neutron scattering." *Journal of Chemical Physics* **114**(21): 9645-9656.

[27] Cendoya, I., Alegria, A., Alberdi, J. M., Colmenero, J., Grimm, H., Richter, D., and Frick, B. (1999). "Effect of blending on the PVME dynamics. A dielectric, NMR, and QENS investigation." *Macromolecules* **32**(12): 4065-4078.

[28] Cereghetti, P. M., Kind, R., and Higgins, J. S. (2004). "Tacticity effects on the barriers to rotation of the ester methyl group in poly (methyl methacrylate): A deuteron magnetic resonance study." *Journal of chemical physics* **121**(16): 8068-78.

[29] Chen, C. X., Depa, P., García Sakai, V., Maranas, J. K., Lynn, J. W., Peral, I., and Copley, J. R. D. (2006a). "A comparison of united atom, explicit atom, and coarse-grained simulation models for poly(ethylene oxide)." *Journal of Chemical Physics* **124**(23): 234901/1-234901/11.

[30] Chen, C. X., Maranas, J. K., and Gacía Sakai, V. (2006b), "Local dynamics of syndiotactic poly(methyl methacrylate) using molecular dynamics simulation." *Macromolecules*, accepted.

[31] Chung, G. C., Kornfield, J. A., and Smith, S. D. (1994a). "Component dynamics in miscible polymer blends: A two-dimensional deuteron NMR investigation." *Macromolecules* **27**(4): 964-73.

[32] Chung, G. C., Kornfield, J. A., and Smith, S. D. (1994b). "Compositional dependence of segmental dynamics in a miscible polymer blend." *Macromolecules* **27**(20): 5729-41.

[33] Clark, J. and Maranas, J. K. (2003). "Densification effects on structural relaxation of polyolefins." *Journal of Chemical Physics* **119**(16): 8695-8703.

[34] Colby, R. H. (1989). "Breakdown of time temperature superposition in miscible polymer blends." *Polymer* **30**(7): 1275-1278.

[35] Copley, J. R. D. and Cook, J. C. (2003). "The Disk Chopper Spectrometer at NIST: a new instrument for quasielastic neutron scattering studies." *Chemical Physics* **292**(2-3): 477-485.

[36] De Gennes, P. G. (1979) *Scaling concepts in polymer physics*. Cornell University Press, Ithaca.

[37] de Leeuw, S. W., Van Zon, A., and Bel, G. J. (2001). "Structural relaxation in poly(ethylene oxide) and poly(ethylene oxide)-sodium iodide systems: A molecular dynamics study." *Electrochimica Acta* **46**(10-11): 1419-1426.

[38] Dionísio, M., Fernandes, A. C., Mano, J. F., Correia, N. T., and Sousa, R. C. (2000). "Relaxation studies in PEO/PMMA blends." *Macromolecules* **33**(3): 1002-1011.

[39] Doxastakis, M., Kitsiou, M., Fytas, G., Theodorou, D. N., Hadjichristidis, N., Meier, G., and Frick, B. (2000). "Component segmental mobilities in an athermal polymer blend: Quasielastic incoherent neutron scattering versus simulation." *Journal of Chemical Physics* **112**(19): 8687-8694.

[40] Ewald, P. P. (1921) "Die Berechnung optischer und elektrostatischer Gitterpotentiale", *Ann. Phys*., **64**, 253-287.

[41] Ewen, B. and Richter, D. (1997). "Neutron spin echo investigations on the segmental dynamics of polymers in melts, networks and solutions." *Advances in Polymer Science* **134**: 1-129.

[42] Farago, B. (1997). "IN11C, medium-resolution multidetector extension of the IN11 NSE spectrometer at the ILL." *Physica B* **241**: 113-116.

[43] Farago, B., Chen, C. X., Maranas, J. K., Kamath, S., Colby, R. H., Pasquale, A. J., and Long, T. E. (2005). "Collective motion in Poly(ethylene oxide) /poly(methylmethacrylate) blends." *Physical Review E* **72**(3).

[44] Flores, R., Perez, J., Cassagnau, P., Michel, A., and Cavaille, J. Y. (1996). "Dynamic mechanical behavior of poly(vinyl chloride)/poly(methyl methacrylate) polymer blend." *Journal of Applied Polymer Science* **60**(9): 1439-1453.

[45] Flory, P. J. (1953). *Principles of Polymer Chemistry*, Cornell University Press, Ithaca.

[46] Frenkel, D. and Smit, B. (2002). Understanding molecular simulation: From algorithms to applications, Academic Press, California.

[47] García Sakai, V., Chen, C. X., Maranas, J. K., and Chowdhuri, Z. (2004). "Effect of blending with poly(ethylene oxide) on the dynamics of poly(methyl methacrylate): A quasi-elastic neutron scattering approach." *Macromolecules* **37**(26): 9975-9983.

[48] García Sakai, V., Maranas, J. K., Chowdhuri, Z., Peral, I., and Copley, J. R. D. (2005). "Miscible blend dynamics and the length scale of local compositions." *Journal of Polymer Science Part B-Polymer Physics* **43**(20): 2914-2923.

[49] Genix, A. C., Arbe, A., Alvarez, F., Colmenero, J., Willner, L., and Richter, D. (2005). "Dynamics of poly(ethylene oxide) in a blend with poly(methyl methacrylate): A quasielastic neutron scattering and molecular dynamics simulations study." *Physical Review E* **72**(3).

[50] Gómez, D., Alegría, A., Arbe, A., and Colmenero, J. (2001). "Merging of the dielectric α and β relaxations in glass-forming polymers." *Macromolecules* **34**(3): 503-513.

[51] Heijboer, J., Baas, J. M. A., Van de Graaf, B., and Hoefnagel, M. A. (1987). "A molecular mechanics study on rotational motions of side groups in poly(methyl methacrylate)." *Polymer* **28**(3): 509-13.

[52] Higgins, J. S. (1982). *Static and dynamic properties of the polymeric solid state*, Eds. R. A. Pethrick and R. W. Richards, D. Reidel Publishing company, Dordrecht, p. 349.

[53] Higgins, J. S. and Benoît, H.C. (1996). *Polymers and Neutron Scattering*, Clarendon press, Oxford.

[54] Hoffmann, S., Willner, L., Richter, D., Arbe, A., Colmenero, J., and Farago, B. (2000). "Origin of dynamic heterogeneities in miscible polymer blends: A quasielastic neutron scattering study." *Physical Review Letters* **85**(4): 772-775.

[55] Humphreys, D. D., Friesner, R. A., and Berne, B. J. (1994). "A multiple-time-step molecular-dynamics algorithm for macromolecules." *Journal of Physical Chemistry* **98**(27): 6885-6892.

[56] Ito, H., Russell, T. P., and Wignall, G. D. (1987). "Interactions in mixtures of poly(ethylene oxide) and poly(methyl methacrylate)." *Macromolecules* **20**(9): 2213-2220.

[57] Johnson, J. A., Saboungi, M. L., Price, D. L., Ansell, S., Russell, T. P., Halley, J. W., and Nielsen, B. (1998). "Atomic structure of solid and liquid polyethylene oxide." *Journal of Chemical Physics* **109**(16): 7005-7010.

[58] Kahn, K. and Bruice, T. C. (2002). "Parameterization of OPLS-AA force field for the conformational analysis of macrocyclic polyketides." *Journal of Computational Chemistry* **23**(10): 977-996.

[59] Kamath, S., Colby, R. H., Kumar, S. K., Karatasos, K., Floudas, G., Fytas, G., and Roovers, J. E. L. (1999). "Segmental dynamics of miscible polymer blends: Comparison of the predictions of a concentration fluctuation model to experiment." *Journal of Chemical Physics* 111(13): 6121-6128.

[60] Kanaya, T. and Kaji, K. (2001). "Dynamics in the glassy state and near the glass transition of amorphous polymers as studied by neutron scattering." *Advances in Polymer Science* **154**: 87-141.

[61] Kant, R., Kumar, S. K., and Colby, R. H. (2003). "What length scales control the dynamics of miscible polymer blends?" *Macromolecules* **36**(26): 10087-10094.

[62] Karatasos, K., Ryckaert, J. P., Ricciardi, R., and Laupretre, F. (2002). "Methyl dynamics and β-relaxation in polyisobutylene: Comparison between experiment and molecular dynamics simulations." *Macromolecules* **35**(4): 1451-1462.

[63] Karatasos, K., Saija, F., and Ryckaert, J. P. (2001). "Short length-scale dynamics of polyisobutylene by molecular dynamics simulations." *Physica B: Condensed Matter (Amsterdam, Netherlands)* **301**(1&2): 119-125.

[64] Katana, G., Fischer, E. W., Hack, T., Abetz, V., and Kremer, F. (1995). "Influence of concentration fluctuations on the dielectric α-relaxation in homogeneous polymer mixtures." *Macromolecules* **28**(8): 2714-2722.

[65] Komeiji, Y., Uebayasi, M., Takata, R., Shimizu, A., Itsukashi, K., and Taiji, M. (1997). "Fast and accurate molecular dynamics simulation of a protein using a special-purpose computer." *Journal of Computational Chemistry* **18**(12): 1546-1563.

[66] Kremer, K. and Muller-Plathe, F. (2001). "Multiscale problems in polymer science: Simulation approaches." *Mrs Bulletin* **26**(3): 205-210.

[67] Kulik, A. S., Beckham, H. W., Schmidt-Rohr, K., Radloff, D., Pawelzik, U., Boeffel, C., and Spiess, H. W. (1994). "Coupling of α and β processes in poly(ethyl methacrylate) investigated by multidimensional NMR." *Macromolecules* **27**(17): 4746-54.

[68] Kumar, S. K., Colby, R. H., Anastasiadis, S. H., and Fytas, G. (1996). "Concentration fluctuation induced dynamic heterogeneities in polymer blends." *Journal of Chemical Physics* **105**(9): 3777-3788.

[69] Lartigue, C., Guillermo, A., and Cohen-Addad, J. P. (1997). "Proton NMR investigation of the local dynamics of PEO in PEO/PMMA blends." *Journal of Polymer Science, Part B: Polymer Physics* **35**(7): 1095-1105.

[70] Liu, J. H., Sakai, V. G., and Maranas, J. K. (2006). “Composition dependence of segmental dynamics of poly(methyl methacrylate) in miscible blends with poly(ethylene oxide).” *Macromolecules* **39**(8): 2866-2874.

[71] Londono, J. D., Annis, B. K., Habenschuss, A., Borodin, O., Smith, G. D., Turner, J. Z., and Soper, A. K. (1997). “Cation environment in molten lithium iodide doped poly(ethylene oxide).” *Macromolecules* **30**(23): 7151-7157.

[72] Lopez, C. F., Moore, P. B., Shelley, J. C., Shelley, M. Y., and Klein, M. L. (2002a). “Computer simulation studies of biomembranes using a coarse grain model.” *Computer Physics Communications* **147**(1-2): 1-6.

[73] Lopez, C. F., Nielsen, S. O., Moore, P. B., Shelley, J. C., and Klein, M. L. (2002b). “Self-assembly of a phospholipid Langmuir monolayer using coarse-grained molecular dynamics simulations.” *Journal of Physics-Condensed Matter* **14**(40): 9431-9444.

[74] Lovesey, S. W. (1984). *Theory of Neutron Scattering from Condensed Matter*. Vol. 1, Clarendon Press, Oxford.

[75] Lutz, T. R., He, Y., and Ediger, M. D. (2003). “Rapid poly(ethylene oxide) segmental dynamics in blends with poly(methyl methacrylate).” *Macromolecules* **36**(5): 1724.

[76] Madras, N. and Sokal, A. D. (1988). “The pivot algorithm - a highly efficient Monte-Carlo method for the self-avoiding walk.” *Journal of Statistical Physics* **50**(1-2): 109-186.

[77] Mao, G. M., Perea, R. F., Howells, W. S., Price, D. L., and Saboungi, M. L. (2000). “Relaxation in polymer electrolytes on the nanosecond timescale.” *Nature* **405**(6783): 163-165.

[78] Maranas, J. K., Mondello, M., Grest, G. S., Kumar, S. K., Debenedetti, P. G., and Graessley, W. W. (1998). “Liquid structure, thermodynamics, and mixing behavior of saturated hydrocarbon polymers. 1. Cohesive energy density and internal pressure.” *Macromolecules* **31**(20): 6991-6997.

[79] Mayo, S. L., Olafson, B. D., and Goddard, W. A. (1990). "DREIDING: A generic force-field for molecular simulations." *Journal of Physical Chemistry* **94**(26): 8897-8909.

[80] McCoy, J. D. and Curro, J. G. (1998). “Mapping of explicit atom onto united atom potentials.” *Macromolecules* **31**(26): 9362-9368.

[81] Merenga, A. S., Papadakis, C. M., Kremer, F., Liu, J., and Yee, A. F. (2001). "Broadband dielectric spectroscopy of the inter- and intramolecular dynamics of a series of random polyester copolymers." *Colloid and Polymer Science* **279**(11): 1064-1072.

[82] Meyer, A., Dimeo, R. M., Gehring, P. M., and Neumann, D. A. (2003). "The high-flux backscattering spectrometer at the NIST Center for Neutron Research." *Review of Scientific Instruments* **74**(5): 2759-2777.

[83] Min, B. C. (2001). "Component dynamics in polyisoprene/polyvinylethylene blends well above T-g." *Macromolecules* **34**(13): 4466-4475.

[84] Moreno, A. J., Alegria, A., Colmenero, J., and Frick, B. (2001a). "Methyl group dynamics in poly(methyl methacrylate): From quantum tunneling to classical hopping." *Macromolecules* **34**(14): 4886-4896.

[85] Moreno, A. J., Alegria, A., Colmenero, J., Prager, M., Grimm, H., and Frick, B. (2001b). "Methyl group dynamics in glassy toluene: A neutron scattering study." *Journal of Chemical Physics* **115**(19): 8958-8966.

[86] Mos, B., Verkerk, P., Pouget, S., van Zon, A., Bel, G. J., de Leeuw, S. W., and Eisenbach, C. D. (2000). "The dynamics in polyethyleneoxide-alkali iodide complexes investigated by neutron spin-echo spectroscopy and molecular dynamics simulations." *Journal of Chemical Physics* **113**(1): 4-7.

[87] Mudi, A. and Chakravarty, C. (2004). "Effect of the Berendsen thermostat on the dynamical properties of water." *Molecular Physics* **102**(7): 681-685.

[88] Mukhopadhyay, R., Alegria, A., Colmenero, J., and Frick, B. (1998). "Effect of blending on the methyl side group dynamics in poly(vinyl methyl ether)." *Journal of Non-Crystalline Solids* **235-237**: 233-236.

[89] Muralidharan, K., Deymier, P. A., and Simmons, J. H. (2003). "A concurrent multiscale finite difference time domain/molecular dynamics method for bridging an elastic continuum to an atomic system." *Modelling and Simulation in Materials Science and Engineering* **11**(4): 487-501.

[90] Neyertz, S. and Brown, D. (1995). "A computer-simulation study of the chain configurations in poly(ethylene oxide)-homolog melts." *Journal of Chemical Physics* **102**(24): 9725-9735.

[91] Neyertz, S., Brown, D., and Thomas, J. O. (1994). "Molecular-dynamics simulation of crystalline poly(ethylene oxide)." *Journal of Chemical Physics* **101**(11): 10064-10073.

[92] Padding, J. T. and Briels, W. J. (2001). “Uncrossability constraints in mesoscopic polymer melt simulations: Non-Rouse behavior of C120H242.’ *Journal of Chemical Physics* **115**(6): 2846-2859.

[93] Padding, J. T. and Briels, W. J. (2002). “Time and length scales of polymer melts studied by coarse-grained molecular dynamics simulations.’ *Journal of Chemical Physics* **117**(2): 925-943.

[94] Pathak, J. A., Colby, R. H., Floudas, G., and Jerome, R. (1999). “Dynamics in miscible blends of polystyrene and poly(vinyl methyl ether).” *Macromolecules* **32**(8): 2553-2561.

[95] Paul, W., Smith, G. D., and Yoon, D. Y. (1997). “Static and dynamic properties of a n-C100H202 melt from molecular dynamics simulations.” *Macromolecules* **30**(25): 7772-7780.

[96] Paul, W., Yoon, D. Y., and Smith, G. D. (1995). “An optimized united atom model for simulations of polymethylene melts.” *Journal of Chemical Physics* **103**(4): 1702-1709.

[97] Perez Aparicio, R., Arbe, A., Colmenero, J., Frick, B., Willner, L., Richter, D., and Fetters, L. J. (2006). “Quasielastic neutron scattering study on the effect of blending on the dynamics of head-to-head poly(propylene) and poly(ethylene-propylene).” *Macromolecules* **39**(3): 1060-1072.

[98] Pethrick, R. A. and Richards, R. W. (1982). *Static and Dynamic Properties of the Polymeric Solid State*, D. Reidel Publishing Company, Dordrecht.

[99] Phillips, J. C. (1996). "Stretched exponential relaxation in molecular and electronic glasses." *Reports on Progress in Physics* **59**(9): 1133-1207.

[100] Prager, M. and Heidemann, A. (1997). “Rotational tunneling and neutron spectroscopy: A compilation.” *Chemical Reviews* **97**(8): 2933-2966.

[101] Price, M. L. P., Ostrovsky, D., and Jorgensen, W. L. (2001). “Gas-phase and liquid-state properties of esters, nitriles, and nitro compounds with the OPLS-AA force field.” *Journal of Computational Chemistry* **22**(13): 1340-1352.

[102] Qiu, X. H., Moe, N. E., Ediger, M. D., and Fetters, L. J. (2000). “Local and global dynamics of atactic polypropylene melts by multiple field C-13 nuclear magnetic resonance.” *Journal of Chemical Physics* **113**(7): 2918-2926.

[103] Rafii-Tabar, H. and Chirazi, A. (2002). “Multi-scale computational modelling of solidification phenomena.” *Physics Reports-Review Section of Physics Letters* **365**(3): 145-249.

[104] Richter, D. (1997). "Neutron spin echo investigations in the α- and β- relaxation regime of polybutadiene." *Macromolecular Symposia* **121**: 147-161.

[105] Richter, D., Arbe, A., Colmenero, J., Monkenbusch, M., Farago, B., and Faust, R. (1998a). "Molecular motions in polyisobutylene: A neutron spin-echo and dielectric investigation." *Macromolecules* **31**(4): 1133-1143.

[106] Richter, D., Monkenbusch, M., Arbe, A., Colmenero, J., and Farago, B. (1998b). "Dynamic structure factors due to relaxation processes in glass-forming polymers." *Physica B: Condensed Matter (Amsterdam)* **241-243**: 1005-1012.

[107] Roe, R.-J. (2000). Methods of X-ray and neutron scattering in polymer science, Oxford university press, New York.

[108] Roland, C. M. and Ngai, K. L. (1991). "Dynamic heterogeneity in a miscible polymer blend." *Macromolecules* **24**(9): 2261-2265.

[109] Roovers, J. and Toporowski, P. M. (1992). "Rheological study of miscible blends of 1,4-polybutadiene and 1,2-polybutadiene (63% 1,2)." *Macromolecules* **25**(3): 1096-102.

[110] Russell, T. P., Ito, H., and Wignall, G. D. (1988). "Neutron and x-ray scattering studies on semicrystalline polymer blends." *Macromolecules* **21**(6): 1703-9.

[111] Saelee, C., Nicholson, T. M., and Davies, G. R. (2000). "A molecular dynamics study of methyl group rotation in poly(vinyl methyl ether)." *Macromolecules* **33**(6): 2258-2265.

[112] Schmidt-Rohr, K., Kulik, A. S., Beckham, H. W., Ohlemacher, A., Pawelzik, U., Boeffel, C., and Spiess, H. W. (1994). "Molecular nature of the β- relaxation in poly(methyl methacrylate) investigated by multidimensional NMR." *Macromolecules* **27**(17): 4733-4745.

[113] Smith, G. D. and Yoon, D. Y. (1994). "Equilibrium and dynamic properties of polymethylene melts from molecular-dynamics simulations .1. N-tridecane." *Journal of Chemical Physics* **100**(1): 649-658.

[114] Smith, G. D., Borodin, O., and Bedrov, D. J. (2002). "A revised quantum chemistry-based potential for poly(ethylene oxide) and its oligomers in aqueous solution." *Journal of Computational Chemistry* **23**(15): 1480-1488.

[115] Smith, G. D., Jaffe, R. L., and Yoon, D. Y. (1993). "A force-field for simulations of 1,2-dimethoxyethane and poly(oxyethylene) based upon ab-initio electronic-structure calculations on model molecules." *Journal of Physical Chemistry* **97**(49): 12752-12759.

[116] Smith, G. D., Paul, W., Yoon, D. Y., Zirkel, A., Hendricks, J., Richter, D., and Schober, H. (1997). "Local dynamics in a long-chain alkane melt from molecular dynamics simulations and neutron scattering experiments." *Journal of Chemical Physics* **107**(12): 4751-4755.

[117] Smith, G. D., Yoon, D. Y., Jaffe, R. L., Colby, R. H., Krishnamoorti, R., and Fetters, L. J. (1996). "Conformations and structures of poly(oxyethylene) melts from molecular dynamics simulations and small-angle neutron scattering experiments." *Macromolecules* **29**(10): 3462-3469.

[118] Soldera, A. (1998). "Comparison between the glass transition temperatures of the two PMMA tacticities. A molecular dynamics simulation point of view." *Macromolecular Symposia* **133**: 21-32.

[119] Soldera, A. and Metatla, N. (2005). "Glass transition phenomena observed in stereoregular PMMAs using molecular modeling." *Composites, Part A: Applied Science and Manufacturing* **36A**(4): 521-530.

[120] Tetsutani, T., Kakizaki, M., and Hideshima, T. (1982a). "Relaxation spectroscopy of the dielectric β-relaxation in poly(n-alkyl methacrylate)s by absorption-current measurements. I. Dielectric relaxation spectra for atactic polymers." *Polymer Journal (Tokyo, Japan)* **14**(4): 305-21.

[121] Tetsutani, T., Kakizaki, M., and Hideshima, T. (1982b). "Relaxation spectroscopy of the dielectric β-relaxation in poly(n-alkyl methacrylate)s by absorption-current measurements. II. Dielectric relaxation spectrum for isotactic poly(methyl methacrylate)." *Polymer Journal (Tokyo, Japan)* **14**(6): 471-6.

[122] Toukmaji, A. Y. and Board, J. A. (1996). "Ewald summation techniques in perspective: A survey." *Computer Physics Communications* **95**(2-3): 73-92.

[123] Trouw, F. R. and Price, D. L. (1999). "Chemical applications of neutron scattering." *Annual Review of Physical Chemistry* **50**: 571-601.

[124] Trouw, F. R., Borodin, O., Cook, J. C., Copley, J. R. D., and Smith, G. D. (2003). "Quasielastic neutron-scattering study of the local dynamics of poly(ethylene glycol) dimethyl ether in aqueous solution." *Journal of Physical Chemistry B* **107**(38): 10446-10452.

[125] Tsige, M., Curro, J. G., Grest, G. S., and McCoy, J. D. (2003). "Molecular dynamics simulations and integral equation theory of Alkane chains: Comparison of explicit and united atom models." *Macromolecules* **36**(6): 2158-2164.

[126] Tuckerman, M., Berne, B. J., and Martyna, G. J. (1992). "Reversible multiple time scale molecular-dynamics." *Journal of Chemical Physics* **97**(3): 1990-2001.

[127] Tyagi, M., Arbe, A., Colmenero, J., Frick, B., and Stewart, J. R. (2006). "Dynamic confinement effects in polymer blends. A quasielastic neutron scattering study of the dynamics of poly(ethylene oxide) in a blend with poly(vinyl acetate)." *Macromolecules* **39**(8): 3007-3018.

[128] van Zon, A., Mos, B., Verkerk, P., and de Leeuw, S. W. (2001). "On the dynamics of PEO-NaI polymer electrolytes." *Electrochimica Acta* **46**(10-11): 1717-1721.

[129] Whitehead, L., Edge, C. M., and Essex, J. W. (2001). "Molecular dynamics simulation of the hydrocarbon region of a biomembrane using a reduced representation model." *Journal of Computational Chemistry* **22**(14): 1622-1633.

[130] Wunderlich, W. (1989) In *Polymer Handbook*, 3rd ed.; Brandrup, J., Immergut, E. H., eds., John Wiley & Sons: New York, Sec. 5, p 77.

[131] Yoon, D. Y., Smith, G. D., and Matsuda, T. (1993). "A comparison of a united atom and an explicit atom model in simulations of polymethylene." *Journal of Chemical Physics* **98**(12): 10037-10043.

[132] Zawada, J. A., Ylitalo, C. M., Fuller, G. G., Colby, R. H., and Long, T. E. (1992). "Component relaxation dynamics in a miscible polymer blend - poly(ethylene oxide)/poly(methyl methacrylate)." *Macromolecules* **25**(11): 2896-2902.

[133] Zetsche, A. and Fischer, E. W. (1994). "Dielectric studies of the α-relaxation in miscible polymer blends and its relation to concentration fluctuations." *Acta Polymerica* **45**(3): 168-175.

[134] Zhu, W., Gisser, D. J., and Ediger, M. D. (1994). "C-13 NMR measurements of polybutadiene local dynamics in dilute-solution - further evidence for non-Kramers behavior." *Journal of Polymer Science Part B-Polymer Physics* **32**(13): 2251-2262.

[135] Zorn, R., Frick, B., and Fetters, L. J. (2002). "Quasielastic neutron scattering study of the methyl group dynamics in polyisoprene." *Journal of Chemical Physics* **116**(2): 845-853.

Vita

Chunxia Chen was born in Shandong, China. She received her B.S. degree in Chemistry from Qingdao University in 1996 and her M.S. degree in Material Science and Engineering from University of Science and Technology of China in 1999. She started her Ph.D. study in the Department of Chemical Engineering at the Pennsylvania State University from Spring 2001, focusing on the segmental dynamics in polymers.